



Universiteit  
Leiden  
The Netherlands

## **In vivo magnetic resonance imaging and spectroscopy of Alzheimer\_s disease in transgenic mice**

Braakman, N.

### **Citation**

Braakman, N. (2008, December 10). *In vivo magnetic resonance imaging and spectroscopy of Alzheimer\_s disease in transgenic mice*. Retrieved from <https://hdl.handle.net/1887/13328>

Version: Corrected Publisher's Version

License: [Licence agreement concerning inclusion of doctoral thesis in the Institutional Repository of the University of Leiden](#)

Downloaded from: <https://hdl.handle.net/1887/13328>

**Note:** To cite this publication please use the final published version (if applicable).

***In vivo* Magnetic Resonance Imaging and  
Spectroscopy of Alzheimer's Disease in  
Transgenic mice**

**Niels Braakman**

Niels Braakman

*In vivo* Magnetic Resonance Imaging and Spectroscopy of Alzheimer's Disease in Transgenic mice  
PhD Thesis, Leiden University, 10 December 2008

ISBN: 978-90-9023693-3

© Niels Braakman, except the following chapters:

Chapter 3 JMRI 2006, 24(3):530-536; 2006 © John Wiley & Sons, Inc. Reprinted with permission of Wiley-Liss, Inc. a subsidiary of John Wiley & Sons, Inc.

Chapter 4 MRM 2008, 60(2):449-456; 2008 © John Wiley & Sons, Inc. Reprinted with permission of Wiley-Liss, Inc. a subsidiary of John Wiley & Sons, Inc.

Cover photograph courtesy of Wim van Oordt

No part of this thesis may be reproduced in any form without the express written consent of the copyright holders.

*In vivo* Magnetic Resonance Imaging and Spectroscopy of  
Alzheimer's Disease in Transgenic mice

Proefschrift

ter verkrijging van  
de graad van Doctor aan de Universiteit Leiden,  
op gezag van Rector Magnificus prof.mr. P.F. van der Heijden,  
volgens besluit van het College voor Promoties  
te verdedigen op 10 december 2008  
klokke 10.00 uur

door

**Niels Braakman**

geboren te Curaçao, Nederlandse Antillen  
in 1976

**Promotiecommissie**

**Promotor:**

Prof. dr. H.J.M. de Groot

**Copromotor:**

Dr. A. Alia

**Referent:**

Prof. dr. K. Nicolay, Technische Universiteit Eindhoven

**Overige leden:**

Prof. dr. R. Schliebs, Paul Flechsig Institute for Brain Research, Leipzig, Germany

Prof. dr. J. Brouwer

The most exciting phrase to hear in science, the one that heralds new discoveries, is not 'Eureka!' but 'That's funny...'  
- *Isaac Asimov*

Voor Charlotte  
Voor mijn ouders



# Contents

<b>List of abbreviations</b>	<b>11</b>
<b>1 General introduction</b>	<b>15</b>
1.1 Alzheimer's disease	15
1.2 Alzheimer mouse models	17
1.3 Magnetic resonance techniques in studies of Alzheimer's disease	19
1.4 Thesis scope	27
References	29
<b>2 Theoretical background: MRI and MRS</b>	<b>37</b>
2.1 Magnetic Resonance Imaging	39
2.2 Magnetic Resonance Spectroscopy	43
2.3 Two-dimensional Magnetic Resonance Spectroscopy	46
References	50
<b>3 Longitudinal assessment of Alzheimer's <math>\beta</math>-amyloid plaque development in transgenic mice monitored by <i>in vivo</i> magnetic resonance microimaging</b>	<b>53</b>
3.1 Abstract	53
3.2 Introduction	53
3.3 Methods	55
3.4 Results	57
3.5 Discussion	62
Acknowledgements	65
References	66



<b>4</b>	<b>High resolution localized two dimensional magnetic resonance spectroscopy in mouse brain <i>in vivo</i></b>	<b>69</b>
4.1	Abstract	69
4.2	Introduction	69
4.3	Materials & Methods	70
4.4	Results and discussion	73
	Acknowledgements	80
	References	80
<b>5</b>	<b>Correlation between the severity of amyloid-<math>\beta</math> deposition and altered neurochemical profile in a transgenic mouse model of Alzheimer's disease, observed by <math>\mu</math>MRI and high resolution two-dimensional MRS</b>	<b>83</b>
5.1	Abstract	83
5.2	Introduction	83
5.3	Materials & methods	85
5.4	Results & Discussion	88
	Acknowledgements	95
	References	96
<b>6</b>	<b>General discussion and future outlook</b>	<b>101</b>
6.1	Visualization of AD hallmarks: amyloid plaques and beyond	101
6.2	2D MRS applications in AD	103
6.3	Potential challenges for the translation to humans	105
	References	106
	<b>Appendix: L-COSY pulse program</b>	<b>109</b>

---

<b>Summary</b>	<b>113</b>
<b>Samenvatting</b>	<b>115</b>
<b>Curriculum Vitae</b>	<b>119</b>
<b>List of publications</b>	<b>121</b>
<b>Nawoord</b>	<b>123</b>



# List of abbreviations

---

$\mu$ MRI	Magnetic Resonance micro-Imaging
1D	One-dimensional
2D	Two-dimensional
3D	Three-dimensional
ACQ	Acquisition
AD	Alzheimer's Disease
Ala	Alanine
APP	Amyloid Precursor Protein
ASL	Arterial Spin Labeling
Asp	Aspartate
A $\beta$	Amyloid $\beta$
CAA	Congophilic Amyloid Angiopathy
CFC	Contextual Fear Conditioning
Cho	Choline
COSY	Correlation Spectroscopy
cPLA <sub>2</sub>	Calcium-dependent Phospholipase A <sub>2</sub>
CNR	Contrast-to-Noise Ratio
Cr	Creatine
CRAZED	COSY revamped with asymmetric z-GE detection
CSF	Cerebrospinal Fluid
CT	Computed Tomography
DW	Diffusion Weighted
fMRI	Functional Magnetic Resonance Imaging
FOV	Field of View
FSB	( <i>E,E</i> )-1-fluoro-2,5-bis(3-hydroxycarbonyl-4-hydroxy)styryl-benzene
FSE	Fast Spin Echo
FWHH	Full Width at Half Height
GABA	$\gamma$ -Aminobutyric acid
GE	Gradient Echo

## Abbreviations

---

Glc	Glucose
Gln	Glutamine
Glu	Glutamate
Glx	Glutamine + Glutamate
GPC	Glycerophosphocholine
GPE	Glycerophosphoethanolamine
Gro	Glycerol
GSH	Glutathione
HCar	Homocarnosine
HPLC	High Performance Liquid Chromatography
IR-RARE	Inversion Recovery RARE
Lac	Lactate
L-COSY	Localized Correlation Spectroscopy
MAPT	Microtubule Associated Protein Tau
MCI	Mild Cognitive Impairment
mI	<i>myo</i> -Inositol
MION	Monocrystalline Iron Oxide Nanoparticles
MM	Macromolecule
MMSE	Mini Mental State Examination
MRA	Magnetic Resonance Angiography
MRI	Magnetic Resonance Imaging
MRM	Magnetic Resonance Microscopy
MRS	Magnetic Resonance Spectroscopy
MSME	Multi-Slice Multi-Echo
MTX	Matrix
NA	Number of Averages
NAA	N-Acetylaspartate
NAAG	N-acetylaspartylglutamate
NEX	Number of Excitations
NFT	Neurofibrillary Tangle
NMDA	N-methyl-D-aspartate
NMR	Nuclear Magnetic Resonance
OR	Object Recognition
OVS	Outer Volume Suppression
PCh	Phosphocholine
PCr	Phospho-creatine

---

PEA	Phosphoethanolamine
PET	Positron Emission Tomography
PIB	Pittsburgh-B compound
PLA <sub>2</sub>	Phospholipase A <sub>2</sub>
PPI	Pre-Pulse Inhibition
PRESS	Point Resolved Spectroscopy
PS1, PS2	Presenilin 1, Presenilin 2
PUT	Putrescine
PtdCho	Phosphatidyl Choline
QSINE	Squared Sine function
RARE	Rapid Acquisition with Relaxation Enhancement
ROI	Region Of Interest
SE	Spin Echo
sI	<i>scyllo</i> -Inositol
SNR	Signal-to-Noise Ratio
SPECT	Single Photon Emission CT
T	Tesla
$T_1$	Longitudinal or spin-lattice relaxation time
$T_2$	Transverse or spin-spin relaxation time
Tau	Taurine
tCr	Total Creatine (Creatine + Phosphocreatine)
TE	Echo Time
Tg	Transgenic
Thr	Threonine
TR	Repetition Time
Tyr	Tyrosine
VAPOR	Variable Pulse power and Optimized Relaxation delays
VOI	Volume Of Interest
WT	Wild-type



# 1 General introduction\*

## 1.1 Alzheimer's disease

Alzheimer's disease is the most common neurodegenerative disease, the exact cause of which is still unknown. AD increases in incidence exponentially with age and is therefore poised to become a leading health problem as the population ages. The disease is characterized by a disruption of the neuronal function, progressive memory loss and gradual cognitive, functional and behavioral deterioration (1,2).

The two most prominent pathological features of AD are the extracellular senile plaques, and intracellular neurofibrillary tangles (Fig. 1.1) (1). Senile plaques consist of aggregated amyloid  $\beta$  protein, and are located mainly in the hippocampus, cerebral cortex and other areas of the brain essential for cognitive function. Neurofibrillary tangles consist of the hyperphosphorylated form of the microtubule associated protein tau. As the tau starts to form neurofibrillary tangles, it loses its cytoskeleton stabilizing function, leading to a collapse of the supporting structures in the neurons (Fig. 1.1). Other pathological features of the disease include neuronal cell loss, microglial activation, gross cerebral atrophy and synapse loss. Synaptic alterations and loss are considered by some investigators to be the most likely cause of the observed clinical symptoms (2).

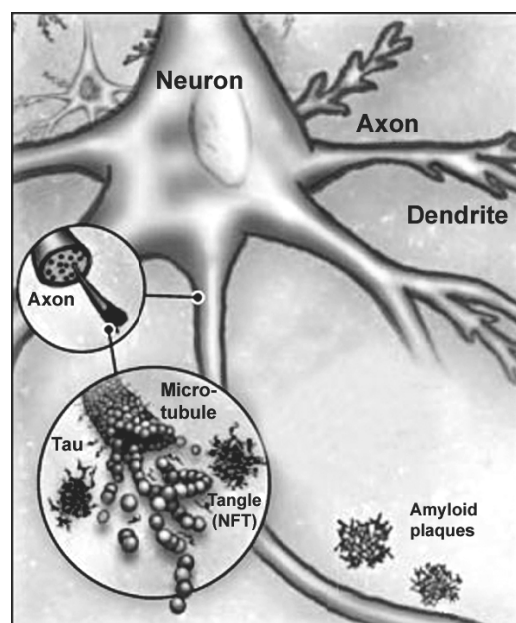


Fig. 1.1. Pathology of AD. Senile plaques that consist of  $A\beta$  are located extracellularly, while neurofibrillary tangles consisting of hyperphosphorylated tau are located intracellularly in AD brain.

The core of senile plaques consists mainly of aggregated amyloidogenic peptide  $A\beta$ , a highly hydrophobic peptide that spontaneously aggregates *in vitro* (3). The amyloid  $\beta$  protein is a 39- to 43-amino acid protein derived from the amyloid protein precursor through proteolytic cleavage by  $\beta$ - and  $\gamma$ -secretases (4,5). Soluble  $A\beta$  is a product of normal cell metabolism, and found in various body fluids including blood and

\*Parts of this chapter were submitted to Curr Alzheimer Res



cerebrospinal fluid. Recent studies have shown that in AD brain, A $\beta$  protein with 42 amino acid residues (A $\beta$ <sub>1-42</sub>) is deposited first and is the predominant form in senile plaques, while A $\beta$  protein with 40 amino acid residues (A $\beta$ <sub>1-40</sub>) is deposited later in the disease and is prominent in vascular amyloid deposits (6). During aggregation, single monomeric A $\beta$  peptides bind together to form oligomeric strings that assemble into fibrillar sheets. Multiple fibrils bind to form the backbone of the amyloid plaque, trapping other macromolecules along the way. There is recent consensus that the disordered metabolism of A $\beta$  is central to the pathological cascade that ultimately leads to clinical AD, although the presence of A $\beta$  plaques does not correlate well with neuronal loss and the onset, progress, or severity of dementia (7,8). The wide variety of mouse models of AD currently available (see section 1.2) has helped validate the assumed close relationship between A $\beta$  accumulation and the formation of neurofibrillary pathology and neurodegeneration (4). Fig. 1.2 shows a recently proposed scheme of the interaction between A $\beta$  and microtubule associated protein tau in AD pathogenesis (4).

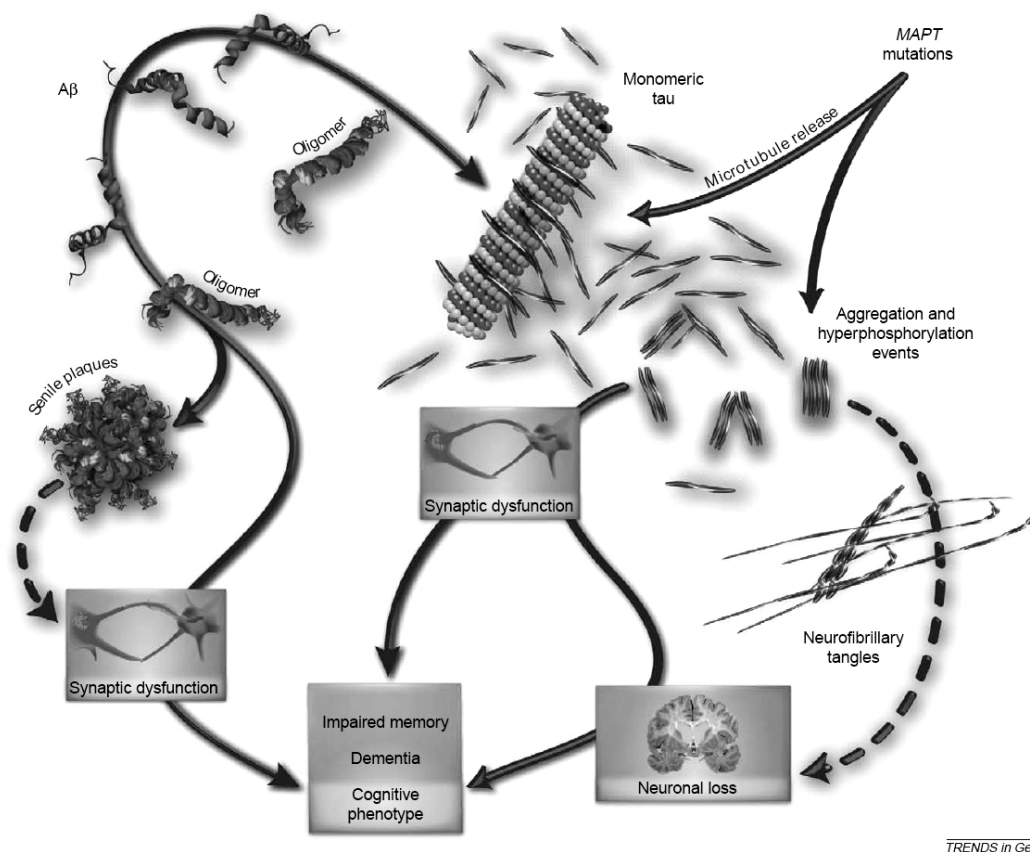


Fig. 1.2. The interaction of A $\beta$  and microtubule associated protein tau (MAPT) in AD pathogenesis. In this scheme, accumulation of aggregated A $\beta$  oligomers accelerates the parallel process of the formation of MAPT pathology. The toxic MAPT species then initiates neurodegeneration. Reprinted, with permission, from McGowan et al. 2006 (4). © Elsevier Ltd.

In this scheme, A $\beta$  monomers can form soluble oligomeric species that cause synaptic dysfunction but do not lead directly to neuronal cell death (9). A $\beta$  oligomers also aggregate to form senile plaques, and these dense cored structures have been shown to cause synaptic degeneration directly (10,11). In addition to a direct impact on synaptic activity, soluble A $\beta$  oligomers can target MAPT pathogenesis, causing an acceleration of MAPT aggregation to form NFT with associated hyperphosphorylation (12). However, the major MAPT toxic species is not NFT. Earlier stage aggregates or modified monomers that appear to initially cause the reversible neuronal, or perhaps synaptic, dysfunction. Increasing accumulation leads to neuronal loss and permanent effects on cognitive phenotype (13).

The amyloid in senile plaques forms spherical cores that can range from 2 to ~200  $\mu\text{m}$ , and are typically 20-60  $\mu\text{m}$  in diameter (14). A $\beta$  plaque formation precedes disease onset by many years and is generally accepted as a biomarker for onset and progression of the AD (7,15). Consequently, amyloid reduction in humans is now a major therapeutic objective. The map of plaque deposition established from post-mortem tissue samples indicates that amyloid is initially deposited in the basal temporal neocortex or entorhinal cortex. Deposition is then extended through the hippocampal formation and, in the final stage, to virtually all cortical areas, including the highly myelinated areas of the neocortex (16,17). However, establishment of the true map of plaque deposition as the disease progresses in living subjects is difficult due to lack of *in vivo* imaging methods for visualizing the development of A $\beta$  plaques in humans.

Currently there is no definitive diagnosis for AD, except by post-mortem observation of senile plaques and neurofibrillary tangles and by eliminating other neurodegenerative disorders. The ability to visualize plaques or neurofibrillary tangles with an *in vivo* imaging technique coupled with clinical diagnosis would add a large degree of confidence to the diagnosis of AD. Non-invasive rapid visualization of A $\beta$  plaques and identification of new early biomarkers of AD would not only facilitate intervention and enhance treatment success but also contribute toward understanding the mechanism of Alzheimer's disease.

## **1.2 Alzheimer mouse models**

The main link between AD and A $\beta$  is based on genetic mutations which were discovered in familial forms of AD and result in increased levels and deposition of A $\beta$ . The three known classes of mutations associated with early onset, or familial AD all directly affect

amyloid metabolism and are: (a) mutations associated with the APP gene; (b) mutations associated with presenilin 1; and (c) mutations associated with presenilin 2. Presenilins are part of the  $\gamma$ -secretase protein complex, an internal protease that cleaves within the membrane-spanning domain of its substrate proteins, including APP (4). Transgenic mouse models of AD have been created by inserting one or more of these human mutations into the mouse genome (4,18,19). These transgenic mice display extensive amyloid plaque formation, while plaques are not found in the corresponding wild-type mice (15,20). Different strains of transgenic AD mice develop plaques at different rates (15,20). However, despite the amyloid deposition observed in these models, none of them develops widespread neuronal loss (21,22). Recently transgenic mice with MAPT mutations have also been developed. These mice develop neurofibrillary tangles similar to humans, coupled with neuronal losses in the affected brain regions (13,23,24). Several groups have combined APP, PS1, PS2 and/or MAPT mutations to generate double or triple transgenic mice. In these mice it was observed that A $\beta$  deposition precedes neurofibrillary tangle development by several months, and furthermore that neurofibrillary tangle pathology was enhanced compared to MAPT-only transgenic mice (12,25,26). These findings suggest that A $\beta$  accumulation can accelerate, if not initiate, the formation of neurofibrillary tangle pathology (12,27,28). A brief overview of the most commonly used transgenic mouse models of AD is given in Table 1.1.

Among the various commonly used mouse models, Tg2576 (19) is one of the most widely used models. This model over-expresses a human APP cDNA transgene with the K670M/N671L double mutation (APP<sub>swe</sub> or Swedish mutation from the location of the family where the gene was originally identified). Tg2576 mice develop plaques starting at ~9 months of age and show memory deficits. The plaque distribution is primarily in the cortex and hippocampus, and, at later ages, is quite pronounced in the cingulate cortex. Tg2576 mice were used in the studies presented in chapters 3 and 5 of this thesis.

Table 1.1: Overview of the most commonly used mouse models in AD research

Model name	Transgene ( <i>mutation</i> )	Cognitive deficits	Age of onset: Pathology	reference
<b>Tg2576</b>	APP ( <i>APP<sub>695</sub></i> )	Impaired reference and working memory, OR, CFC	9-11 months: A $\beta$ plaques, astrogliosis, microgliosis, increased oxidative stress, dystrophic neurites	(19)
<b>APP23</b>	APP ( <i>APP<sub>751</sub></i> )	Impaired: reference memory, passive avoidance. Abnormal reflexes and stereotypic behavior, seizures	6 months: A $\beta$ plaques, neuronal loss in CA1 region of hippocampus	(29)
<b>PS1<sub>M146V</sub>, PS1<sub>M146L</sub></b>	PS1 ( <i>PS1<sub>M146V</sub>, PS1<sub>M146L</sub></i> )	No behavioral abnormalities	No abnormal pathology; elevated A $\beta$ 42, altered mitochondrial activity, dysregulation of calcium homeostasis in PS1 <sub>M146V</sub>	(30)
<b>PSAPP</b>	APP/PS1 ( <i>PS1<sub>M146L</sub>, APP<sub>695</sub>, PS1-A246E, APP<sub>695</sub></i> )	Impaired reference and working memory	6-9 months: (accelerated) A $\beta$ deposition, gliosis, dystrophic neurites	(18,31)
<b>JNPL3</b>	Tau ( <i>Tau<sub>P301L</sub></i> )	Not reported; Mice show progressing motor impairment with age	NFTs in spinal cord, spinal cord atrophy, astrogliosis in spinal cord, brain stem, diencephalon and telencephalon	(24)
<b>Tau<sub>P301S</sub></b>	Tau ( <i>Tau<sub>P301S</sub></i> )	Not reported	NFTs, severe paralysis of lower limbs due to motor neuron loss	(23)
<b>Tau<sub>V337M</sub></b>	Tau ( <i>Tau<sub>V337M</sub></i> )	Increased locomotor activity, deficits in plus maze	NFTs and neuronal degradation in hippocampus	(32)
<b>Tau<sub>R406W</sub></b>	Tau ( <i>Tau<sub>R406W</sub></i> )	Impaired associative memory in CFC, abnormality in PPI	Accumulation of insoluble tau, hyperphosphorylated tau inclusions in forebrain	(33)
<b>rTg4510</b>	Tau ( <i>Tau<sub>P301L</sub></i> )	Spatial defects, cognitive effects early. At 9.5 months exhibit decreased ambulation, body weight, hunched posture	Progressive age-related NFTs, neuronal loss and forebrain atrophy	(13,34)
<b>Htau</b>	Tau ( <i>Human Tau</i> )	Not reported	NFTs and neuronal death	(35)
<b>TAPP</b>	APP/Tau ( <i>APP<sub>695</sub>, Tau<sub>P301L</sub></i> )	Not reported	A $\beta$ plaques, NFTs, gliosis	(12)
<b>3<math>\times</math>TgAD</b>	APP/Tau/PS1 ( <i>APP<sub>695</sub>, Tau<sub>P301L</sub>, PS1<sub>M146V</sub></i> )	Age-progressing memory impairment that	Age-dependent A $\beta$ plaques, followed by the development of NFTs. Age-dependent synaptic dysfunction	(25,27)

Cognitive deficits: OR, object recognition; CFC, contextual fear conditioning; PPI, pre-pulse inhibition. Neuropathology: NFT, neurofibrillary tangle; CAA, congophilic amyloid angiopathy.

### 1.3 Magnetic resonance techniques in studies of Alzheimer's disease

Due to the importance of visualizing AD pathology *in vivo* to track disease progression and evaluate possible therapeutic interventions, much effort has focused in recent years on developing an imaging technique capable of accomplishing this. A major breakthrough in the imaging of AD has been the development of amyloid imaging tracers, such as the ‘‘Pittsburgh-B’’ compound, for positron emission tomography (36).

Although these markers allow visualization of plaque burden with PET in living AD patients (37), individual plaques with sizes ranging from 2-200  $\mu\text{m}$  (14), are beyond the resolution of PET. Magnetic resonance imaging is an alternative imaging technique that should theoretically be able to reach the resolution necessary to visualize individual plaques, especially at high fields. An additional benefit of MRI is that it is a safer technique than PET as it does not require the use of ionizing radiation.

Presently various MR techniques that measure the anatomic, biochemical, microstructural, functional, and blood flow changes are being evaluated as possible surrogate measures of AD progression. MR based volumetry is being explored to detect anatomical changes and differentiate patients with AD from cognitive normal elderly (38), however, the validity of these MR-based volumetry for AD diagnosis remains to be established. Furthermore, volumetric imaging in transgenic mouse models of Alzheimer's disease is challenging due to the small size of the structures of interest in the brain and the low contrast between these structures. Although manual segmentation is still considered as the gold standard in morphometric studies, the variability in these findings is large (39). Consequently, relatively few studies on volumetric imaging in mice have been reported thus far. Efforts to image plaques using MRI are also underway. Over the last few years, multiple research groups have attempted to image A $\beta$  plaque-load using MR microimaging (Table 1.2). For  $\mu\text{MRI}$ , strong magnetic field gradients and specialized radio frequency coils are used to generate images with higher spatial resolution than with normal MRI. Several studies involving  $\mu\text{MRI}$  of A $\beta$  plaques *ex vivo* in human and *ex vivo* and *in vivo* in different transgenic mouse models of AD have been carried out with or without targeted contrast agents (Table 1.2). However, imaging of A $\beta$  plaques *in vivo* still lacks sufficient sensitivity and requires further improvement. Another strategy to detect the presence of A $\beta$  plaques in AD brain is to look for changes in MR relaxation rates which might be associated with the presence of A $\beta$ . For instance, the transverse relaxation time of brain tissue might be modified due to the presence of iron in A $\beta$  deposits (40). Functional MRI methods are being tested in an attempt to differentiate between AD patients and cognitively normal people. These methods measure differences in brain activation, such as visual saccades, visual and motor responses, semantic processing, angle discrimination, and memory (38). MR angiography is being investigated as a method to detect blood flow voids in transgenic mouse models of AD (41). Arterial spin labeling might aid in identifying blood flow reductions in AD patients relative to controls (42). MR spectroscopy is another MR-based technique that allows detection of biochemical changes in the brain and provides a noninvasive way to investigate *in vivo*

neurochemical abnormalities. MRS is being explored for detection of the altered neurochemical profile in AD brain (43). However, neurochemical changes that are specific only to AD have not yet been identified by MRS. A brief account of the development and future demands of MR imaging methods for A $\beta$  plaque visualization, MR relaxometry and MRS for assessment of AD pathology is given below.

### 1.3.1 MRI to visualize A $\beta$ plaques

Nearly a century after the first observation of plaques in post-mortem brain tissue by Alois Alzheimer in 1906, investigators are beginning to visualize A $\beta$  plaques using MRI. MRI can provide much better resolution than SPECT or PET and can theoretically resolve individual plaques non-invasively. The first successful attempt to visualize plaques in fixed human tissue was achieved by Benveniste *et al.* in 1999 (44) using  $T_2^*$ -weighted MRI at 7T with a spatial resolution in the range of  $40 \times 40 \times 40 \mu\text{m}^3$  ( $\sim 6 \times 10^{-5} \text{mm}^3$ ). Plaques emerged as black, spherical elements on  $T_2^*$  images, which can be attributed to the known presence of metals, particularly iron, in A $\beta$  plaques (44). This finding was not replicated in another study, which reported the observed hypointensities to be vascular structures rather than A $\beta$  plaques (45). Subsequently several types of transgenic mouse models of AD have also been used to visualize plaques in fixed mouse brain at different field strengths (4.7T, 7T, 9.4T). The scan times in these studies varied from  $\sim 60$  min up to 15h. The best resolution achieved was  $46 \times 72 \times 72 \mu\text{m}^3$  using a spin echo sequence at 9.4T in 14h (46). Utilizing a fast spin echo sequence, plaque visualization was possible in 10-11 hours with a resolution of  $54 \times 58 \times 200 \mu\text{m}^3$  (47). Gradient echo sequences have been utilized for the *ex vivo* imaging of plaques in mouse brain that were stained with unspecific or target specific gadolinium based contrast agents (48,49).

Visualization of either plaque-load, or preferably individual plaques, in living human AD patients is an important goal of MRI studies in AD. However, current *in vivo*  $\mu$ MRI of A $\beta$  plaques has only been successfully implemented in mouse models of AD, as the required field strengths are not yet widely available for human use. For the imaging of A $\beta$  in mice, two distinct methods have been implemented: (i) methods using plaque specific gadolinium-, MION-, or  $^{19}\text{F}$ -based contrast agents (50,51), and (ii) methods relying on the endogenous chemical properties of plaques to generate the desired contrast on MR images (8,52-54). The first reported study of *in vivo* plaque visualization in transgenic mice was by Wadghiri *et al.* in 2003 (51). This study was performed at 7T, using  $T_2$  weighted SE and  $T_2^*$  weighted GE sequences to obtain spatial resolutions of  $59 \times 59 \times 500$

$\mu\text{m}$  and  $59 \times 59 \times 250 \mu\text{m}^3$ , in scan times of 1-2 hrs. However, in this study the mice were administered different contrast agents prior to imaging, requiring a relatively invasive procedure. As a result longitudinal studies are generally not possible using this technique. In subsequent studies, A $\beta$  plaques have been visualized in live mouse brain, without the need for an exogenous contrast agent (52,53). These studies were done at 9.4T with a spatial resolution of  $60 \times 60 \times 120 \mu\text{m}^3$  using a  $T_2$  weighted SE sequence. However, imaging time was more than 1h and cardio-respiratory triggering was necessary to prevent motion artifacts (52,53). An overview of the described *in vivo* A $\beta$  imaging studies is given in table 1.2. Despite these developments, plaque visualization still requires long measurement times, which makes it difficult to perform studies in human patients, or with a large number of animals. In addition, longitudinal MR studies to follow the development of plaques with age in the same animals have not been attempted in the above studies.

Table 1.2: MR imaging of A $\beta$  plaques in humans and mouse models of Alzheimer disease.

Reference	Species	<i>in vivo</i> / <i>ex vivo</i>	Contrast agent	MRI method	Field Strength	Image resolution	Imaging time
Benveniste <i>et al.</i> 1999 (44)	Human	<i>ex vivo</i>	-	3D $T_2^*$ GE; 3D DW SE	7T	$5.9 \times 10^{-5} \text{ mm}^3$	2.7-21.8 hr (GE) 4.6-18.2 hr (SE)
Dhenain <i>et al.</i> 2002 (45)	Human	<i>ex vivo</i>	-	$T_2^*$ GE	11.7T	$46.9 \times 23.4 \times 23.4 \mu\text{m}^3$ $23.4 \times 23.4 \times 23.4 \mu\text{m}^3$	16-18 hr
Poduslo <i>et al.</i> 2002 (49)	Mice: APP/PS1	<i>ex vivo</i>	PUT-Gd- A $\beta$	Not specified	7T	$62.5 \times 62.5 \times 62.5 \mu\text{m}^3$	$\sim 14$ hr ( $T_1$ W) $\sim 15$ hr ( $T_2$ W)
Wadghiri <i>et al.</i> 2003 (51)	Mice: APP, APP/PS1	<i>in vivo</i> ; <i>ex vivo</i>	A $\beta$ -Gd; A $\beta$ -MION	2D/3D $T_1$ SE; 2D $T_2$ SE; 2D $T_2^*$ GE	7T	$59 \times 59 \times 500 \mu\text{m}^3$ $59 \times 59 \times 250 \mu\text{m}^3$	120 min ( $T_2$ SE) 59 min ( $T_2^*$ GE)
Zhang <i>et al.</i> 2004 (46)	Mice: APP, APP/PS1	<i>ex vivo</i>	-	$T_2$ SE	9.4T	$46 \times 72 \times 72 \mu\text{m}^3$	14 hr
Lee <i>et al.</i> 2004 (47)	Mice: PS1, APP/PS1	<i>ex vivo</i>	-	$T_2$ FSE	7T	$54 \times 58 \times 200 \mu\text{m}^3$	65-80 min
Jack <i>et al.</i> 2004 (52)	Mice: APP/PS1	<i>in vivo</i> ; <i>ex vivo</i>	-	$T_2$ SE; $T_2^*$ GE	9.4T	$60 \times 60 \times 120 \mu\text{m}^3$	67 min (SE) 87 min (GE)
Jack <i>et al.</i> 2005 (53)	Mice: APP/PS1	<i>in vivo</i> ; <i>ex vivo</i>	-	$T_2$ SE	9.4T	$60 \times 60 \times 120 \mu\text{m}^3$ ( $30 \times 30 \times 60 \mu\text{m}^3$ )	100 min
Vanhoutte <i>et al.</i> 2005 (54)	Mice: APP <sub>V717I</sub>	<i>in vivo</i>	-	3D $T_2^*$ GE	7T	$78 \times 156 \times 234 \mu\text{m}^3$ ( $78 \times 78 \times 58 \mu\text{m}^3$ )	68 min
Higuchi <i>et al.</i> 2005 (50)	Mice: Tg2576	<i>in vivo</i>	$^{19}\text{F}$ -FSB	2D FSE; 3D FSE; $T_1$ GE	9.4T	$156 \times 156 \times 500 \mu\text{m}^3$	42 min
Dhenain <i>et al.</i> 2006 (48)	Mice: APP/PS1	<i>ex vivo</i>	-	3D $T_2^*$ GE	4.7T	$63 \times 47 \times 59 \mu\text{m}^3$	7-9 hr

2D/3D, 2- or 3-dimensional;  $T_1/T_2/T_2^*$ , applied weighting in MR imaging experiments; DW, diffusion-weighted;  $^{19}\text{F}$ , imaging of Fluorine-19 labeled contrast agent; GE, Gradient Echo; SE, Spin Echo; FSE, Fast Spin Echo.

### 1.3.2 MR relaxometry for the assessment of AD pathology

In addition to anatomical or pathological features, several intrinsic MR parameters can be studied to determine the effect of disease progression. In relaxometric approaches, the  $T_1$  (longitudinal, or spin-lattice) and  $T_2$  (transverse, or spin-spin) relaxation rates can be studied to facilitate the quantification of disease processes.  $T_1$  specifies the rate at which the net magnetization returns to its equilibrium state along the axis of the magnet bore, while  $T_2$  specifies the rate at which the net magnetization in the transverse plane returns to zero after RF excitation. Alternate relaxation parameters are  $T_2^*$  and  $T_{1\rho}$ ; Unlike  $T_2$ ,  $T_2^*$  is influenced by magnetic field gradient inhomogeneities and is always shorter than the  $T_2$  relaxation time. The spin lattice relaxation time constant in the rotating frame,  $T_{1\rho}$ , determines the decay of the transverse magnetization in the presence of a “spin-lock” RF field (55).

Since both the  $T_2$  and  $T_1$  relaxation times are sensitive to changes in the biophysical water environment it has been hypothesized that the presence of increased deposition of A $\beta$  in the brain affects these parameters (40). As such they might be used as independent markers for changes occurring in tissue, averaged over an ROI. Based on the findings reported thus far,  $T_2$  relaxation appears to be more sensitive to pathophysiology than  $T_1$  relaxation. Several groups have studied the effects of AD progression on the transverse relaxation rate  $T_2$ . There is converging evidence that the  $T_2$  values of affected brain tissue are lower than in controls, and decrease as AD progresses (40,56,57). It has been proposed that a decrease of  $T_2$  values provides evidence of early involvement of regional pathophysiological changes in the absence of neuronal cell loss in mouse brains exhibiting amyloid plaque neuropathology. The explicit influence of plaques on  $T_2$  reduction is not yet clear. It has been proposed that the presence of iron in the plaques and/or cell shrinkage may be associated with decreased  $T_2$  relaxation in plaque affected areas. Very recently, El Tannir El Tayara *et al.* have shown that  $T_2$  relaxation can be affected by plaque deposition, without histochemically detectable iron (57). Furthermore, it has been proposed that a reduced cerebral blood flow resulting from amyloid deposition on vessel walls could contribute to the reduction in  $T_2$  (40,56). A decrease of both  $T_2^*$  and  $T_{1\rho}$  values in plaque affected areas has been reported as well (54,55). An overview of recent relaxometry research in AD mouse models is presented in table 1.3. In most of these studies relaxation time and progressive A $\beta$  deposition has been studied either at one time point or at various time points in different mice belonging to different age groups. A proper longitudinal MR study which follows both the development of A $\beta$  plaques and changes in  $T_2$  relaxation times with age in the same animals is lacking.



Table 1.3: Relaxometry measurements in AD mouse models

Reference	Relaxometric Parameter	AD mouse model	Remarks
Helpert <i>et al.</i> 2004 (40)	$T_1, T_2$	APP/PS1; PS1	$T_2$ lower in APP/PS1 and PS1 mice than in controls. No significant changes in $T_1$ detected.
Falangola <i>et al.</i> 2005 (58)	$T_2$	APP/PS1; PS1	$T_2$ decreased in APP/PS1 mice compared to controls
Vanhoutte <i>et al.</i> 2005 (54)	$T_2^*$	APP <sub>V717I</sub>	$T_2^*$ decreased in APP <sub>V717I</sub> mice compared to controls
Borthakur <i>et al.</i> 2006 (55)	$T_{1\rho}$	APP/PS1	$T_{1\rho}$ decreased after 12 months of age in APP/PS1 mice
El Tannir El Tayara <i>et al.</i> 2007 (57)	$T_2$	APP/PS1; PS1	$T_2$ decreased in amyloid loaded areas in APP/PS1 mice.
Falangola <i>et al.</i> 2007 (56)	$T_2$	APP/PS1; APP; PS1	Significant decrease in $T_2$ in APP and APP/PS1 mice. A longitudinal study*.

\*several mice at each time point were measured longitudinally for  $T_2$  measurements. However, as the experiment progressed, several of the mice that the experiment was started with were no longer included. To maintain a fixed number of animals, those that died between measurements were replaced with fresh ones.

### 1.3.3 MR spectroscopy of Alzheimer's disease

MRS is a noninvasive tool that can be used to measure the chemical composition of tissues *in vivo* and characterize functional metabolic processes in different parts of the body. In brain, MRS can provide a wealth of information on various facets of *in vivo* neurochemistry, including neuronal health, gliosis, osmoregulation, energy metabolism, neuronal-gial cycling, and molecular synthesis rates. A number of different nuclei can be observed using MR, and those that are most commonly seen in brain disorders - in decreasing order of number of studies - are  $^1\text{H}$ ,  $^{31}\text{P}$ ,  $^{13}\text{C}$ ,  $^{19}\text{F}$ ,  $^{15}\text{N}$ ,  $^{23}\text{Na}$ , and  $^7\text{Li}$ , with the first three accounting for approximately 99% of all studies. Of these,  $^1\text{H}$  MRS is the most commonly applied in brain research, due to its higher sensitivity. At lower field strengths (1.5T and 3T), the number of metabolites that can be reliably quantified is relatively low. Metabolites that can be quantified include lactate, N-acetylaspartate, glutamate plus glutamine, creatine/phosphocreatine, choline-containing compounds, *myo*-inositol, and, in the rodent brain, taurine. Generally, little taurine is observed in primate brain, while in rodent brain taurine concentrations are quite high at  $\sim 5$  mM. As with MRI, the current movement towards higher field strengths offers important advantages for MRS, because of the increase in signal-to-noise ratio coupled with the increase in spectral dispersion. This leads to easier identification of the many overlapping resonances. At much higher field strengths, such as 7T in humans and 9.4T in animals, it is possible to quantify an increased number of metabolites (59,60).

Both  $^1\text{H}$  and  $^{31}\text{P}$  NMR have been applied in the study of AD in humans. A decrease of NAA in AD has been reported in at least 18 studies, including *in vitro* studies showing a correlation with AD pathology (61,62). In addition to the decrease in NAA, numerous studies have shown an increase in *myo*-inositol in AD (63,64). The pathological significance of this increase in *myo*-inositol is not yet clear. It is possible that the increase is due to gliosis or osmoregulatory problems, and it has been inferred that it may be related to changes in osmoregulation (43).  $^{31}\text{P}$  MRS studies of AD have shown abnormalities in the levels of membrane phospholipids and high energy metabolites that may depend on the severity of the illness (65).

In transgenic mouse models of AD,  $^1\text{H}$  MRS has been applied in four different studies. In the first study Dedeoglu *et al.* studied Tg2576 mice using both *in vivo* MRS at 4.7T and *in vitro* MRS at 11.7T (66). The data revealed decreased NAA and Glu, and increased taurine levels compared with the wild-type controls. In addition, they were able to detect a decrease in GSH from spectra *in vitro*. A second MRS study examined another model of AD: the APP/PS2 model. APP/PS2 mice showed a similar age-dependent decrease in NAA and Glu. A correlation with the plaque burden in 24-month-old animals was found, with little spectroscopic abnormalities before 16 months of age (67). The third MRS study examined the age-dependent spectroscopic changes noted in yet another mouse model of AD, the so-called APP/PS1 model. APP/PS1 mice start to develop plaques at an earlier age than the single transgene APP mice. In the APP/PS1 model, there was an age-dependent increase in *myo*-inositol and decreases in NAA and Glu were detected. The changes in *myo*-inositol were only significant after about 400 days of age (68). The observation of increased *myo*-inositol in APP/PS1 mice was very different from those made in the previous studies using APP and APP/PS2 mice. APP mice showed an increase in tau rather than *myo*-inositol and changes in neither *myo*-inositol nor taurine were reported in APP/PS2 mice. However, the increase in *myo*-inositol is consistent with observations in human AD studies. Marjanska *et al.* proposed that the ratio of NAA and *myo*-inositol might be a sensitive spectroscopic marker for following AD in human disease as well as in mouse models such as the APP/PS1 (68). However, if NAA and *myo*-inositol represent two different pathological mechanisms coupled to cellular processes in different cellular compartments, they can have independent temporal profiles as the disease progresses, and the ratio may mask this. For instance, in the study of APP/PS1 mice (68), NAA appears to decline fairly linearly with age, while the *myo*-inositol does not show an increase until after 400 days of age. This may reflect different roles and cellular compartments of NAA and *myo*-inositol, the former being primarily

neuronal and the latter glial (68). The fourth study examined 3xTgAD mice, and it was found that at 6 months of age NAA was already declining, while changes in other metabolite levels were not reported (43).

Although a decrease in NAA and an increase in either *myo*-inositol or taurine has been consistently observed in AD, these changes are not specific to only AD, since they have been shown to occur in other neurodegenerative diseases such as Huntington's disease, Parkinson's disease as well as in other brain disorders (43,69,70). Therefore, specific *in vivo* MRS markers of AD are still missing. While transgenic mouse models of AD might be instrumental in discovering new *in vivo* biomarkers of AD, the use of localized *in vivo* 1D MRS in mice is often hampered by low sensitivity of local measurements due to both the small size of the brain resulting in limited signal-to-noise ratio and low concentrations of several brain metabolites. Important neurotransmitters and other metabolites cannot be reliably distinguished due to overlapping or merging of their respective peaks in 1D MRS, although the recent development of high field magnets suitable for *in vivo* investigations in small animals has partly overcome this limitation. However, even with high-field magnets, the spectral dispersion in the proton spectra is limited, since most of the metabolites appear in a narrow spectral range of 5 ppm. Due to local field inhomogeneities in the small mouse brain, signals are broad (10-20 Hz), which results in a considerable overlap of resonances of numerous metabolites, especially those from coupled spin systems (71). Thus, ambiguity in assignment in 1D MRS is unavoidable for localized *in vivo* studies, especially in mouse brain. While 1D spectra at high magnetic field can yield accurate quantification of the known metabolites using analysis software such as LCmodel, which uses a linear combination of model spectra from a predefined basis set to simulate the measured spectra (72), unexpected metabolites are easily overlooked.

Spectral editing MRS sequences offer the possibility to resolve specific metabolites from overlapping regions in the spectra, thus facilitating their unambiguous resonance assignment and characterization *in vivo*. However, this requires pre-selection of metabolites of interest and only a single selected metabolite can be detected per measurement. A correct assignment of metabolite resonances *in vivo* is essential for their quantification under normal and various pathophysiological conditions and for identifying potential biomarkers of various brain disorders, including AD.

Compared to localized 1D MRS, localized 2D  $^1\text{H}$  MRS overcomes the problem of spectral overlap considerably, as the resonances are dispersed over a two-dimensional surface, allowing the separation and unambiguous assignment of resonances of several metabolites in a single measurement. Recently several 2D MRS sequences have been proposed and implemented for studying brain metabolism in human subjects, using clinical MRI scanners (71,73,74). The techniques based on localized variations of the COSY sequence appear most promising with regards to identifying metabolites that are unresolved in 1D MRS sequences due to spectral crowding. With regards to 2D MRS in small animal models, there have been a few reports of localized 2D MRS performed on rat brains (75,76), but thus far 2D MRS studies in the brains of mice have not yet been reported.

#### 1.4 Thesis scope

The rapidly expanding range of MR techniques for imaging neuropathologies and non-invasively assessing neurochemistry *in vivo*, in parallel with the rapid development of transgenic mouse models, offers great potential for the discovery of novel biomarkers of disease progression. Presently no definitive *in vivo* biomarker of AD is available, which impedes both clinical diagnosis in humans and drug discovery in transgenic animal models. Non-invasive rapid visualization of A $\beta$  plaque pathology and identification of new *in vivo* early biomarkers of AD using the various MR based techniques in transgenic mouse models of AD would not only facilitate intervention and enhance treatment success but would also contribute to understanding the mechanism of Alzheimer's disease. The *in vivo*  $\mu\text{MRI}$  approaches used for A $\beta$  plaque visualization thus far need further improvements in resolution and reduction in scan times. Furthermore, longitudinal MR studies which follow plaque development are required, to study plaque biology and its effects in the same animals as they age. In addition, longitudinal MR studies may prove beneficial for assessing the efficacy of amyloid reduction therapies currently under intense development by major pharmaceutical companies.

In addition to the use of A $\beta$  plaque imaging, some of the intrinsic MR parameters such as  $T_2$  relaxation times, which are sensitive to changes in the biophysical environment of water in tissues, may be applied as a sensitive marker for detecting early changes in Alzheimer's brain. These changes can be followed with time in longitudinal studies to identify correlations between plaque development and  $T_2$  relaxation times. Another possibility for identifying potential early biomarkers of AD is the application of *in vivo* localized magnetic resonance spectroscopy to study neurochemical changes resulting

from the disease. As described in the previous section, a major concern with one-dimensional MRS is that there is strong signal overlap which can make identification and precise quantification difficult, in particular for metabolites with coupled spin systems. Better signal dispersion, easier assignment and more accurate quantification can be achieved by the combination of: a) high magnetic field, since the dispersion of chemical shifts increases with magnetic field strength and b) localized 2D MR techniques, since the added dimension in a localized 2D MR spectrum yields an improved spectral resolution compared to conventional 1D MR spectra. In addition to unambiguous assignment opportunities of the various known neurometabolites *in vivo*, 2D MRS has great potential for resolving the resonances of brain metabolites at low concentration that are hidden by overlapping signals. This may be extremely beneficial in future studies, and significantly aid in detecting new biomarkers of the various neurodegenerative diseases, including AD. However, as previously mentioned, 2D MRS has thus far not been applied in studies using mouse models of disease. The specific aim of this thesis is to implement and optimize high resolution MR imaging methods to follow longitudinally the AD pathology in transgenic mouse models of AD, to optimize localized 2D MRS methods for the mouse brain, and to map the neurochemical composition of the brain of AD transgenic mice using high resolution 2D MRS.

**Chapter 2** of this thesis presents the basic theoretical background behind MRI and 1D/2D MRS techniques. In **chapter 3**, high-field  $\mu$ MRI methods have been optimized and successfully implemented to visualize A $\beta$  plaques in the Tg2576 transgenic mouse model of AD, and to follow A $\beta$  plaque development in the same transgenic mice with age. Additionally, the  $T_2$  relaxation times were studied as the mice aged, to study how AD progression and A $\beta$  plaque deposition influence the MR relaxometric properties of brain tissue. Described in **chapter 4** is the implementation and optimization of a localized 2D MR spectroscopic sequence, L-COSY, at 9.4T. Using this sequence, highly resolved 2D MR spectra were obtained, for the first time, from localized regions in the mouse brain *in vivo*. In **chapter 5**, two-dimensional MRS is applied to study the age-dependent metabolic changes in the brain of Tg2576 mice and correlate these changes with the severity of plaque deposition as observed by  $\mu$ MRI. **Chapter 6** provides a general discussion to the work presented in this thesis, and presents some future prospects.

---

**References**

1. Price JL, Davis PB, Morris JC, White DL. The Distribution Of Tangles, Plaques And Related Immunohistochemical Markers In Healthy Aging And Alzheimers-Disease. *Neurobiol Aging* 1991;12:295-312.
2. Terry RD, Masliah E, Salmon DP, Butters N, Deteresa R, Hill R, Hansen LA, Katzman R. Physical Basis Of Cognitive Alterations In Alzheimers-Disease - Synapse Loss Is The Major Correlate Of Cognitive Impairment. *Ann Neurol* 1991;30:572-580.
3. Burdick D, Soreghan B, Kwon M, Kosmoski J, Knauer M, Henschen A, Yates J, Cotman C, Glabe C. Assembly And Aggregation Properties Of Synthetic Alzheimers A4/Beta Amyloid Peptide Analogs. *J Biol Chem* 1992;267:546-554.
4. McGowan E, Eriksen J, Hutton M. A decade of modeling Alzheimer's disease in transgenic mice. *Trends In Genetics* 2006;22:281-289.
5. Petrella JR. Neuroimaging and early diagnosis of Alzheimer disease: A look to the future (vol 226, pg 315, 2003). *Radiology* 2003;227:613-613.
6. Gravina SA, Ho LB, Eckman CB, Long KE, Otvos L, Younkin LH, Suzuki N, Younkin SG. Amyloid-Beta Protein (A-Beta) In Alzheimers-Disease Brain - Biochemical And Immunocytochemical Analysis With Antibodies Specific For Forms Ending At A-Beta-40 Or A-Beta-42(43). *J Biol Chem* 1995;270:7013-7016.
7. Hardy J, Selkoe DJ. Medicine - The amyloid hypothesis of Alzheimer's disease: Progress and problems on the road to therapeutics. *Science* 2002;297:353-356.
8. Jack CR, Marjanska M, Wengenack TM, Reyes DA, Curran GL, Lin J, Preboske GM, Poduslo JF, Garwood M. Magnetic resonance imaging of Alzheimer's pathology in the brains of living transgenic mice: A new tool in Alzheimer's disease research. *Neuroscientist* 2007;13:38-48.
9. Cleary JP, Walsh DM, Hofmeister JJ, Shankar GM, Kuskowski MA, Selkoe DJ, Ashe KH. Natural oligomers of the amyloid-protein specifically disrupt cognitive function. *Nat Neurosci* 2005;8:79-84.
10. Spires TL, Meyer-Luehmann M, Stern EA, McLean PJ, Skoch J, Nguyen PT, Bacskai BJ, Hyman BT. Dendritic spine abnormalities in amyloid precursor protein transgenic mice demonstrated by gene transfer and intravital multiphoton microscopy. *J Neurosci* 2005;25:7278-7287.
11. Tsai J, Grutzendler J, Duff K, Gan WB. Fibrillar amyloid deposition leads to local synaptic abnormalities and breakage of neuronal branches. *Nat Neurosci* 2004;7:1181-1183.

12. Lewis J, Dickson DW, Lin WL, Chisholm L, Corral A, Jones G, Yen SH, Sahara N, Skipper L, Yager D, Eckman C, Hardy J, Hutton M, McGowan E. Enhanced neurofibrillary degeneration in transgenic mice expressing mutant tau and APP. *Science* 2001;293:1487-1491.
13. SantaCruz K, Lewis J, Spires T, Paulson J, Kotilinek L, Ingelsson M, Guimaraes A, DeTure M, Ramsden M, McGowan E, Forster C, Yue M, Orne J, Janus C, Mariash A, Kuskowski M, Hyman B, Hutton M, Ashe KH. Tau suppression in a neurodegenerative mouse model improves memory function. *Science* 2005;309:476-481.
14. Lehericy S, Marjanska M, Mesrob L, Sarazin M, Kinkingnehun S. Magnetic resonance imaging of Alzheimer's disease. *European Radiology* 2007;17:347-362.
15. Wengenack TM, Whelan S, Curran GL, Duff KE, Poduslo JF. Quantitative histological analysis of amyloid deposition in Alzheimer's double transgenic mouse brain. *Neuroscience* 2000;101:939-944.
16. Geula C. Pathological diagnosis of Alzheimer's disease. In: *The early diagnosis of Alzheimer's disease*. Totowa, NJ: Humana, 2000; 65–82.
17. Braak H, Braak E. Neuropathological Staging Of Alzheimer-Related Changes. *Acta Neuropathol* 1991;82:239-259.
18. Holcomb L, Gordon MN, McGowan E, Yu X, Benkovic S, Jantzen P, Wright K, Saad I, Mueller R, Morgan D, Sanders S, Zehr C, O'Campo K, Hardy J, Prada CM, Eckman C, Younkin S, Hsiao K, Duff K. Accelerated Alzheimer-type phenotype in transgenic mice carrying both mutant amyloid precursor protein and presenilin 1 transgenes. *Nat Med* 1998;4:97-100.
19. Hsiao K, Chapman P, Nilsen S, Eckman C, Harigaya Y, Younkin S, Yang FS, Cole G. Correlative memory deficits, A beta elevation, and amyloid plaques in transgenic mice. *Science* 1996;274:99-102.
20. Wengenack TM, Curran GL, Poduslo JF. Targeting Alzheimer amyloid plaques in vivo. *Nat Biotechnol* 2000;18:868-872.
21. Irizarry MC, McNamara M, Fedorchak K, Hsiao K, Hyman BT. APP(Sw) transgenic mice develop age-related A beta deposits and neuropil abnormalities, but no neuronal loss in CA1. *J Neuropathol Exp Neurol* 1997;56:965-973.
22. Irizarry MC, Soriano F, McNamara M, Page KJ, Schenk D, Games D, Hyman BT. A beta deposition is associated with neuropil changes, but not with overt neuronal loss in the human amyloid precursor protein V717F (PDAPP) transgenic mouse. *J Neurosci* 1997;17:7053-7059.

23. Allen B, Ingram E, Takao M, Smith MJ, Jakes R, Virdee K, Yoshida H, Holzer M, Craxton M, Emson PC, Atzori C, Migheli A, Crowther RA, Ghetti B, Spillantini MG, Goedert M. Abundant tau filaments and nonapoptotic neurodegeneration in transgenic mice expressing human P301S tau protein. *J Neurosci* 2002;22:9340-9351.
24. Lewis J, McGowan E, Rockwood J, Melrose H, Nacharaju P, Van Slegtenhorst M, Gwinn-Hardy K, Murphy MP, Baker M, Yu X, Duff K, Hardy J, Corral A, Lin WL, Yen SH, Dickson DW, Davies P, Hutton M. Neurofibrillary tangles, amyotrophy and progressive motor disturbance in mice expressing mutant (P301L) tau protein. *Nature Genet* 2000;25:402-405.
25. Oddo S, Caccamo A, Shepherd JD, Murphy MP, Golde TE, Kaye R, Metherate R, Mattson MP, Akbari Y, LaFerla FM. Triple-transgenic model of Alzheimer's disease with plaques and tangles: Intracellular A beta and synaptic dysfunction. *Neuron* 2003;39:409-421.
26. Perez M, Ribe E, Rubio A, Lim F, Moran MA, Ramos PG, Ferrer I, Isla MTG, Avila J. Characterization of a double (amyloid precursor protein-tau) transgenic: Tau phosphorylation and aggregation. *Neuroscience* 2005;130:339-347.
27. Oddo S, Caccamo A, Kitazawa M, Tseng BP, LaFerla FM. Amyloid deposition precedes tangle formation in a triple transgenic model of Alzheimer's disease. *Neurobiol Aging* 2003;24:1063-1070.
28. Oddo S, Caccamo A, Tran L, Lambert MP, Glabe CG, Klein WL, LaFerla FM. Temporal profile of amyloid-beta (A beta) oligomerization in an in vivo model of Alzheimer disease - A link between A beta and tau pathology. *J Biol Chem* 2006;281:1599-1604.
29. Sturchler-Pierrat C, Abramowski D, Duke M, Wiederhold KH, Mistl C, Rothacher S, Ledermann B, Burki K, Frey P, Paganetti PA, Waridel C, Calhoun ME, Jucker M, Probst A, Staufenbiel M, Sommer B. Two amyloid precursor protein transgenic mouse models with Alzheimer disease-like pathology. *Proc Natl Acad Sci U S A* 1997;94:13287-13292.
30. Duff K, Eckman C, Zehr C, Yu X, Prada CM, Pereztur J, Hutton M, Buee L, Harigaya Y, Yager D, Morgan D, Gordon MN, Holcomb L, Refolo L, Zenk B, Hardy J, Younkin S. Increased amyloid-beta 42(43) in brains of mice expressing mutant presenilin 1. *Nature* 1996;383:710-713.



31. Borchelt DR, Ratovitski T, vanLare J, Lee MK, Gonzales V, Jenkins NA, Copeland NG, Price DL, Sisodia SS. Accelerated amyloid deposition in the brains of transgenic mice coexpressing mutant presenilin 1 and amyloid precursor proteins. *Neuron* 1997;19:939-945.
32. Tanemura K, Akagi T, Murayama M, Kikuchi N, Murayama O, Hashikawa T, Yoshiike Y, Park JM, Matsuda K, Nakao S, Sun XY, Sato S, Yamaguchi H, Takashima A. Formation of filamentous tau aggregations in transgenic mice expressing V337M human tau. *Neurobiol Dis* 2001;8:1036-1045.
33. Tatebayashi Y, Miyasaka T, Chui DH, Akagi T, Mishima K, Iwasaki K, Fujiwara M, Tanemura K, Murayama M, Ishiguro K, Planel E, Sato S, Hashikawa T, Takashima A. Tau filament formation and associative memory deficit in aged mice expressing mutant (R406W) human tau. *Proc Natl Acad Sci U S A* 2002;99:13896-13901.
34. Ramsden M, Kotilinek L, Forster C, Paulson J, McGowan E, SantaCruz K, Guimaraes A, Yue M, Lewis J, Carlson G, Hutton M, Ashe KH. Age-dependent neurofibrillary tangle formation, neuron loss, and memory impairment in a mouse model of human tauopathy (P301L). *J Neurosci* 2005;25:10637-10647.
35. Andorfer C, Kress Y, Espinoza M, de Silva R, Tucker KL, Barde YA, Duff K, Davies P. Hyperphosphorylation and aggregation of tau in mice expressing normal human tau isoforms. *J Neurochem* 2003;86:582-590.
36. Klunk WE, Engler H, Nordberg A, Wang YM, Blomqvist G, Holt DP, Bergstrom M, Savitcheva I, Huang GF, Estrada S, Ausen B, Debnath ML, Barletta J, Price JC, Sandell J, Lopresti BJ, Wall A, Koivisto P, Antoni G, Mathis CA, Langstrom B. Imaging brain amyloid in Alzheimer's disease with Pittsburgh Compound-B. *Ann Neurol* 2004;55:306-319.
37. Sair HI, Doraiswamy PM, Petrella JR. In vivo amyloid imaging in Alzheimer's disease. *Neuroradiology* 2004;46:93-104.
38. Kantarci K, Jack CR. Neuroimaging in Alzheimer disease: An evidence-based review. *Neuroimaging Clin N Am* 2003;13:197-209.
39. Bookstein FL. "Voxel-based morphometry" should not be used with imperfectly registered images. *Neuroimage* 2001;14:1454-1462.
40. Helpert JA, Lee SP, Falangola MF, Dyakin VV, Bogart A, Ardekani B, Duff K, Branch C, Wisniewski T, de Leon MJ, Wolf O, O'Shea J, Nixon RA. MRI assessment of neuropathology in a transgenic mouse model of Alzheimer's disease. *Magn Reson Med* 2004;51:794-798.

41. Beckmann N, Schuler A, Mueggler T, Meyer EP, Wiederhold KH, Staufenbiel M, Krucker T. Age-dependent cerebrovascular abnormalities and blood flow disturbances in APP23 mice modeling Alzheimer's disease. *J Neurosci* 2003;23:8453-8459.
42. Alsop DC, Detre JA, Grossman M. Assessment of cerebral blood flow in Alzheimer's disease by spin-labeled magnetic resonance imaging. *Ann Neurol* 2000;47:93-100.
43. Choi JK, Dedeoglu A, Jenkins BG. Application of MRS to mouse models of neurodegenerative illness. *NMR Biomed* 2007;20:216-237.
44. Benveniste H, Einstein G, Kim KR, Hulette C, Johnson A. Detection of neuritic plaques in Alzheimer's disease by magnetic resonance microscopy. *Proc Natl Acad Sci U S A* 1999;96:14079-14084.
45. Dhenain M, Privat N, Duyckaerts C, Jacobs RE. Senile plaques do not induce susceptibility effects in T<sub>2</sub>\*-weighted MR microscopic images. *NMR Biomed* 2002;15:197-203.
46. Zhang J, Yarowsky P, Gordon MN, Di Carlo G, Munireddy S, van Zijl PCM, Mori S. Detection of amyloid plaques in mouse models of Alzheimer's disease by magnetic resonance imaging. *Magn Reson Med* 2004;51:452-457.
47. Lee SP, Falangola MF, Nixon RA, Duff K, Helpert JA. Visualization of beta-amyloid plaques in a transgenic mouse model of Alzheimer's disease using MR microscopy without contrast reagents. *Magn Reson Med* 2004;52:538-544.
48. Dhenain M, Delatour B, Walczak C, Volk A. Passive staining: A novel ex vivo MRI protocol to detect amyloid deposits in mouse models of Alzheimer's disease. *Magn Reson Med* 2006;55:687-693.
49. Poduslo JF, Wengenack TM, Curran GL, Wisniewski T, Sigurdsson EM, Macura SI, Borowski BJ, Jack CR. Molecular targeting of Alzheimer's amyloid plaques for contrast-enhanced magnetic resonance imaging. *Neurobiol Dis* 2002;11:315-329.
50. Higuchi M, Iwata N, Matsuba Y, Sato K, Sasamoto K, Saido TC. <sup>19</sup>F and <sup>1</sup>H MRI detection of amyloid beta plaques in vivo. *Nat Neurosci* 2005;8:527-533.
51. Wadghiri YZ, Sigurdsson EM, Sadowski M, Elliott JI, Li YS, Scholtzova H, Tang CY, Aguinaldo G, Pappolla M, Duff K, Wisniewski T, Turnbull DH. Detection of Alzheimer's amyloid in Transgenic mice using magnetic resonance microimaging. *Magn Reson Med* 2003;50:293-302.

52. Jack CR, Garwood M, Wengenack TM, Borowski B, Curran GL, Lin J, Adriany G, Grohn IHJ, Grimm R, Poduslo JF. In vivo visualization of Alzheimer's amyloid plaques by magnetic resonance imaging in transgenic mice without a contrast agent. *Magn Reson Med* 2004;52:1263-1271.
53. Jack CR, Wengenack TM, Reyes DA, Garwood M, Curran GL, Borowski BJ, Lin J, Preboske GM, Holasek SS, Adriany G, Poduslo JF. In vivo magnetic resonance microimaging of individual amyloid plaques in Alzheimer's transgenic mice. *J Neurosci* 2005;25:10041-10048.
54. Vanhoutte G, Dewachter I, Borghgraef P, Van Leuven F, Van der Linden A. Noninvasive in vivo MRI detection of neuritic plaques associated with iron in APP[V717I] transgenic mice, a model for Alzheimer's disease. *Magn Reson Med* 2005;53:607-613.
55. Borthakur A, Gur T, Wheaton AJ, Corbo M, Trojanowski JQ, Lee VMY, Reddy R. In vivo measurement of plaque burden in a mouse model of Alzheimer's disease. *J Magn Reson Imaging* 2006;24:1011-1017.
56. Falangola MF, Dyakin VV, Lee SP, Bogart A, Babb JS, Duff K, Nixon R, Helpert JA. Quantitative MRI reveals aging-associated T<sub>2</sub> changes in mouse models of Alzheimer's disease. *NMR Biomed* 2007;20:343-351.
57. El Tayara NET, Volk A, Dhenain M, Delatour B. Transverse relaxation time reflects brain amyloidosis in young APP/PS1 transgenic mice. *Magn Reson Med* 2007;58:179-184.
58. Falangola MF, Ardekani BA, Lee SP, Babb JS, Bogart A, Dyakin VV, Nixon R, Duff K, Helpert JA. Application of a non-linear image registration algorithm to quantitative analysis of T<sub>2</sub> relaxation time in transgenic mouse models of AD pathology. *J Neurosci Methods* 2005;144:91-97.
59. Pfeuffer J, Tkac I, Provencher SW, Gruetter R. Toward an in vivo neurochemical profile: Quantification of 18 metabolites in short-echo-time H-1 NMR spectra of the rat brain. *J Magn Reson* 1999;141:104-120.
60. Tkac I, Andersen P, Adriany G, Merkle H, Ugurbil K, Gruetter R. In vivo H-1 NMR spectroscopy of the human brain at 7 T. *Magn Reson Med* 2001;46:451-456.
61. Klunk WE, Xu C, Panchalingam K, McClure RJ, Pettegrew JW. Quantitative H-1 and P-31 MRS of PCA extracts of postmortem Alzheimer's disease brain. *Neurobiol Aging* 1996;17:349-357.

62. Mohanakrishnan P, Fowler AH, Vonsattel JP, Husain MM, Jolles PR, Liem P, Komoroski RA. An In-Vitro H-1 Nuclear-Magnetic-Resonance Study Of The Temporoparietal Cortex Of Alzheimer Brains. *Exp Brain Res* 1995;102:503-510.
63. Jessen F, Block W, Traber F, Keller E, Flacke S, Papassotiropoulos A, Lamerichs R, Heun R, Schild HH. Proton MR spectroscopy detects a relative decrease of N-acetylaspartate in the medial temporal lobe of patients with AD. *Neurology* 2000;55:684-688.
64. Miller BL. A Review Of Chemical Issues In H-1-Nmr Spectroscopy - N-Acetyl-L-Aspartate, Creatine And Choline. *NMR Biomed* 1991;4:47-52.
65. Pettegrew JW, Panchalingam K, Moosy J, Martinez J, Rao G, Boller F. Correlation Of P-31 Magnetic-Resonance Spectroscopy And Morphologic Findings In Alzheimers-Disease. *Arch Neurol* 1988;45:1093-1096.
66. Dedeoglu A, Choi JK, Cormier K, Kowall NW, Jenkins BG. Magnetic resonance spectroscopic analysis of Alzheimer's disease mouse brain that express mutant human APP shows altered neurochemical profile. *Brain Res* 2004;1012:60-65.
67. von Kienlin M, Kunnecke B, Metzger F, Steiner G, Richards JG, Ozmen L, Jacobsen H, Loetscher H. Altered metabolic profile in the frontal cortex of PS2APP transgenic mice, monitored throughout their life span. *Neurobiol Dis* 2005;18:32-39.
68. Marjanska M, Curran GL, Wengenack TM, Henry PG, Bliss RL, Poduslo JF, Jack CR, Ugurbil K, Garwood M. Monitoring disease progression in transgenic mouse models of Alzheimer's disease with proton magnetic resonance spectroscopy. *Proc Natl Acad Sci U S A* 2005;102:11906-11910.
69. Tsang TA, Woodman B, McLoughlin GA, Griffin JL, Tabrizi SJ, Bates GP, Holmes E. Metabolic characterization of the R6/2 transgenic mouse model of Huntington's disease by high-resolution MAS H-1 NMR spectroscopy. *J Proteome Res* 2006;5:483-492.
70. Boska MD, Lewis TB, Destache CJ, Benner EJ, Nelson JA, Uberti M, Mosley RL, Gendelman HE. Quantitative H-1 magnetic resonance spectroscopic imaging determines therapeutic immunization efficacy in an animal model of Parkinson's disease. *J Neurosci* 2005;25:1691-1700.
71. Thomas MA, Yue K, Binesh N, Davanzo P, Kumar A, Siegel B, Frye M, Curran J, Lufkin R, Martin P, Guze B. Localized two-dimensional shift correlated MR spectroscopy of human brain. *Magn Reson Med* 2001;46:58-67.
72. Provencher SW. Estimation Of Metabolite Concentrations From Localized In-Vivo Proton Nmr-Spectra. *Magn Reson Med* 1993;30:672-679.

73. Thomas MA, Hattori N, Umeda M, Sawada T, Naruse S. Evaluation of two-dimensional L-COSY and PRESS using a 3 T MRI scanner: from phantoms to human brain in vivo. *NMR Biomed* 2003;16:245-251.
74. Binesh N, Yue K, Fairbanks L, Thomas MA. Reproducibility of localized 2D correlated MR spectroscopy. *Magn Reson Med* 2002;48:942-948.
75. Delmas F, Beloeil JC, van der Sanden BPJ, Nicolay K, Gillet B. Two-voxel localization sequence for in vivo two-dimensional homonuclear correlation spectroscopy. *J Magn Reson* 2001;149:119-125.
76. Welch JWR, Bhakoo K, Dixon RM, Styles P, Sibson NR, Blamire AM. In vivo monitoring of rat brain metabolites during vigabatrin treatment using localized 2D-COSY. *NMR Biomed* 2003;16:47-54.

## 2 Theoretical background: MRI and MRS

---

Without a basic knowledge of MRI physics, basic imaging phenomena, including the source of image contrast, relaxometry and 2D spectroscopy, would be very difficult to explain. This chapter gives a brief introduction of MR physics with emphasis on fast spin echo imaging, transverse relaxation mapping and 2D correlated spectroscopy.

MR is based upon the interaction between an applied magnetic field and a nucleus with a nuclear magnetic moment or “spin” (1-3). Several nuclei, including  $^1\text{H}$ ,  $^{31}\text{P}$ ,  $^{13}\text{C}$ ,  $^{15}\text{N}$ , and  $^{19}\text{F}$  have nuclear magnetic moments corresponding with spin  $\frac{1}{2}$  and are most suitable for detection by magnetic resonance (2-4). Protons are the most abundant spin  $\frac{1}{2}$  nuclei in living organisms and they have the best NMR sensitivity (2-4). For this reason protons are the most frequently studied nuclei. As a crude simplification, nuclear spins can be thought of as small magnets. When placed in an external magnetic field ( $B_0$ ) a large number of proton spins will be aligned parallel to  $B_0$ , with a somewhat smaller number oriented anti-parallel. This orientation yields a net nuclear magnetization and a net magnetization vector  $M_z$  parallel to  $B_0$  (Fig. 2.1a).

When tilted away from the magnetic field, the spins precess about the axis of  $B_0$  (commonly taken as the  $z$ -axis) at a frequency proportional to the magnitude of the external field, according to

$$\nu_0 = \omega_0 / 2\pi = \gamma B_0 / 2\pi, \quad (2.1)$$

with  $\nu_0$  the Larmor frequency in MHz, and  $\gamma$  the gyromagnetic ratio. For protons  $\gamma/2\pi = 42.576 \text{ MHz}\cdot\text{Tesla}^{-1}$ . When a second, time-dependent magnetic field ( $B_1$ ) is applied perpendicular to  $B_0$ , by using an RF pulse at the Larmor frequency, the magnetization vector  $M_z$  will rotate away from the  $z$ -axis towards the  $xy$ -plane. The angle of rotation ( $\alpha$ ), or flip angle, of  $M_z$  around  $B_1$  is defined as

$$\alpha = \gamma B_1 \tau / 2\pi, \quad (2.2)$$

with  $\tau$  the time during which the RF pulse field  $B_1$  is switched on.

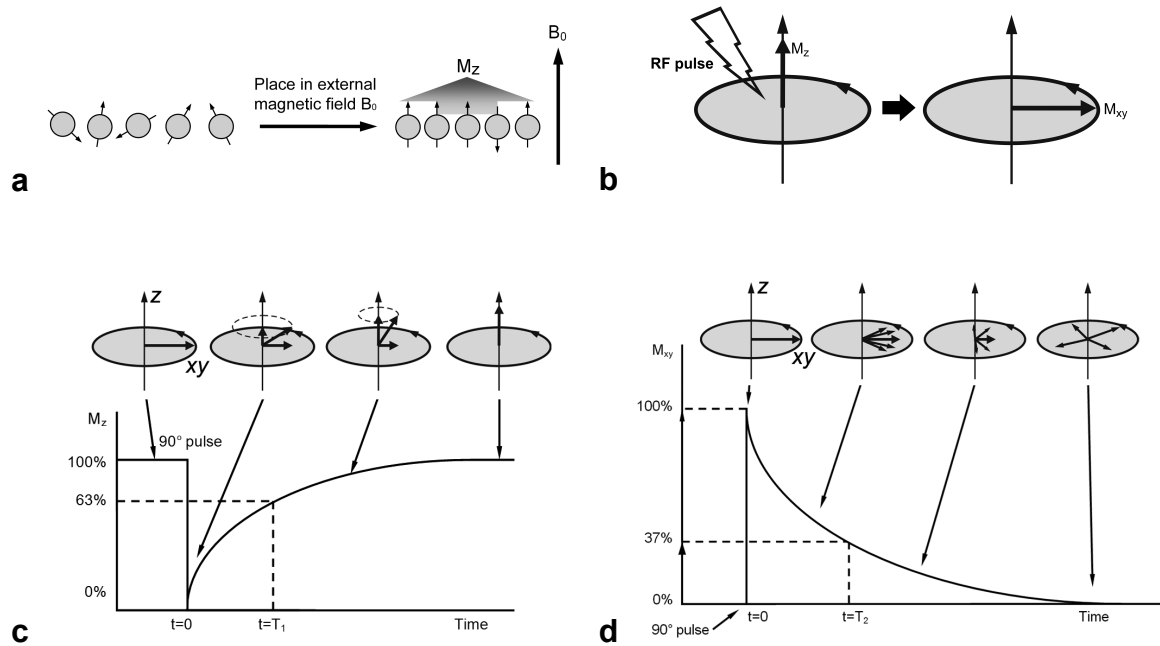


Figure 2.1: MR basics. (a) Protons ( $^1H$ ) possess a magnetic moment, or “spin”. When placed in an external field  $B_0$ , the majority of these spins align parallel to  $B_0$  (along the z-axis), resulting in a magnetization vector  $M_z$ . (b) Application of a  $90^\circ$  RF pulse flips  $M_z$  into the xy-plane (perpendicular to  $B_0$ ), resulting in magnetization vector  $M_{xy}$  and phase coherence between spins. (c)  $M_z$  will return to its original distribution along the z-axis through  $T_1$  relaxation (eq. 2.3). (d) Loss of phase coherence, and thereby loss of magnetization in the xy-plane, is determined by  $T_2$  relaxation (eq. 2.4).

After application of a  $90^\circ$  pulse the magnetization vector will be in the xy-plane, and the spins will be in phase coherence;  $M_z$  will be zero and  $M_{xy}$  will be at a maximum (Fig. 2.1b). This process is commonly referred to as pulse excitation. After the RF pulse is switched off, the net magnetization vector will start reverting back to its equilibrium state as a result of a process which is called relaxation. The recovery process along the longitudinal axis is called  $T_1$  relaxation, spin-lattice relaxation or longitudinal relaxation (Fig. 2.1c) and is described as:

$$M_z(t) = M_{z_{\max}} \left( 1 - e^{-\frac{t}{T_1}} \right) \quad (2.3)$$

During this process, the nuclei are giving up energy to their immediate surroundings. The dephasing process in the transverse plane (the plane orthogonal to  $B_0$ ) is referred to as  $T_2$  relaxation, or spin-spin relaxation.

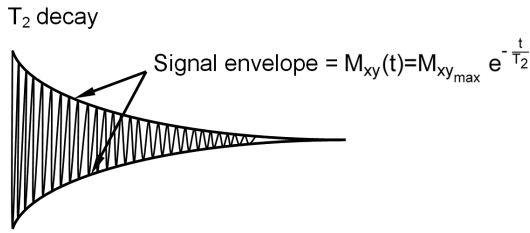


Figure 2.2: Free induction decay; after a single RF pulse the signal detected in the transverse plane is sinusoidal in shape and decays to zero over time under influence of the transverse relaxation.

In this process, nuclei exchange energy with each other and the spins lose phase coherence. To first order the net magnetization in the  $xy$ -plane decays exponentially to zero over time. The rate at which this occurs is dependent on  $T_2$  (Fig. 2.1d) and the  $T_2$  process is described as:

$$M_{xy}(t) = M_{xy_{max}} e^{-\frac{t}{T_2}}. \quad (2.4)$$

In reality the signal will decay at a faster rate than  $T_2$  due to field inhomogeneities and magnetic susceptibility differences. This shorter relaxation rate is known as  $T_2^*$ , and can be determined according to

$$\frac{1}{T_2^*} = \frac{1}{T_2} + \frac{1}{T_{2M}} + \frac{1}{T_{2MS}}. \quad (2.5)$$

Here  $T_{2M}$  is the dephasing due to inhomogeneity of the applied field, and  $T_{2MS}$  is the dephasing due to magnetic susceptibility differences (4).

An RF coil placed in the transverse plane will detect the transverse component of the net magnetization vector as it precesses around  $B_0$ . The length of the magnetization vector is the magnitude of the signal, while the angle between the magnetization vector and the  $y$ -axis is referred to as the phase of the signal. The decaying sinusoidal signal detected in the transverse plane (Fig. 2.2) after a single RF pulse is known as the free induction decay. Depending on the sample the FID can contain multiple resonance frequencies. A simple spectrum can be obtained from the FID by converting it from the time domain to the frequency domain using the Fourier transform. The resulting spectrum contains peaks for the various different frequencies contained within the FID.

## 2.1 Magnetic Resonance Imaging

In the above model where nuclei are placed in a homogeneous magnetic field, and an RF excitation pulse is followed by relaxation of the nuclei, the entire sample would only give a single signal. In other words, in the above highly simplified system, the NMR signal



cannot be spatially resolved. In order to assign spatial information to smaller volume units, commonly denoted as voxels, an additional step is required. From the basic equation in the previous section, it is clear that the resonance frequencies of spins depend on the magnetic field strength in which they reside. Spatial variations in frequencies can be translated to spatial information and subsequently to an image. Assigning spatial information to the spins is achieved by adding a magnetic field gradient inside the MR scanner. The gradient field is parallel to  $B_0$  and its strength varies with position relative to  $B_0$ . The gradient has three components,  $G_x$ ,  $G_y$ , and  $G_z$ , associated with the  $x$ ,  $y$ , or  $z$  spatial axis, respectively. The spins experience different field strengths depending on where they are within the gradient field. Positional dependence of the field strength and resonance frequencies can be calculated according to:

$$B(\mathbf{r})=B_0+\mathbf{r}\mathbf{G} \quad (2.6)$$

$$\omega(\mathbf{r})=\gamma B(\mathbf{r})=\gamma B_0+\gamma\mathbf{r}\mathbf{G} \quad (2.7)$$

Here  $B(\mathbf{r})$  and  $\omega(\mathbf{r})$  are the position dependent field strength and resonance frequency, respectively. The position in the magnetic field is denoted by the vector  $\mathbf{r}$  and the magnitude and direction of the gradient as  $\mathbf{G}$  (2,4). Spins in different volume units within the field gradient experience a different magnetic field. Each “sub-field” is associated with a different Larmor frequency. The initial localization step is most commonly in the selection of the desired cross-section or “slice”. This is achieved by applying a gradient along the  $z$ -axis in combination with an excitation pulse. This RF pulse excites only the spins in the desired slice, while leaving adjacent spins unaffected, as they have a different resonance frequency due to the applied  $z$ -gradient. Within the acquired slice, the  $x$ - and  $y$ -gradients are applied to assign the spins at each position within the slice with a unique frequency and phase. The gradients in this example are often referred to as the **slice selection-** ( $G_z$ ), the **frequency encoding-** ( $G_x$ ) and the **phase encoding gradients** ( $G_y$ ).  $G_x$  is usually kept constant over the course of an experiment, thus assigning a different frequency to each position along the  $x$ -axis.  $G_y$  is stepped a number of times each scan, depending on the desired resolution in the  $y$ -direction.  $G_y$  applies a specific phase angle to the transverse magnetization vector. While  $G_y$  is switched on, each transverse magnetization vector has its own unique Larmor frequency. When  $G_y$  is subsequently switched off, the spins return to the frequency they had prior to phase encoding, however, the phase angle of each transverse magnetization vector is different. A variety of imaging pulse sequences can be created by combining slice selection, phase encoding and frequency encoding. In two-dimensional experiments, all three of the above components

are used in an orthogonal manner. In true 3D imaging experiments, two phase encoding directions and one frequency encoding direction are used.

Among the most important and widely used pulse sequences for MRI are the spin echo sequence and the gradient echo sequence. GE sequences use a slice selective pulse of  $90^\circ$  or less, and subsequently employ the gradient coils for producing an echo. This is done by first applying a negative frequency-encoding gradient, which is subsequently reversed, causing the spins to rephase and form an echo. Following signal detection the phase coherence of the precessing spins in the transverse plane is dephased or “spoiled” using spoiler gradients, thus ensuring contribution of only the longitudinal magnetization to the net magnetization  $M$  at the time of the next excitation pulse (4). Conversely, SE sequences use a slice selective  $90^\circ$  pulse for excitation, followed by a  $180^\circ$  pulse at  $t = TE/2$ . The  $180^\circ$  pulse serves to reverse or refocus the spins. This produces an echo at  $t = TE$ . During SE acquisition, the phase encoding gradient is applied following the  $90^\circ$  pulse, and the frequency encoding, or read out-, gradient is applied centered around the echo at  $t = TE$  (4). The TE in these examples is the echo time, and is measured from the center of the excitation pulse to the center of the echo. As multiple excitation-refocus-echo steps are needed to build up an entire image, the sequence is looped several times, depending on the desired resolution. The repetition time is defined as the time from the start of one loop of the sequence to the next.

### **2.1.1 Rapid acquisition with relaxation-enhancement imaging**

Rapid acquisition with relaxation-enhancement imaging (5) is a fast spin echo imaging sequence in which multiple spin echoes are generated by employing multiple  $180^\circ$  refocusing pulses (Fig. 2.3). Each refocused echo is acquired after having experienced a different phase-encoding value. Because refocusing of the transverse magnetization is inherent in the sequence, it is less vulnerable to susceptibility-induced dephasing than gradient echo sequences, but it is substantially faster to apply than a spin-echo sequence with a single-phase encoding step per repetition time.

The primary contrast is  $T_2$ -based, although this can be mixed with  $T_1$  and perfusion effects by combining it with the inversion recovery sequence (IR-RARE). The contrast in the final image can be modified depending on the choice of TE and TR. Choosing a long TR, and a relatively long TE, for example, will yield a  $T_2$ -weighted image, where elements with long  $T_2$  will appear bright, and elements with a short  $T_2$  will appear dark. A practical implementation of RARE imaging in visualizing Alzheimer’s A $\beta$  plaques is demonstrated in chapter 3.

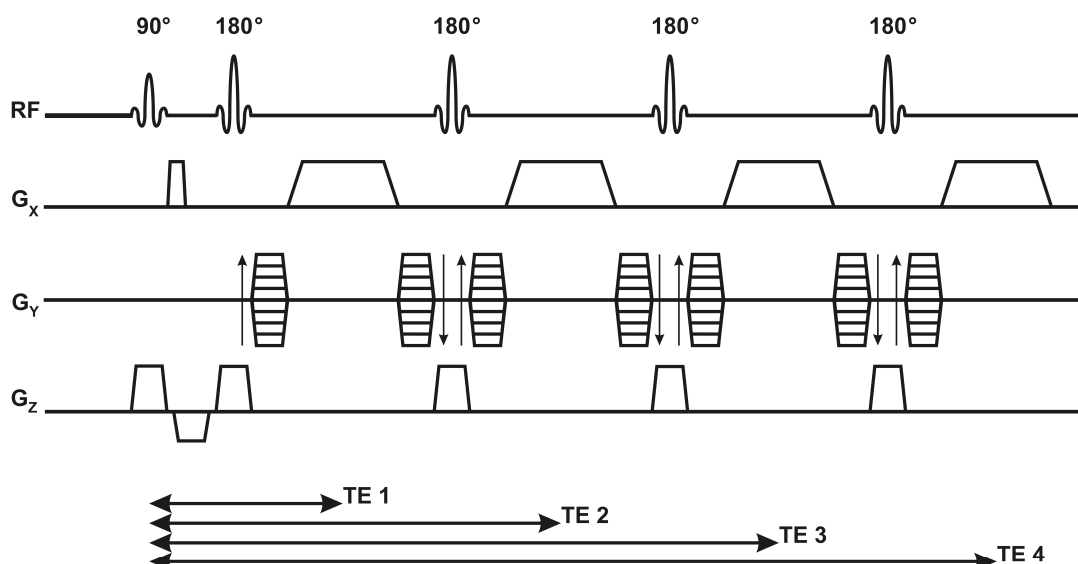


Figure 2.3: RARE pulse sequence: A four-segment (RARE factor of 4) version is shown. Each cycle has four phase encoding steps; the sequence will be looped until the desired number of phase encoding steps is reached. As this sequence acquires four times the data per loop as a standard SE sequence, the scan time is roughly 25% shorter than for an equivalent SE sequence. The effective TE is the TE time during which the  $G_y = 0$  lines of data are acquired (4).

### 2.1.2 Transverse relaxation mapping

The relaxation times ( $T_2$  and  $T_1$ ) mentioned in the introductory section of this chapter may vary depending on tissue type, protein molecular structure, water content or presence of metal ions such as iron or manganese. As mentioned in chapter 1, disease mechanisms influence the composition of tissue, and can have an effect on the tissue specific relaxation rates. As AD pathology is predominantly visualized in MR research using  $T_2$ -weighted methods,  $T_2$  mapping has been proposed as a tool to diagnose and/or predict AD (see chapter one).

Considering that the amount of magnetization present in the  $xy$ -plane depends on  $T_2$ , and that by modifying the TE value of a spin echo technique different  $T_2$ -weighting factors are obtained, it is possible to calculate the value of  $T_2$  from a series of SE images with different echo times. As the signal intensity in these images is related to the magnetization in the  $xy$  plane,  $T_2$  can be calculated by substituting the measured signal intensity for  $M_{xy}(t)$ , according to

$$M_{xy}(t) = M_{xy_{\max}} e^{-\frac{t}{T_2}}, \quad (2.8)$$

where  $t$  equals the experimental TE mentioned above.

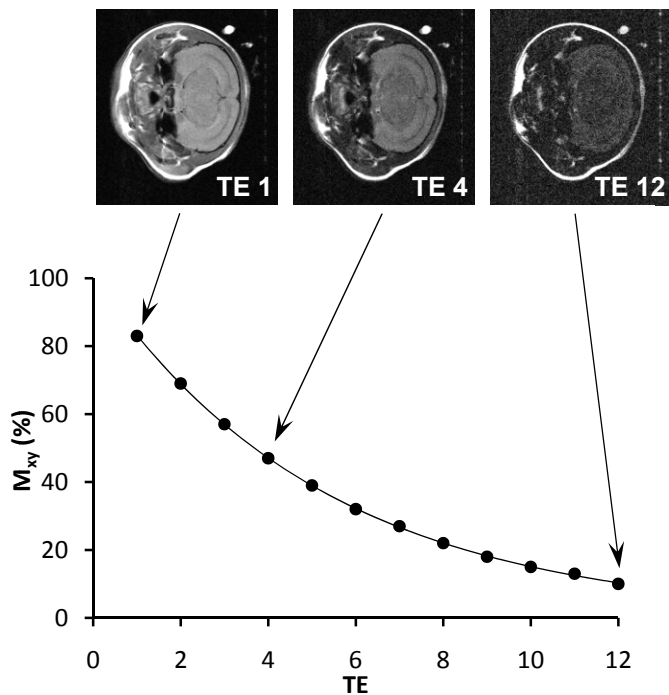


Figure 2.4: To calculate  $T_2$  for specific regions of interest, a series of spin echo images is recorded, each with increasing TE. As TE increases, the signal intensity will decrease. This is plotted in the adjoining graph. An exponential decay function can be fit to this data, which allows calculation of the  $T_2$  relaxation. As the transverse relaxation rate is calculated according to (eq 2.8),  $T_2$  can be obtained in a relatively straightforward manner.

This can be calculated for the individual voxels of the sample, thus creating a  $T_2$  map, or for specific regions of interest, by averaging the signal intensities for the pixels located within the ROI, and calculating the average  $T_2$  for that region. Since an SE technique is used here, the signal is rephased before detection, which causes the effects of field inhomogeneities and susceptibilities to cancel. Hence, the calculated  $T_2$  is the “true”  $T_2$  and not  $T_2^*$ . Chapter 3 contains a practical implementation of this technique.

## 2.2 Magnetic Resonance Spectroscopy

The most basic method to obtain MR spectra is by placing a sample within the magnetic field of an MR scanner, exciting the spins in the sample by means of an RF pulse, and recording the FID as the spins relax back to their equilibrium state. Subsequent Fourier transformation of the recorded signal yields the magnetic resonance spectrum. Despite the numerous variations on this sequence that can be implemented, the obtained spectrum will always be of the entire sample within the scanner.

For *in vivo* applications it is desirable to localize the spectroscopic measurement in a specific volume of interest, or voxel. In the first *in vivo* experiments, the signal was approximately localized using a coil suitable for the observed organ, such as a surface coil to study the brain. However, a wide variety of more accurate spatial localization techniques using  $B_0$  gradients have since been developed. These methods rely on the selection of spatially selective slices by the application of frequency-selective RF pulses

in the presence of a magnetic field gradient. Some of them require several acquisitions to achieve complete localization, whereas others can achieve localization in a single experiment (6), (Chap. 5). Among the most popular methods is point resolved spectroscopy (7,8). The PRESS sequence (Fig. 2.5a) is a double spin-echo sequence. Three slice-selective pulses ( $90^\circ$ ,  $180^\circ$ ,  $180^\circ$ ) along three orthogonal axes define three orthogonal slices, and make it possible to localize the signal in the voxel formed by the intersection of the three slices (Fig. 2.5b).

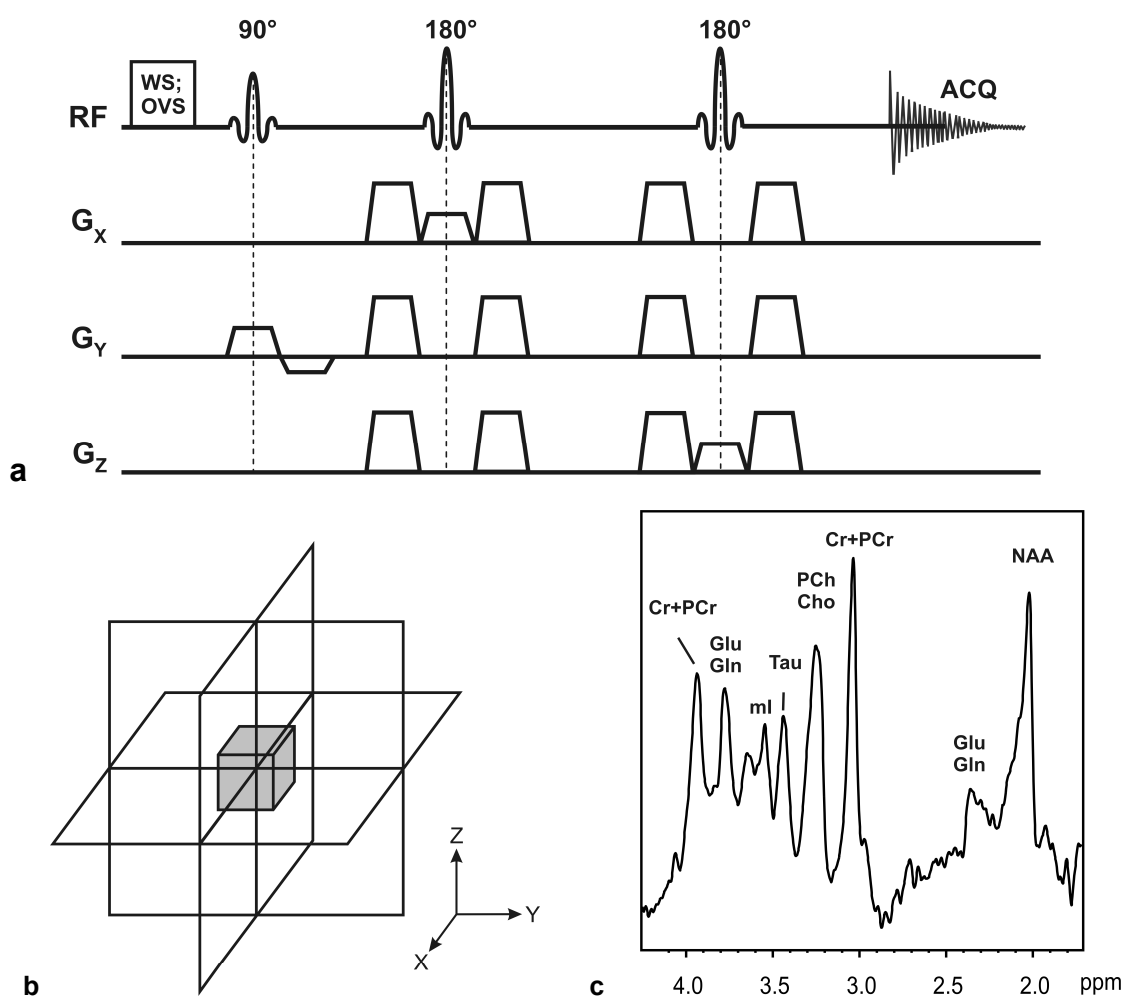


Figure 2.5: a) PRESS sequence: The slice selective pulses along orthogonal axes define three orthogonal slices, with the volume of interest (voxel) located at the intersection of the slices (b). The crusher gradients on either side of the  $180^\circ$  pulses dephase unwanted magnetization. The entire sequence is preceded by a water-suppression and outer volume suppression schemes. These remove the water signal and signals outside of the voxel from the final spectrum. c) An example of an MR spectrum obtained from a localized region in the brain of a mouse.

Outer volume suppression schemes excite narrow slices positioned around the volume of interest to selectively remove unwanted signals from outside the voxel. Following slice selective excitation, the transverse magnetization in these slices is dephased by a subsequent magnetic field crusher gradient. OVS is most commonly employed to remove lipid signals from the spectrum (3). As water is the most abundant compound in tissue, the NMR proton spectrum of almost all tissue is dominated by a resonance at  $\sim 4.7$  ppm that originates from water protons. While metabolite detection is possible without water suppression, the water peak does lead to baseline distortions and spurious signals due to vibration-induced signal modulation, which make the detection of metabolites unreliable (3). Suppression of the water signal eliminates these problems, leading to a reliable and consistent detection of metabolite spectra. Water signals can be eliminated by utilizing differences in relaxation parameters. One such method, VAPOR, combines  $T_1$ -based water suppression and optimized frequency-selective perturbations to provide excellent water suppression with a large insensitivity towards  $T_1$  and  $B_1$  inhomogeneity (3,9). The combination of OVS and water suppression improves localization performance and reduces the demand for spoiler gradients (9).

When implementing MRS, in particular at ultra-high fields ( $\geq 7$  Tesla), several important factors should be considered when preparing an experiment. The first is field inhomogeneity. A sample brought into the main magnetic field of the scanner distorts the magnetic field. Properly shimming the field prior to the experiment ensures that the magnetic field homogeneity is at its optimum. The need for a proper shim is that the resonance frequency of the sample depends on the magnetic field strength. Hence, spins “experiencing” the same field will resonate at the same frequency and thus produce a resonance with a narrow line, with a low FWHH. A poor shim will result in spins resonating at a range of frequencies rather than one single frequency, which in turn results in broad peaks and high FWHH. An additional benefit of narrow resonances is that the signal will be stronger, as the FWHH is inversely related to  $T_2$  (10,11). The second important factor is short echo times. This criterion is closely related to the previous one, since  $T_2$  relaxation rates increase with increasing field strength, yielding a shorter  $T_2$ . The choice of the shortest possible echo time ensures the least signal loss due to dephasing (10,11). Finally, the RF pulse bandwidth and gradient strength are important. Short, high bandwidth pulses, coupled with strong gradients are preferable, as these reduce the likelihood of chemical shift displacement artifacts (3,10,11).

### 2.3 Two-dimensional Magnetic Resonance Spectroscopy

The general idea of 2D experiments is to generate a second frequency axis by introducing an evolution delay into a pulse sequence, during which the transverse magnetization precesses at a different frequency than during signal acquisition (12,13). Generally, 2D MRS experiments consist of four stages: preparation, evolution, mixing and detection. Starting from a spin system in thermodynamic equilibrium, during the preparation period this spin system has to be prepared in a coherent non-equilibrium superposition of quantum states. One of the simplest 2D experiments is the correlation spectroscopy sequence (12,13). Here the preparation period consists of a single pulse. The spin system evolves during the evolution period  $t_1$ . To sample the changes during  $t_1$ , a series of experiments is carried out with a systematic increment of  $t_1$ . This provides the information in the frequency domain  $F_1$  (13), (Chap. 6). During the mixing time a pulse is applied that transforms coherences into observable transverse magnetization. The observable magnetization is recorded during the detection time, commonly designated  $t_2$ , and corresponds to the other frequency domain in the 2D experiment. The experimental dataset collected therefore corresponds to a time domain matrix that comprises the time-dependent signals in the two time dimensions  $t_1$  and  $t_2$ , and a double Fourier transform converts this into a matrix with two frequencies axes,  $F_1$  and  $F_2$ . The result is a three-dimensional landscape representing the variation of the signal intensity over the plane spanned by the two frequency dimensions  $F_1$  and  $F_2$ , and is commonly presented as a contour plot (14).

For the COSY experiment, incrementing the evolution period reveals the frequencies  $\omega_1$  during  $t_1$  according to  $\omega_1 = d\varphi/dt_1$ , where  $\varphi$  is the phase of the coherences at  $t_2 = 0$ . For uncoupled spins the resonance frequency is identical during the evolution and detection period (i.e.  $\omega_1 = \omega_2$ ), giving rise to diagonal peaks in the 2D MR spectrum. For  $J$ -coupled spin systems, additional off-diagonal or cross-peaks will arise at  $(\omega_1, \omega_2)$  and  $(\omega_2, \omega_1)$  where  $\omega_1 \neq \omega_2$ . This gives direct information on the connectivity pattern within a spin system via the  $J$ -couplings, and NMR signals can be assigned even when the spins are not resolved in the 1D spectrum (3), (Chap. 8).

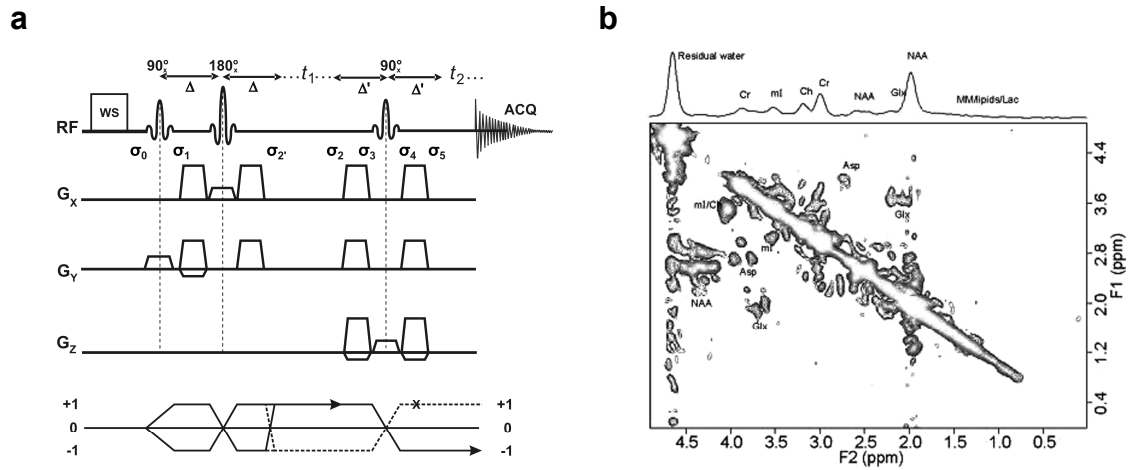


Figure 2.6: a) Localized two-dimensional shift correlated MR spectroscopic sequence. The RF pulse scheme consists of three RF pulses ( $90^\circ$ ,  $180^\circ$ ,  $90^\circ$ ), which are slice-selective along three orthogonal axes. A pair of  $B_0$  gradient crusher pulses is symmetric with respect to the slice-refocusing  $180^\circ$  RF pulse. The last slice-selective  $90^\circ$  RF pulse with a pair of symmetric  $B_0$  gradient crushers also serves as a coherence transfer pulse for the L-COSY spectrum. The sequence is preceded by a water suppression scheme. The coherence transfer pathway diagram depicts the different stages of conversion of magnetization/coherences (13). The  $t_1$  evolution for the 2D spectroscopy,  $\sigma_2$ - $\sigma_2$ , is integrated with volume localization and follows the evolution during the slice selection  $\sigma_1$ - $\sigma_2$  that refocuses the chemical shift prior to the 2D evolution. b) Sample 2D L-COSY spectrum obtained from a 27 ml voxel localized in the occipito-parietal gray matter region of a healthy human volunteer. Reproduced, with permission, from Thomas et al. 2003 (15). © John Wiley & Sons, Inc.

### Localized 2D shift-correlated MR spectroscopy (L-COSY)

In localized 2D MRS the preparation, evolution, mixing and detection are integrated with volume selection. The L-COSY sequence achieves this through the integration of an evolution period in a spatially selective PRESS sequence that comprises three slice selective RF pulses ( $90^\circ$ ,  $180^\circ$ ,  $90^\circ$ ) combined with three orthogonal  $B_0$  gradients. The L-COSY sequence is derived from the COSY experiment and was first developed and published by Thomas and colleagues in 2001 (16). The pulse sequence with a representative 2D spectrum obtained from a localized region in the brain of a human subject is depicted in figure 2.6. The advantage of the L-COSY sequence is that the volume localization and the coherence transfer via the  $J$ -couplings are achieved simultaneously, without adding additional RF or gradient pulses. For high magnetic fields, the frequency differences between signals from different nuclear spins is often much larger than the scalar coupling constant  $J$ , and the spins are weakly coupled. In that case a straightforward description of the L-COSY experiment (Fig 2.6a) can be given using the product operator formalism instead of a full density matrix treatment. The calculation of the amplitudes and phases of L-COSY diagonal and cross peaks in a



weakly coupled two spin system, with  $I$  the spin under consideration and  $S$  its  $J$ -coupled partner ( $I, S = \text{spin } \frac{1}{2}$ ), is summarized below (3,13,16). The coherences  $\sigma_0$ - $\sigma_5$  describing the conversion of magnetization are depicted in Fig. 2.6a.

Prior to the first slice-selective  $90^\circ$  RF pulse, the preparation stage, the spin-state is represented by

$$\sigma_0 \propto I_z. \quad (2.11)$$

After the rotation by the first  $90^\circ$  RF pulse, the spin-state is represented by

$$\sigma_1 \propto I_y. \quad (2.12)$$

After the first evolution during the interval of  $2\Delta$ , the spins evolve under the influence of the gradients and  $J$ -coupling, but the chemical shift will be refocused by the slice selective  $180^\circ$  pulse resulting in an echo characterized by

$$\sigma_2 \propto I_y \cos(2\pi J_{IS}\Delta) - 2I_x S_z \sin(2\pi J_{IS}\Delta). \quad (2.13)$$

Starting from  $\sigma_2$ ,  $t_1$  evolution allows for the encoding of chemical shift ( $\omega_1^{(I)}$ ) for 2D spectroscopy, while in parallel the  $J$ -coupling sustains the development of the  $I_x S_z$  coherence for the detection of 2D correlations, yielding

$$\begin{aligned} \sigma_2 \propto & [I_y \cos(\omega_1^{(I)} t_1) \cos(\pi J_{IS} t_1) - 2I_x S_z \cos(\omega_1^{(I)} t_1) \sin(\pi J_{IS} t_1) \\ & - I_x \sin(\omega_1^{(I)} t_1) \cos(\pi J_{IS} t_1) - 2I_y S_z \sin(\omega_1^{(I)} t_1) \sin(\pi J_{IS} t_1)] \\ & \times \cos(2\pi J_{IS}\Delta) - [2I_x S_z \cos(\omega_1^{(I)} t_1) \cos(\pi J_{IS} t_1) \\ & + I_y \cos(\omega_1^{(I)} t_1) \sin(\pi J_{IS} t_1) + 2I_y S_z \sin(\omega_1^{(I)} t_1) \cos(\pi J_{IS} t_1) \\ & - I_x \sin(\omega_1^{(I)} t_1) \sin(\pi J_{IS} t_1)] \sin(2\pi J_{IS}\Delta). \end{aligned} \quad (2.14)$$

Using

$$A = \cos(\omega_1^{(I)} t_1) \cos(\pi J_{IS} t_1), \quad (2.14a)$$

$$B = \cos(\omega_1^{(I)} t_1) \sin(\pi J_{IS} t_1), \quad (2.14b)$$

$$C = \sin(\omega_1^{(I)} t_1) \cos(\pi J_{IS} t_1), \quad (2.14c)$$

$$D = \sin(\omega_1^{(I)} t_1) \sin(\pi J_{IS} t_1), \quad (2.14d)$$

eq. (2.4) simplifies to:

$$\sigma_2 \propto [AI_y - B2I_x S_z - CI_x - D2I_y] \cos(2\pi J_{IS}\Delta) - [A2I_x S_z + BI_y + C2I_y S_z - DI_x] \sin(2\pi J_{IS}\Delta). \quad (2.15)$$

A second pair of  $B_0$  gradient crusher pulses is transmitted around the last slice-selective  $90^\circ$  RF pulse. After an evolution during the first set of crusher gradient pulses ( $\theta_1$ ), the spin state is represented by

$$\begin{aligned} \sigma_3 \propto \{ & AI_y \cos \theta_1 - AI_x \sin \theta_1 - CI_x \cos \theta_1 - CI_y \sin \theta_1 \\ & - B2I_x S_z \cos \theta_1 - B2I_y S_z \sin \theta_1 - D2I_x S_z \cos \theta_1 \\ & + D2I_x S_z \sin \theta_1 \} \cos(2\pi J_{IS}\Delta) - \{ BI_y \cos \theta_1 - BI_x \sin \theta_1 \\ & - DI_x \cos \theta_1 - DI_y \sin \theta_1 + A2I_x S_z \cos \theta_1 + A2I_y S_z \sin \theta_1 \\ & + C2I_y \cos \theta_1 - C2I_x S_z \sin \theta_1 \} \sin(2\pi J_{IS}\Delta). \end{aligned} \quad (2.16)$$

The spin state after the last  $90^\circ$  RF pulse rotation, or mixing stage, is

$$\begin{aligned} \sigma_4 \propto \{ & AI_z \cos \theta_1 - AI_x \sin \theta_1 - CI_x \cos \theta_1 - CI_z \sin \theta_1 \\ & + B2I_x S_y \cos \theta_1 + B2I_z S_y \sin \theta_1 + D2I_z S_y \cos \theta_1 \\ & - D2I_x S_y \sin \theta_1 \} \cos(2\pi J_{IS}\Delta) - \{ BI_z \cos \theta_1 - BI_x \sin \theta_1 \\ & - DI_x \cos \theta_1 - DI_z \sin \theta_1 - A2I_x S_y \cos \theta_1 - A2I_z S_y \sin \theta_1 \\ & - C2I_z \cos \theta_1 + C2I_x S_y \sin \theta_1 \} \sin(2\pi J_{IS}\Delta). \end{aligned} \quad (2.17)$$

At this point, evolution of  $I_z$  and  $2I_x S_y$  will be excluded since there will be no observable signal. The spin state after an evolution during the last set of  $B_0$  gradient crushers ( $\theta_2$ ):

$$\begin{aligned} \sigma_5 \propto & \frac{1}{2} \cos(2\pi J_{IS}\Delta) [I_y \cos(\omega_1^{(I)} t_1) \cos(\pi J_{IS} t_1) \\ & + I_x \sin(\omega_1^{(I)} t_1) \cos(\pi J_{IS} t_1) + 2I_z S_x \cos(\omega_1^{(I)} t_1) \sin(\pi J_{IS} t_1) \\ & - 2I_z S_y \sin(\omega_1^{(I)} t_1) \sin(\pi J_{IS} t_1)] + \frac{1}{2} \sin(2\pi J_{IS}\Delta) [I_y \cos(\omega_1^{(I)} t_1) \sin(\pi J_{IS} t_1) \\ & + I_x \sin(\omega_1^{(I)} t_1) \sin(\pi J_{IS} t_1) - 2I_z S_x \cos(\omega_1^{(I)} t_1) \cos(\pi J_{IS} t_1) \\ & + 2I_z S_y \sin(\omega_1^{(I)} t_1) \cos(\pi J_{IS} t_1)]. \end{aligned} \quad (2.18)$$

Equation (2.8) shows the 2D encoding for the I-spin that was achieved during the  $t_1$  period. It was calculated under the assumption that the gradient crushers are balanced ( $\theta_1 = \theta_2$ ) and also using

$$\frac{1}{2\pi} \int_0^{2\pi} \cos \theta \sin \theta d\theta = 0 \quad \text{and} \quad \frac{1}{2\pi} \int_0^{2\pi} \sin^2 \theta d\theta = \frac{1}{2}. \quad (2.19)$$

The phase factors,  $\theta_1$  and  $\theta_2$ , are defined as:

$$\theta_1 = 2\pi\gamma \int \Delta B_0 dt_1 \quad \text{and} \quad \theta_2 = 2\pi\gamma \int \Delta B_0 dt_2. \quad (2.20)$$

Here  $\tau_1$  and  $\tau_1$  are the durations of the second pair of gradient crusher pulses. It is also evident from Equation (2.8) that the coherence transfer from spin  $I$  to spin  $S$  is characterized by  $2I_z S_x$  and  $2I_z S_y$ . A similar equation can also be calculated for spin  $S$  resulting in a coherence transfer to spin  $I$ . Finally, the 2D signal acquired after the last crusher gradients, during the detection time  $t_2$ , is given by

$$s(t_1, t_2) = \text{Tr} \{ (I_x) \sigma_S \} e^{-i\omega_2^{(I)} t_2} e^{-t_1/T_2} \times e^{-t_2/T_2} [1 - e^{-TR/T_1}]. \quad (2.21)$$

A double Fourier transformation along both  $t_1$  and  $t_2$  axes will result in a 2D MR spectrum as a function of two frequency variables ( $F_1, F_2$ ) described by:

$$S(F_1, F_2) = \iint s(t_1, t_2) dt_1 dt_2. \quad (2.22)$$

Aue *et al.* (17) reported that the diagonal peaks were dispersive, whereas the cross-peaks were absorptive when two hard  $90^\circ$  RF pulses were used to acquire the COSY spectrum. In contrast to the amplitude modulation in conventional COSY, phase modulation is present in the L-COSY, which is caused by the evolution during the  $B_0$  gradient pulse before the last  $90^\circ$  RF pulse (18). Equation (2.8) clearly indicates that both the diagonal and cross-peaks of an L-COSY spectrum have mixed phases along the  $F_1$  axis. Hence a drawback of including the gradient pulses is mixed line shapes in the 2D NMR spectra (18).

In this thesis the 2D L-COSY sequence has been applied for the first time in mouse brain, demonstrating its potential for simultaneously resolving and assigning several metabolite resonances *in vivo* (chapter 4) and examining the age-dependent neurochemical changes occurring in AD transgenic mice (Tg2576) as a result of disease progression (chapter 5).

## References

1. Levitt MH. Spin Dynamics: Basics of Nuclear Magnetic Resonance, 1st ed. Wiley 2001, Chichester, UK.
2. Haacke EM, Brown RW, Thompson MR, Venkatesan R. Magnetic Resonance Imaging: Physical Principles and Sequence Design, 1st ed. Wiley-Liss 1999, Hoboken, USA.
3. De Graaf RA. In vivo NMR spectroscopy: Principles and techniques, 2nd ed. Wiley 2008, Chichester, UK.

4. Brown MA, Semelka RC. MRI: Basic Principles and Applications, 3rd ed. Wiley-Liss 2003, Hoboken, USA.
5. Hennig J, Nauerth A, Friedburg H. Rare Imaging - A Fast Imaging Method For Clinical Mr. *Magn Reson Med* 1986;3:823-833.
6. De Graaf RA. *In vivo NMR spectroscopy: Principles and techniques*, 1st ed. Wiley 1998, Chichester, UK.
7. Bottomley PA; Selective volume method for performing localized NMR spectroscopy, 1984; US patent 4,480,228
8. Bottomley PA. Spatial Localization In NMR Spectroscopy *In vivo*. *Ann N Y Acad Sci* 1987;508:333-348.
9. Tkac I, Starcuk Z, Choi IY, Gruetter R. *In vivo* H-1 NMR spectroscopy of rat brain at 1 ms echo time. *Magn Reson Med* 1999;41:649-656.
10. Tkac I. Lecture notes: The Ingredients of a Successful MRS Study at Ultra-High-Field. ISMRM 16th annual meeting 2008. Toronto, Canada.
11. Tkac I, Gruetter R. Methodology of H-1 NMR spectroscopy of the human brain at very high magnetic fields. *Applied Magnetic Resonance* 2005;29:139-157.
12. Jeener J. unpublished lecture notes. Ampere Summer School 1971. Basko Polje, Yugoslavia.
13. Ernst RR, Bodenhausen G, Wokaun A. *Principles of nuclear magnetic resonance in one and two dimensions*. Oxford Publications 1987, Oxford, UK.
14. Martin GE, Zektzer AS. *Two-dimensional NMR methods for establishing molecular connectivity*. VCH Verlagsgesellschaft 1988, Weinheim, Germany.
15. Thomas MA, Hattori N, Umeda M, Sawada T, Naruse S. Evaluation of two-dimensional L-COSY and PRESS using a 3 T MRI scanner: from phantoms to human brain *in vivo*. *NMR Biomed* 2003;16:245-251.
16. Thomas MA, Yue K, Binesh N, Davanzo P, Kumar A, Siegel B, Frye M, Curran J, Lufkin R, Martin P, Guze B. Localized two-dimensional shift correlated MR spectroscopy of human brain. *Magn Reson Med* 2001;46:58-67.
17. Aue WP, Bartholdi E, Ernst RR. 2-Dimensional Spectroscopy - Application To Nuclear Magnetic-Resonance. *J Chem Phys* 1976;64:2229-2246.
18. Brereton IM, Galloway GJ, Rose SE, Doddrell DM. Localized 2-Dimensional Shift Correlated Spectroscopy In Humans At 2-Tesla. *Magn Reson Med* 1994;32:251-257.



# 3 Longitudinal assessment of Alzheimer's $\beta$ -amyloid plaque development in transgenic mice monitored by *in vivo* magnetic resonance microimaging\*

---

## 3.1 Abstract

The development of  $\beta$ -amyloid plaques with age in the brains of the transgenic mouse model of Alzheimer's disease pathology was assessed by *in vivo* magnetic resonance microimaging. Towards this goal live transgenic mice (Tg2576) and non-transgenic littermates (control) were studied at regular intervals between the age of 12 and 18 months. Plaques were visualized using a  $T_2$  weighted Rapid Acquisition with Relaxation Enhancement sequence. Changes in  $T_2$  relaxation times were followed using a Multi-Slice Multi-Echo sequence. SCIL image software was used to calculate the plaque-load in the  $T_2$  weighted MR images. A $\beta$  plaques were clearly detected with the  $T_2$  weighted RARE sequence in a scan time as short as 25 min in the hippocampal and cortical regions of the brain of Tg2576 mice but not in control mice. Following the plaque development in the same animals with age shows that the plaque-load and plaque size increased markedly, while  $T_2$  relaxation times show a decreasing trend with age. These results demonstrate that  $\mu$ MRI is a viable method for following the plaque developmental characteristics *in vivo* in the same animals and suggest that monitoring the effect of future therapeutic interventions over time in the same animals would ultimately be possible by  $\mu$ MRI.

## 3.2 Introduction

Alzheimer's disease is the most common neurodegenerative disease and currently afflicts about 10% of the population over 60, with numbers still rising (1). The neuropathologic features of AD include the occurrence of senile plaques, neurofibrillary tangles, decreased synaptic density, and loss of neurons. The core of senile plaques consists mainly of aggregated amyloidogenic peptide A $\beta$  which is derived from the amyloid precursor protein. The role of A $\beta$  in AD may be substantial, as soluble A $\beta$  polymers have

---

\*This chapter was published in J Magn Reson Imaging 2006; 24:530 - 536

been reported to be neurotoxic, both *in vitro* and *in vivo* (2). Although it is not yet clear whether senile plaques themselves are neurotoxic, A $\beta$  plaque formation precedes disease onset by many years and is generally accepted as a biomarker for onset and progression of the disease (2,3). Early diagnosis of Alzheimer's disease is prevented by difficulties in visualizing A $\beta$  plaques *in vivo* in the brain, and the only definite diagnosis for AD at present is post-mortem observation of A $\beta$  plaques and neurofibrillary tangles in brain sections (4).

In order to study the pathogenesis of AD, its development over time, and to ultimately develop adequate therapeutic agents or preventive strategies, it is important to establish non-invasive *in vivo* imaging methods to visualize A $\beta$  plaques and to validate if the  $\mu$ MRI is feasible for quantitative monitoring of the plaque development with age in the same animals. Imaging methods such as single photon emission computed tomography or positron emission tomography use ionizing radiation and suffer from low resolution (5). MRI can provide much higher resolution than SPECT or PET without ionizing radiation and can theoretically resolve individual plaques non-invasively. The first effort to visualize A $\beta$  plaques by MRI in fixed post-mortem human brain tissue was made by Benveniste *et al.* (6) using  $T_2^*$ -weighted MRI at 7T. Subsequently several different transgenic mouse models of AD pathology have been used to visualize A $\beta$  plaques either *ex vivo* in fixed brain (5,7,8) or *in vivo* using targeted contrast agents (9,10) or amyloidophilic probes (2,11). However, the delivery of these agents requires a relatively invasive procedure. Very recently, initial efforts for *in vivo* detection of A $\beta$  plaques using MRI without the aid of an exogenous plaque-specific contrast agent have also been reported in transgenic mouse models of AD (12,13) using  $T_2$ -weighted spin echo and  $T_2^*$ -weighted gradient echo sequences. Vanhoutte *et al.* (13) used basic  $T_2^*$ -weighted MRI to visualize plaques associated with iron *in vivo* in the thalamus region of the brain, but failed to detect plaques in the cortex and hippocampus areas which are the main regions of A $\beta$  deposit in the brain in human as well as in transgenic mouse models of AD pathology (14,15). Although imaging of A $\beta$  plaques *in vivo* without the aid of an exogenous plaque-specific contrast agent still lacks sufficient sensitivity and requires further improvement, to date no longitudinal MR studies to follow the development of A $\beta$  plaques with age in the same animals have been attempted. In recent longitudinal studies concerning the detection of A $\beta$  plaque-load in mouse models of AD pathology, post-mortem biochemical and/or histological examinations were performed on different mice belonging to different age groups (16).

In the present study, high field  $\mu$ MRI was used to detect A $\beta$  plaques in a living transgenic mouse model of AD pathology, without contrast agent, and to track the development of plaques with age in the same animals. Our results demonstrate that  $\mu$ MRI is a viable non-invasive method for longitudinal studies to assess A $\beta$  plaque development in a quantitative manner and thus would be invaluable for evaluation of new anti-amyloid treatment strategies.

### 3.3 Methods

#### 3.3.1 Transgenic mice

The transgenic mice used in this study contain as transgene the Swedish double mutation of the human amyloid precursor protein (APP<sub>695</sub>), as developed and described previously by Hsiao et al (17). The transgene is expressed in C57B6 breeders. The N2 generation mice of both genders (n=5) were studied at ages between 12 and 18 months. Age-matched non-transgenic littermates served as controls. All animal experiments were approved by the Institutional Animal Care and Animal Use Committee in accordance with the NIH *Guide for the care and Use of Laboratory Animals*.

#### 3.3.2 $\mu$ MRI

All  $\mu$ MRI measurements were conducted on a vertical wide-bore 9.4T Bruker Avance 400WB spectrometer, with a 1000 mTm<sup>-1</sup> actively shielded imaging gradient insert (Bruker). The imaging coil used was a 25 mm volume coil (Bruker) which was best suited to acquire full brain images in both the coronal and the horizontal plane. The system was interfaced to a Linux pc running XWinNMR 3.2 and Paravision 3.02pl (Bruker Biospin).

For *in vivo*  $\mu$ MRI measurements the mice were anesthetized using Isoflurane (Forene, Abott, UK) inhalation anesthesia, together with air and oxygen (1:1) at 0.3 l/minute. The anesthetic gas was administered via a special face mask, which also served as a fixation device for the mouse head by coupling it with a specially designed toothbar to hold the head in place (Bruker Biospin). While inside the probe, the respiration rate of the mouse was constantly monitored by means of a pressure transducer placed on the abdomen. The transducer was connected to a BioTrig acquisition module, which was interfaced to a BioTrig command module and laptop running BioTrig BT1 monitoring software (Bruker Biospin).



$T_2$ -weighted MR images were acquired using a RARE sequence (18) which employs a single excitation step followed by the collection of multiple phase-encoded echoes. This reduces the total scan time significantly compared to normal multi slice spin echo methods. Basic measurement parameters used for the RARE sequence were: TE = 10.567 ms (22.45 ms effective), TR = 5-6 s, flip angle =  $90^\circ$ , averages = 4+, RARE factor (echo train length) = 4. The field of view was  $2.0 \times 2.0 \text{ cm}^2$ , with an image matrix of  $256 \times 256$ . This yields an effective in plane resolution of approximately  $78 \mu\text{m}$ . Coronal (transverse) image slices (30-60) were acquired from the olfactory bulb to the cerebellum with a slice thickness of 0.2 mm spaced 0.2 mm between slices, or 0.5 mm spaced 0.5 mm between slices. The horizontal and coronal slices shown in Fig. 3.1 and those used for longitudinal studies (Fig. 3.4) were obtained with a slice thickness of 0.5 mm and a total scan time of approximately 25 minutes.

For  $T_2$  relaxation measurements, an MSME sequence was used. Imaging parameters were: FOV  $2.0 \times 2.0 \text{ cm}^2$ , matrix size  $256 \times 256$ , number of averages 2, number of slices 6 with slice thickness of 1 mm, number of echoes = 8 with TE of 8.5, 17.0, 25.5, 34.0, 42.5, 51.0, 59.5, and 68.0 msec, and a repetition time of 1.5 seconds. To calculate the  $T_2$  relaxation time, regions of interest were drawn around the cortex and hippocampus in two adjacent mid-coronal slices. Another ROI in the muscle was used as an internal control according to Helpert *et al.* (7). The means and standard deviation of the  $T_2$  relaxation times for each ROI were calculated. Mean values were compared using Student's t-test assuming equal variance, and significance was assigned at  $P < 0.05$ .

### 3.3.3 Brain preparation and histology

Following *in vivo* MR measurements, mice were deeply anesthetized and transcardially perfused with phosphate-buffered saline (pH 7.4) followed by 4% buffered paraformaldehyde (Zinc Formal-Fixx, ThermoShandon, UK) through the left cardiac ventricle. After perfusion fixation the brain was dissected out and placed in the same fixative for 48 h. Following fixation, the brain was dehydrated and embedded in paraffin. Subsequently coronal sections ( $40 \mu\text{m}$  thick) were carefully cut using a vibratome while maintaining as much as possible the same spatial orientation of mouse brain as in the MR imaging experiments. To detect the  $A\beta$  plaques, brain sections were subjected to immunohistochemistry using monoclonal anti-amyloid  $\beta$  (6E10) antibody at 1:1000 (Signet Laboratories, Inc). Immunolabeling was visualized by using the ABC kit (Vectastain) according to the manufacturer's instructions.

Detection of redox active iron associated with the A $\beta$  plaques was done histochemically as described previously (19,20). Briefly, the brain sections were incubated for 15 h in 7% potassium ferrocyanide in aqueous hydrochloric acid (3%) and subsequently incubated in 0.75 mg/ml 3, 3'-diaminobenzidine (DAB) and 0.015% H<sub>2</sub>O<sub>2</sub> for 5-10 min. This method involves the formation of mixed-valence iron (II/III), (Prussian blue) when iron (III) released from iron containing plaques by the hydrochloric acid reacts with potassium ferrocyanide. The mixed-valence complex then catalyzes the H<sub>2</sub>O<sub>2</sub>-dependent oxidation of DAB to give a brown color. Images of the histological sections were obtained using a Leica DM RE HC microscope, interfaced to a Leica DC500 3CCD digital camera. Quantitative histological analysis of A $\beta$  plaque density and iron associated plaques was performed by SCIL image software (21).

For co-registration, immuno-histological images were matched with MR slices using common anatomical landmarks such as the ventricles, corpus callosum and hippocampal fissure using PhotoShop 7.0 (Adobe Systems, San Jose, CA). As a result of differences in the slice thickness in  $\mu$ MRI (200 $\mu$ m) and histology (40  $\mu$ m), each MR image could be matched with at least 4 immuno-stained histological images.

### 3.3.4 Image analysis and quantification

For quantification of A $\beta$  plaque-load and numerical density in MR images, image files with calibrated scale markers were imported in SCIL image software (21). The brightness of the images was altered so that the average optical density measurement for each imported image was similar. Regions of interest were manually drawn on the cortex and hippocampus, corresponding to the same anatomical markers used for histological A $\beta$  quantification. Dark spots, with intensity below a preset threshold value (equal for all MR images), were considered as A $\beta$  plaques. A $\beta$  plaque-load (percentage hypointense area of the ROI) and numerical density of plaques (number of plaques per mm<sup>2</sup> of the ROI) were calculated for cortex and hippocampus.

## 3.4 Results

Figure 3.1 shows horizontal (axial) and transverse (coronal) slices through the brain of a living 18-month-old APP transgenic mouse (Tg2576) and its non-transgenic littermate (control) obtained by using a  $T_2$ -weighted RARE sequence. As can be seen in this figure, numerous dark spots were clearly evident in the cortex and hippocampus areas in both horizontal and transverse MR slices of the brain of Tg2576 transgenic mouse (Fig. 3.1, right panels).

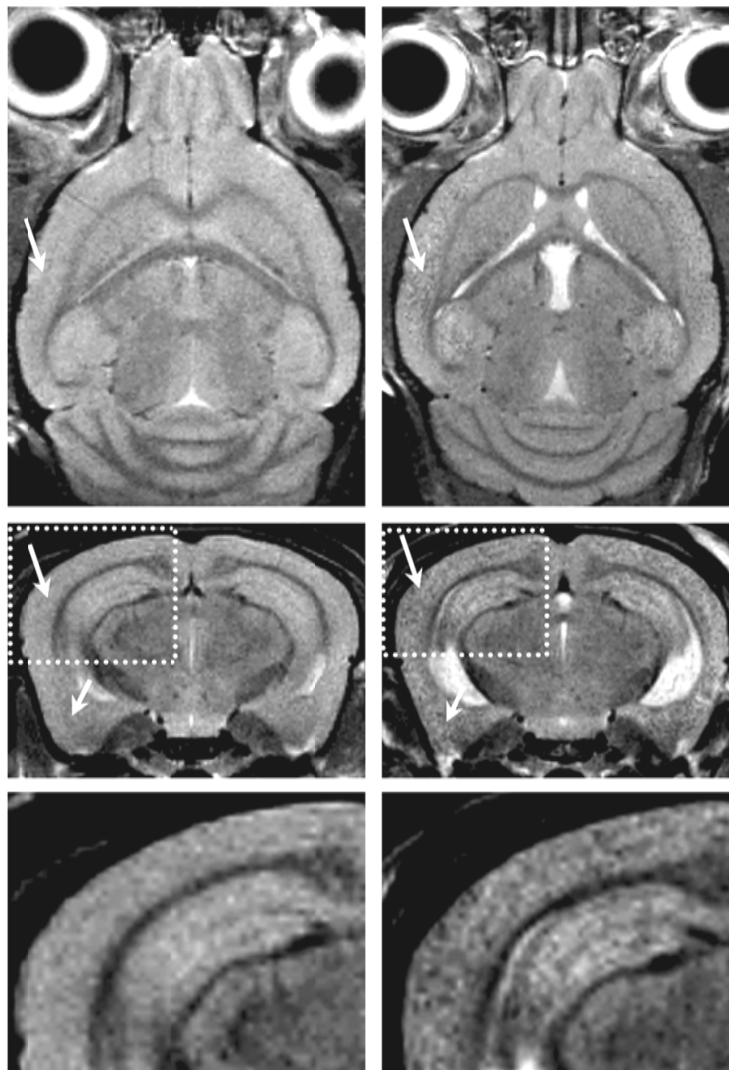


*Figure 3.1: In vivo  $T_2$ -weighted MR images of the brain of an 18-month-old control mouse (left panels) and AD transgenic Tg2576 mouse (right panels) obtained at 9.4T. The top row shows horizontal slices (Bregma: -6 mm), the middle row shows coronal slices (Bregma: -3.4 mm) and the bottom row shows magnified sub-sampled insets of the coronal slices, showing adequately resolved individual plaques in the bottom right panel. MR images were obtained with an in-plane resolution of  $78 \mu\text{m} \times 78 \mu\text{m}$  ( $TE = 10.567 \text{ ms}$ ,  $TR = 6\text{s}$ , echo train length = 4, averages = 4, total scan time 25 min). Arrows indicate areas with differences in the signal intensities between the Tg2576 mouse and its non-transgenic litter-mate. Numerous circular hypointensities can be clearly observed in the images of the cortical and hippocampal areas of the Tg2576 mouse right column), while no clear signal hypointensities are visible in the images collected from the control mouse shown in the left column.*

These hypointense regions could be detected with scan times as short as 25 minutes. Such signal hypointensities were not observed in the brains of control mice (Fig. 3.1, left panels). MR hypointensities can be seen more clearly with higher magnification as displayed in the bottom row in Fig. 3.1.

To confirm that the hypointense signals seen in MR images correspond to the A $\beta$  plaques, *in vivo* MR images of an 18-month-old transgenic mouse were compared with immunostained images obtained from the same mouse brain (Fig. 3.2). Immunolabeled sections show that dense-cored plaques are the predominant form of senile plaques in the cortical and hippocampal areas of the Tg2576 transgenic mouse brain (Fig. 3.2b). Many are giant plaques with core diameters above 100  $\mu$ m. In addition a few diffuse plaques were also observed. Co-registration of plaques between *in vivo*  $\mu$ MRI and corresponding immunostained sections validates that many circular hypointense regions seen in  $\mu$ MRI correspond to A $\beta$  plaques (Fig. 3.2).

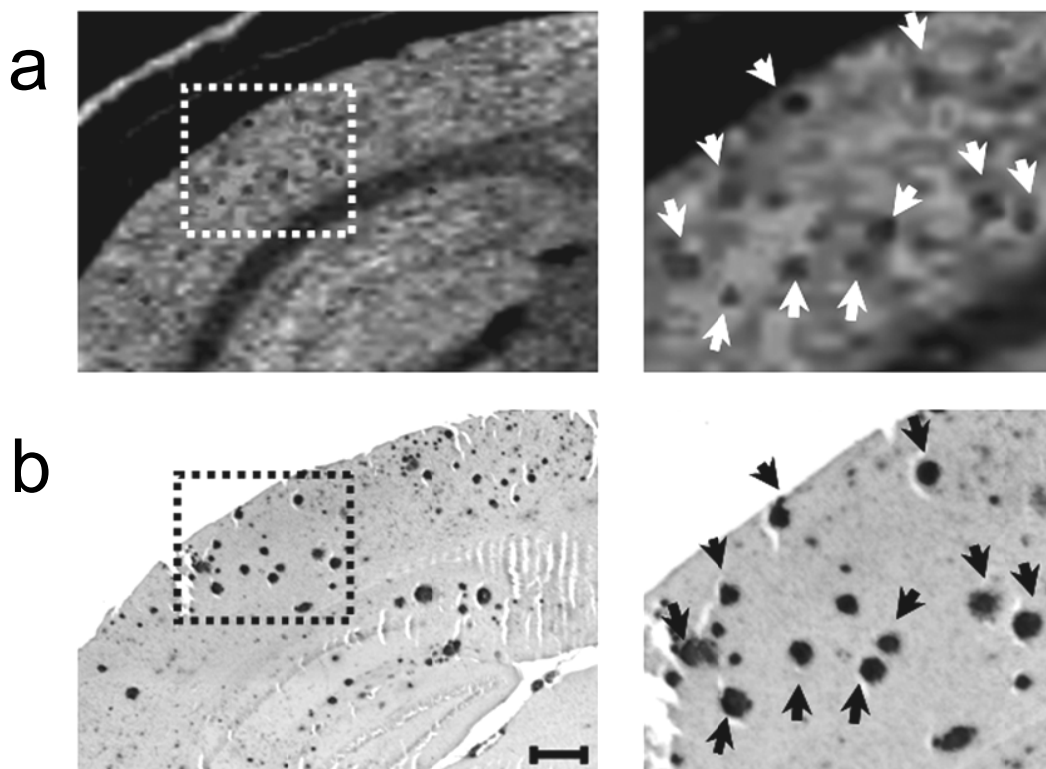


Figure 3.2: Co-registration of A $\beta$  plaques seen in the brain of an 18-month-old AD mouse by (a) *in vivo*  $\mu$ MRI and (b) histological section of the same mouse brain stained with A $\beta$  antibodies. Many MR circular hypointense spots could be matched to immunostained A $\beta$  plaques (arrows), seen more clearly in the higher magnification insets. Scale bar, 500  $\mu$ m.

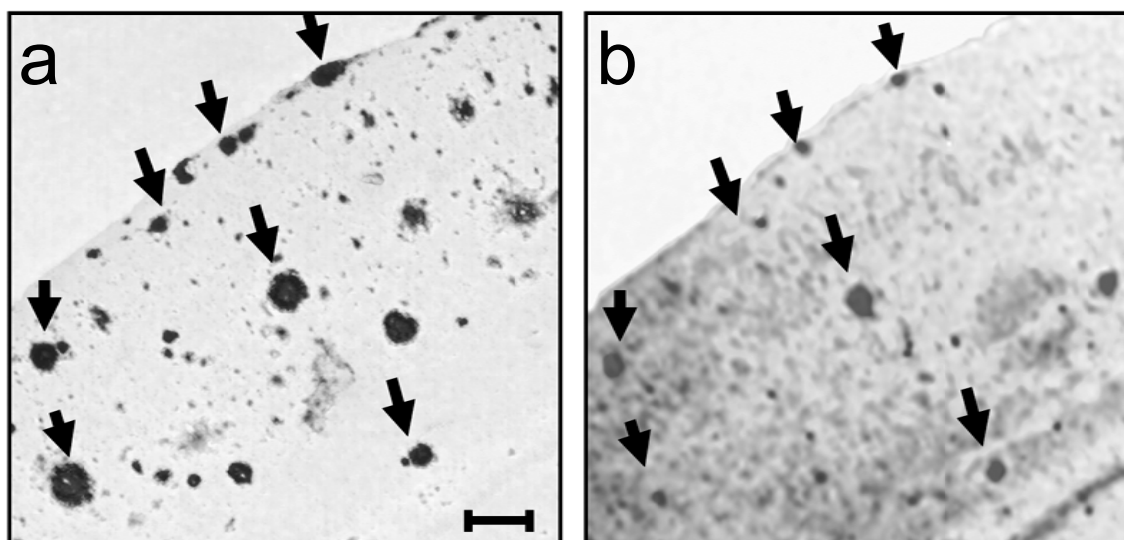


Figure 3.3: Co-registration of A $\beta$  plaques and iron in the adjacent brain sections of an 18-month-old Tg2576 mouse. Brain sections (4  $\mu$ m thick) were stained with (a) an A $\beta$  antibody (6E10) or (b) Perl's reaction following 3, 3-diaminobenzidine enhancement. Arrows indicate co-registered plaques. Scale bar, 250  $\mu$ m.

Although association of iron with plaques in human and in mouse models of AD pathology is known (19,22,23,24), it is yet to be established if it is the main reason for plaque specific  $T_2$  contrast in MR images. As can be seen in Fig. 3.3, iron (III) was found to be associated with many dense-cored senile plaques, although not all A $\beta$  plaques seen by immunohistology contained iron. Iron loaded plaques were restricted to the cortical and hippocampal regions of the brain (Fig. 3.3).

To examine the utility of  $\mu$ MRI for detecting the development of A $\beta$  plaques in longitudinal studies, the same mice ( $n=5$  for each group) were imaged at regular intervals of approximately one month starting at the age of 12 months. An example of MR images obtained from the brain of a Tg2576 transgenic mouse at the age of 12, 14, 16 and 18 months is displayed in Fig. 3.4. A consistent increase in the MR hypointensities was observed with age in the cerebral cortical and hippocampal regions. In addition to the overall rise in MR hypointensities, the size of the circular hypointense spots also increased, suggesting an increase in the size of A $\beta$  plaques with age (Fig. 3.4). Some of the A $\beta$  plaques observed in the brain at the age of 12 months were detected consistently at all ages, while the sizes of these plaques showed an increasing trend with age (Fig. 3.4).

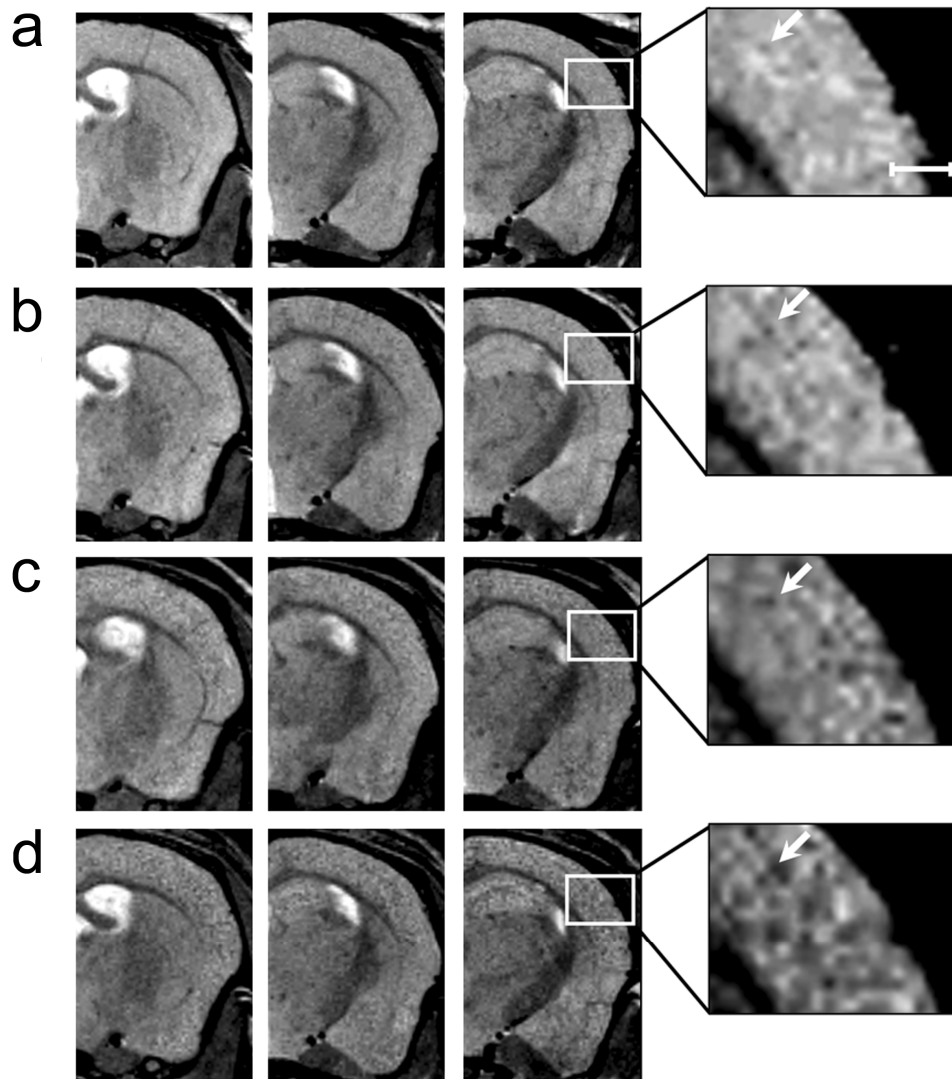


Figure 3.4: Development of A $\beta$  plaques with age in the brain of AD transgenic mouse monitored by *in vivo*  $\mu$ MRI. MR images showing successive coronal slices (left to right) of the brain of the same Tg2576 mouse at the ages of 12 months (a), 14 months (b), 16 months (c), and 18 months (d). Magnified subsampled areas on the right show an increase in plaque-load with age. Arrows indicate the same plaque seen at 12, 14, 16 and 18 months of age. Note the increase in size with age. Scale bar, 400  $\mu$ m.

Quantification of A $\beta$  plaque-load in Tg2576 mice with age is shown in Fig. 3.5a. A marked age-related increase in both plaque-load and numerical density of the A $\beta$  plaques is evident in this figure. Although the increase in numerical density of A $\beta$  plaque shows an almost linear trend from 12 to 18 months of age, the overall plaque-load shows a much more rapid increase from 16 to 18 months of age (Fig. 3.5a).

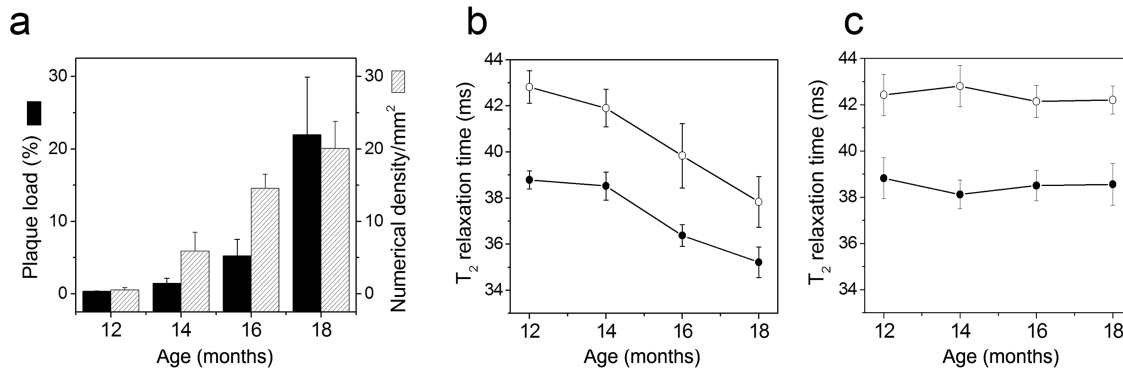


Figure 3.5: Age dependent changes in: (a) A $\beta$  plaque-load and numerical density of A $\beta$  lesions detected by  $\mu$ MRI and T<sub>2</sub> relaxation time in the hippocampus (o) and cortex (●) regions of AD transgenic mice (b) and control mice (c). Data represents a mean of n=5 ( $\pm$ SD).

An increase in the plaque-load with age was associated with a significant reduction in the mean transverse relaxation time  $T_2$  in the hippocampus and cortex of Tg2576 mice (Fig. 3.5b). A region in muscle, used as the internal control, did not show any significant change in  $T_2$  relaxation time with age. The  $T_2$  relaxation time in muscle was  $27.6 \pm 0.95$  ms at the age of 12 months, and  $27.9 \pm 0.82$  ms at the age of 18 months. A similar study using the age-matched nontransgenic control mice did not show any significant age-dependent decline in  $T_2$  relaxation time in the cortex or hippocampus (Fig. 3.5c).

### 3.5 Discussion

This study demonstrates the application of  $\mu$ MRI to resolve A $\beta$  plaque in the brain of living transgenic mouse model of AD pathology and to follow the development of the plaques in the same animals over time. Tg2576 mice overexpressing human APP<sub>695</sub> with the “Swedish” mutation develop A $\beta$  plaques and memory deficit with age, (17,25,26,27) making them suitable for longitudinal MR studies.

The  $T_2$ -weighted RARE sequence used in this study allowed clear identification of hypointense lesions corresponding to A $\beta$  plaques identified by immunohistochemistry (Fig. 3.2). Previously, a similar fast spin echo sequence has been used to visualize plaques very clearly in *ex vivo* brain of AD mice at 7T (5). Our results suggest that a similar sequence with careful adjustment of MR parameters can be applied for detection of plaques in the brain *in vivo* at a moderately higher magnetic field of 9.4T. The characteristic size of A $\beta$  plaques in Tg2576 mice varies from 20 to 150  $\mu$ m. Fig. 3.2 shows many giant plaques with sizes above 75  $\mu$ m in diameter, which is within the spatial resolution (78  $\mu$ m) of our MR experiments. Vanhoutte et al (13) have recently reported *in*

*in vivo* visualization of A $\beta$  plaques at 7T using intrinsic MRI contrast arising from the iron associated with plaques using a  $T_2^*$ -weighted 2D gradient echo sequence. One of the major limitations of their study was that the plaques were seen only in the thalamus but not in the cortex or hippocampus, which are the main areas for the A $\beta$  plaque deposition in humans as well as in all known AD transgenic mouse models. In addition, the size of the plaques in  $T_2^*$ -weighted images is often overestimated (12). Jack *et al.* (12) recently demonstrated MRI visualization of plaques *in vivo* at 9.4T in another transgenic mouse model without the use of a contrast agent and using a trigger desensitizing modification of a  $T_2$ -weighted spin echo sequence. With this method they resolved the plaques in an acquisition time as short as 1h 7 min. However, without trigger desensitizing modification or cardiorespiratory triggering, plaques could not be resolved (12). In our present study we use the multi-slice RARE method employing a single excitation step followed by the collection of multiple phase encoded echoes. With this method we have reduced the acquisition time significantly to 25 minutes and clearly identified plaques even with an in-plane resolution of 78  $\mu$ m (Figs. 3.1 and 3.4). In addition, plaques can be resolved without any cardiorespiratory triggering or trigger desensitizing modification. It is difficult to directly compare the results of this study to those of Jack *et al.* (12) due to the differences in the employed pulse sequence, as well as the different mouse models used.

The reason for plaque specific  $T_2$  contrast is not known. It has been speculated that the presence of iron in the A $\beta$  plaques may be responsible for MR contrast (5,12,13,22). Defective iron homeostasis, resulting in an increased iron level in AD brain, has been reported (9,28). In AD brain, iron is apparently mainly concentrated in amyloid plaques and may catalyze the formation of free radicals (29). The source of iron is unknown, but evidence suggests that induction of heme oxygenase, which occurs in AD, converts heme into tetrapyrrole and free iron (30). In AD such iron binds with the abnormal protein constituents of the lesions e.g. A $\beta$ . It has been shown earlier that plaque-associated iron is redox active iron and is not bound to normal iron binding proteins but to the abnormal protein constituents of the A $\beta$  lesions (19,20,24). To understand whether the presence of iron is the main reason for plaque specific  $T_2$  contrast in MR images, we examined the distribution of iron in the adjacent histological sections of the Tg2576 mouse brain. The results show that iron is associated with many dense-cored A $\beta$  plaques seen in the cortex as well as in the hippocampus (Fig. 3.3). Iron seems to be associated with the central region of the  $\beta$  amyloid deposits (Fig. 3.3). This observation is in line with earlier histochemical studies (19), which show that redox active iron is specifically localized to



the lesions of AD and not the glial cells surrounding senile plaques, which contain abundant iron binding proteins. Our results suggest that iron may be the source of the intrinsic MR contrast from A $\beta$  plaques as has been recently proposed for this mouse model (22). However, signal hypointensities arising from the reduced water content in A $\beta$  plaques compared to the surrounding tissue and from other unknown factors cannot be ruled out.

In addition to the presence of A $\beta$  plaques, the lateral ventricles are visible as hyperintense regions in the coronal MR slices of the brain of AD mouse at Bregma -2.4. At the same location in the brain of wild-type mice, only very small portion of lateral ventricles is seen (Fig. 3.1, middle row). This can be explained by the fact that AD brains show immense enlargement of the lateral ventricles due to significant loss of surrounding tissue in comparison to control brains. The ventricular enlargement in AD brains was previously shown in humans (31) and another AD mouse model (32).

As illustrated in Fig. 3.4, Tg2576 mice show a marked age-related increase in amyloid deposition in the hippocampal and cortical regions of the brain (Fig. 3.4). The plaques increase rapidly in number, in size and in the degree of compactness. Only a few circular hypointense regions corresponding to A $\beta$  plaques were observed in 12 month old Tg2576 mice, while the density of A $\beta$  deposits, seen as dark circular hypointense regions in the cortical and hippocampal region, considerably increased at 18 months (Fig. 3.4).

A quantitative estimation of A $\beta$  plaque-load and numerical density with age in the MR images shows that plaque burden increased markedly with age (Fig. 3.5a). The increase of plaque-load was more significant after 16 months than between 12-16 months. In comparison to A $\beta$  plaque-load, the numerical density of the A $\beta$  plaques shows a linear increase between 12 and 18 months. These results can be explained by a significant increase in the size of the plaques after 16 months contributing to an increase in the plaque area in the cortex and hippocampus. These results are well in line with immunohistochemical observations (16). Since the trend toward an increase in plaque burden seen by  $\mu$ MRI is clearly significant within 12 and 18 months of age, it is suggested that monitoring the effect of anti-amyloid drugs in Tg2576 mice during that time window is feasible using *in vivo*  $\mu$ MRI

A $\beta$  plaques in mice and humans are quite similar in size (up to 200  $\mu$ m). In principle, the detection of A $\beta$  plaques by MRI can be extended to human subjects. However, this would require improvement in instrumentation and MR sequences to permit imaging of human

brain with a similar contrast-to-noise ratio at a slightly lower spatial resolution, in a much shorter imaging time. With the growing awareness of the feasibility of human imaging at ultrahigh fields ( $\geq 7$ T) and improvements in RF coil technology, it may be possible to apply this approach to humans in the future (12).

The spin-spin relaxation time  $T_2$  is a specific attribute of spins that depends on their surroundings. Interaction between spins destroys the phase coherence and therefore, the  $T_2$  relaxation time can be a sensitive indicator of impaired cell physiology. A lower  $T_2$  relaxation time was previously observed in cortex and hippocampus of Tg2576 transgenic mice compared to non transgenic control (7). We followed the changes in  $T_2$  relaxation time with age in Tg2576 transgenic mice. A good correlation has been observed between increase in the plaque-load and decrease in mean transverse relaxation time  $T_2$  with age in both the hippocampus and cortex of Tg2576 mice (Fig. 3.5a and b). A similar study with age-matched non-transgenic control mice did not show any significant age dependent decline in  $T_2$  relaxation time (Fig. 3.5c). These observations suggest an influence of plaque-load on  $T_2$  reduction. Although the reason for reduction in  $T_2$  time is not yet clear, earlier studies have speculated the involvement of iron associated plaques in reducing the  $T_2$  time in AD brain (7,22).

In conclusion, we have applied  $\mu$ MRI to resolve A $\beta$  plaques in the brains of living transgenic AD mice without the aid of exogenous contrast agents in a reasonably short scanning time, and followed the development of the plaques in the same animals with age. Our results show that the developmental characteristics of A $\beta$  plaques, such as number, size and compactness can be followed with age in the same animals using *in vivo*  $\mu$ MRI. Such MR longitudinal studies may be a valuable tool for evaluating the efficiency of novel anti-amyloid treatment strategies for arresting the growth or preventing the development of new plaques using AD mouse models.

### **Acknowledgements**

The authors thank Ingrid Hegeman for her assistance with immunohistology, and Fons Lefeber and Bianca Hogers for their help with the initial MRI measurements. We are grateful to Dr. Karen Hsiao Ashe (University of Minnesota, USA) for providing the initial three Tg2576 F1 mice for further breeding. We also thank Marion Maat-Schieman and Mark van Buchem for useful discussions.

## References

1. Frank RA, Galasko D, Hampel H, et al. Biological markers for therapeutic trials in Alzheimer's disease. Proceedings of the biological markers working group; NIA initiative on neuroimaging in Alzheimer's disease. *Neurobiol Aging* 2003;24:521–536.
2. Higuchi M, Iwata N, Matsuba Y, Sato K, Sasamoto K, Saido TC. <sup>19</sup>F and <sup>1</sup>H MRI detection of amyloid- $\beta$  plaques in vivo. *Nat Neurosci* 2005;8:527–533.
3. Golde TE. Alzheimer disease therapy: can the amyloid cascade be halted? *J Clin Invest* 2003;111:11–18
4. Wengenack TM, Curran GL, Poduslo JF. Targeting Alzheimer amyloid plaques in vivo. *Nat Biotechnol* 2000;18:868–872.
5. Lee SP, Falangola MF, Nixon RA, Duff K, Helpert JA. Visualization of  $\beta$ -amyloid plaques in a transgenic mouse model of Alzheimer's disease using MR microscopy without contrast agents. *Magn Reson Med* 2004;52:538–544.
6. Benveniste H, Einstein G, Kim KR, Hulette C, Johnson GA. Detection of neuritic plaques in Alzheimer's disease by magnetic resonance microscopy. *Proc Natl Acad Sci USA* 1999;96:14079–14084.
7. Helpert JA, Lee SP, Falangola MF, et al. MRI assessment of neuropathology in a transgenic mouse model of Alzheimer's disease. *Magn Reson Med* 2004;51:794–798.
8. Zhang J, Yarowsky P, Gordon MN, et al. Detection of amyloid plaques in mouse models of Alzheimer's disease by magnetic resonance imaging. *Magn Reson Med* 2004;51:452–457.
9. Poduslo JF, Wengenack TM, Curran GL, et al. Molecular targeting of Alzheimer's amyloid plaques for contrast-enhanced magnetic resonance imaging. *Neurobiol Dis* 2002;11:315–329.
10. Wadghiri YZ, Singurdsson EM, Sadowski M, et al. Detection of Alzheimer's Amyloid in transgenic mice using magnetic resonance microimaging. *Magn Reson Med* 2003;50:293–302.
11. Skovronsky DM, Zhang B, Kung MP, Kung HF, Trojanowski JQ, Lee VMY. In vivo detection of amyloid plaques in a mouse model of Alzheimer's disease. *Proc Natl Acad Sci USA* 2000;97:7609–7614.
12. Jack CR, Garwood M, Wengenack TM, et al. In vivo visualization of Alzheimer's amyloid plaques by magnetic resonance imaging in transgenic mice without a contrast agent. *Magn Reson Med* 2004;52:1263–1271.

13. Vanhoutte G, Dewachter I, Borghgraef P, van Leuven F, Van der Linden A. Noninvasive *in vivo* MRI detection of neuritic plaques associated with iron in APP[V717I] transgenic mice, a model for Alzheimer's disease. *Magn Reson Med* 2005;53:607–613.
14. Apelt J, Kumar A, Schliebs R. Impairment of cholinergic neurotransmission in adult and aged transgenic Tg2576 mouse brain expressing the Swedish mutation of human  $\beta$ -amyloid precursor protein. *Brain Res* 2002;953:17–30.
15. Apelt J, Schliebs R.  $\beta$ -Amyloid-induced glial expression of both pro-and anti-inflammatory cytokines in cerebral cortex of aged transgenic Tg2576 mice with Alzheimer plaque pathology. *Brain Res* 2001;894:21–30.
16. Sasaki A, Shoji M, Harigaya Y, et al. Amyloid cored plaques in Tg2576 transgenic mice are characterized by giant plaques, slightly activated microglia, and the lack of paired helical filament typed, dystrophic neurites. *Virchows Arch* 2002;441:358–367.
17. Hsiao K, Chapman P, Nilsen S, et al. Correlative memory deficits, A $\beta$  elevation, and amyloid plaques in transgenic mice. *Science* 1996;274:99–103.
18. Henning J, Nauerth A, Friedburg H. RARE imaging: a fast imaging method for clinical MR. *Magn Reson Med* 1986;3:823–833.
19. Smith MA, Harris PLR, Sayre LM, Perry G. Iron accumulation in Alzheimer disease is a source of redox-generated free radicals. *Proc Natl Acad Sci USA* 1997;94:9866–9868.
20. Smith MA, Hirai K, Hsiao K, et al. Amyloid-beta deposition in Alzheimer transgenic mice is associated with oxidative stress. *J Neurochem* 1998;70:2212–2215.
21. van Balen R, Koelma D, Ten Kate TK, Mosterd B, Smeulders AWM. SCIL Image: a multi-layered environment for use and development of image processing software. In: Christensen RW, Crowley JL, editors. *Experimental environments for computer vision and image processing*. Singapore: World Scientific Publishing Co. Ltd., 1994. p 107–126.
22. Falangola MF, Lee SP, Nixon RA, Duff K, Helpert JA. Histological colocalization of iron in A $\beta$  Plaques of PS/APP transgenic mice. *Neurochem Res* 2005;30:201–205.
23. Atwood CS, Martins RN, Smith MA, Perry G. Senile plaque composition and posttranslational modification of amyloid-beta peptide and associated proteins. *Peptides* 2002;23:1343–1350.

24. Bush AI, Pettingell WH, Multhaup G, et al. Rapid induction of Alzheimer A $\beta$  amyloid formation by zinc. *Science* 1994;265:1464–1467.
25. Westerman MA, Cooper-Blacketer D, Mariash A, et al. The relationship between Abeta and memory in the Tg2576 mouse model of Alzheimer's disease. *J Neurosci* 2002;22:1858–1867.
26. Klinger M, Apelt J, Kumar A, et al. Alterations in cholinergic and non-cholinergic neurotransmitter receptor densities in transgenic Tg2576 mouse brain with  $\beta$ -amyloid plaque pathology. *Int J Dev Neurosci* 2003;21:357–369.
27. Apelt J, Bigl M, Wunderlich P, Schliebs R. Aging-related increase in oxidative stress correlates with developmental pattern of beta secretase activity and beta-amyloid plaque formation in transgenic Tg2576 mice with Alzheimer-like pathology. *Int J Dev Neurosci* 2004;22:475–484.
28. Gelman BB. Iron in CNS disease. *J Neuropathol Exp Neurol* 1995; 54:477–486.
29. Markesbery WR, Carney JM. Oxidative alterations in Alzheimer's disease. *Brain Pathol* 1999;9:133–146.
30. Salinas M, Diaz R, Abraham NG, Ruiz de Galarreta CM, Cuadrado A. Nerve growth factor protects against 6-hydroxydopamine-induced oxidative stress by increasing expression of heme oxygenase-1 in a phosphatidylinositol 3-kinase-dependent manner. *J Biol Chem* 2003;278:13898–13904.
31. Schott JM, Price SL, Frost C, Whitwell JL, Rossor MN, Fox NC. Measuring atrophy in Alzheimer disease: a serial MRI study over 6 and 12 months. *Neurology* 2005;65:119–124.
32. Feng R, Wang H, Wang J, Shrom D, Zeng X, Tsien JZ. Forebrain degeneration and ventricle enlargement caused by double knockout of Alzheimer's presenilin-1 and presenilin-2. *Proc Natl Acad Sci USA* 2004;101:8162–8167.

# 4 High resolution localized two dimensional magnetic resonance spectroscopy in mouse brain *in vivo*\*

---

## 4.1 Abstract

Localized two-dimensional magnetic resonance spectroscopy is making an impact in the *in vivo* studies of brain metabolites, due to the improved spectral resolution and unambiguous assignment opportunities. Despite the large number of transgenic mouse models available for neurological disorders, localized 2D MRS has not yet been implemented in the mouse brain due to size and sensitivity constraints. In this study we optimized a localized 2D proton chemical shift correlated spectroscopic sequence at a field strength of 9.4T to obtain highly resolved 2D spectra from localized regions in mouse brains *in vivo*. The combination of the optimized 2D sequence, high field strength, strong gradient system, efficient water suppression and the use of short echo times allowed clear detection of cross-peaks of up to 16 brain metabolites and their direct chemical shift assignments *in vivo*. To our knowledge this is the first *in vivo* 2D MRS study of the mouse brain, demonstrating its feasibility to resolve and simultaneously assign several metabolite resonances in the mouse brain *in vivo*. Implementation of 2D MRS will be invaluable in the identification of new biomarkers during disease progression and treatment using the various available mouse models of neurodegenerative disease.

## 4.2 Introduction

Proton magnetic resonance spectroscopy is an indispensable tool for noninvasive *in vivo* analysis of brain metabolites. MRS is increasingly used in the area of neurodegenerative diseases and other brain illnesses (1-2) and can be used to identify crucial *in vivo* biomarkers of these diseases (3-4). However, low concentrations of brain metabolites and difficulty in resolving the resonances of metabolites with coupled spin systems restricts the application of *in vivo* 1D MRS in identifying potential biomarkers of these diseases. In contrast to localized 1D MRS, localized two dimensional MRS reduces the problem of spectral overlap considerably, since the resonances are dispersed over a two-dimensional

---

\*This chapter was published in Magn Reson Med 2008; 60:449-456

surface rather than along a single frequency dimension. In addition, 2D MRS provides spectral assignment opportunities from correlations between pairs of related resonances. Thus, *in vivo* application of localized 2D MRS can allow separation and unambiguous assignment of resonances of several metabolites in a single measurement (5). The linear relationship between cross-peak volume and concentration has been previously used for quantification of metabolites using 2D MRS (6-8). Several studies in humans (9-12) and a few studies in rats (6,7,13) have shown promising results with localized 2D MRS by correctly distinguishing metabolites that could not be unambiguously identified using 1D MRS. However, due to a low signal-to-noise ratio, a relatively small number of molecules could be clearly detected and a large sample volume (voxel) was necessary to achieve a reasonable temporal resolution. Hence, improvement in signal-to-noise ratio of *in vivo* localized 2D MRS will be critical for exploiting its potential benefits in terms of resolution and assignment opportunities.

A large number of transgenic mouse models are currently available for various brain disorders, including neurodegenerative diseases (4). 2D MRS has not yet been implemented in mouse brain, due to its small size and associated sensitivity issues (5). Successful implementation of 2D MRS in mice, however, will be important for studies of neurological diseases, since it will enable the possibility of identifying new and potentially crucial *in vivo* biomarkers in the various transgenic mouse models available for these diseases.

In this study we implemented and optimized a PRESS-based localized 2D  $^1\text{H}$  homonuclear correlation spectroscopy sequence on a 9.4T MRI scanner using a phantom solution and obtained for the first time highly resolved localized 2D MR spectra from the living mouse brain. In comparison to the earlier *in vivo* localized 2D studies in rat brain at 7T (7), we achieved significantly higher signal-to-noise ratio in a smaller voxel of only 27  $\mu\text{l}$  and provide direct *in vivo* assignment of several brain metabolites in a single measurement in mouse brain.

### **4.3 Materials & Methods**

#### **4.3.1 Mice**

Six female C57bl6J mice aged between 5 and 6 months were used in this study. All animal experiments were approved by the Institutional Animal Care and Animal Use Committee, in accordance with the NIH Guide for the care and Use of Laboratory

Animals. For all *in vivo* MR measurements the mice were anesthetized and their respiration rate and temperature was constantly monitored as described earlier (14).

### 4.3.2 Brain phantom

As a reference for the *in vivo* measurements, a brain phantom was designed that contained 11 different brain metabolites in physiologically relevant concentrations. The phantom was made in potassium phosphate buffer (50 mM; pH 7.5) containing the following metabolites: creatine hydrate (10mM), N-acetyl-DL-aspartic acid (12.5mM), phosphocreatine sodium salt (4 mM), choline chloride (3 mM), L-glutamine (1.5 mM), L-glutamate (12.5 mM), glutathione (1.25 mM),  $\gamma$ -aminobutyric acid (1.8 mM), *myo*-inositol (7.5 mM), taurine (1 mM) and DL-lactic acid (5 mM). The final pH of the brain phantom was 7.5. All chemicals were purchased from Sigma-Aldrich Chemie BV (Netherlands).

### 4.3.3 MR spectroscopy

All measurements were conducted at 25° on a vertical wide-bore 9.4T Bruker Avance 400WB spectrometer, with a 1000 mTm<sup>-1</sup> actively shielded imaging gradient insert (Bruker BioSpin). The RF coil used was a 25 mm volume coil, specifically, a birdcage transmit/receive coil (Bruker BioSpin). The system was interfaced to a Linux pc running Topspin 1.5 and Paravision 4.0 imaging software (Bruker BioSpin).

Localized  $T_2$ -weighted multislice RARE images were acquired to select a volume of interest (voxel) as described previously (14). The MRS voxels were localized either in: (a) the middle of the mouse brain, covering predominantly the thalamus region and some parts of the hippocampus (4×4×4 mm<sup>3</sup>; 64  $\mu$ l), or (b) in the cortex-hippocampus regions in the mouse brain (1.7×4×4 mm<sup>3</sup>; 27  $\mu$ l). The local field homogeneity was optimized by adjustment of first- and second-order shim coil currents using the FASTMAP sequence. The field homogeneity in a 27-64  $\mu$ l voxel typically resulted in water line-widths of 5-11 Hz in phantoms and ~16-20 Hz in live mouse brain.

The PRESS sequence (15) was used for 1D localized 1H MR spectroscopy. This sequence uses 3 hermite RF pulses (90°, 180°, 180°). The sequence details are described by Mandal *et al.* (2). The repetition time and echo time were 1500 ms and 15 ms respectively. The PRESS sequence used 2048 complex points, with a spectral width of 10 ppm. The final 1D spectra were obtained with number of scans = 512 and scan times of approximately 13 minutes.



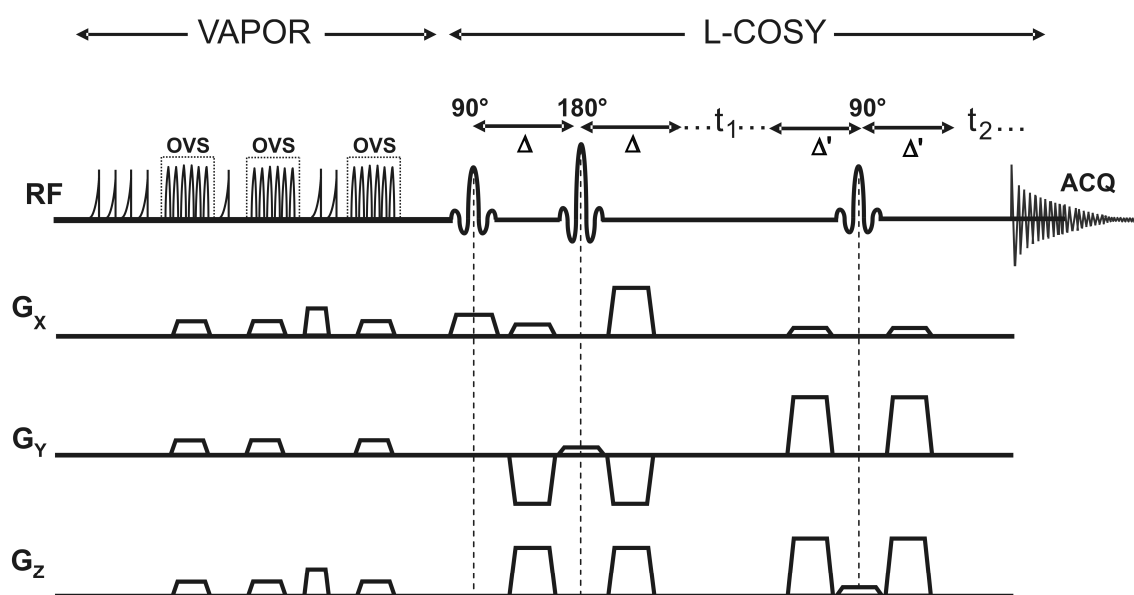


Figure 4.1. The pulse sequence of 2D L-COSY preceded by a VAPOR sequence for global water suppression interleaved with outer volume suppression. The initial value of  $TE = 15$  ms, consisting of 2 separate echo times;  $TE_1$  (6ms) and  $TE_2$  (9ms). The values of the variables in the figure are determined as follows:  $\Delta = TE_1/2$ ;  $t_1 = TE_1 + \Delta t_1$ ;  $\Delta' = TE_2/2$ .

For 2D localized MRS, the PRESS protocol was modified based on the paper of Thomas *et al.* (10) to generate a localized 2D chemical shift correlated spectroscopic sequence for the 9.4T MR spectrometer. The resulting PRESS based L-COSY sequence was integrated in the Paravision 4.0 imaging software (Bruker BioSpin) and is shown in Fig. 4.1. The sequence consists of three RF pulses ( $90^\circ$ ,  $180^\circ$ ,  $90^\circ$ ), slice-selective along 3 orthogonal axes. The last slice-selective  $90^\circ$  RF pulse also served as a coherence transfer pulse for the L-COSY spectrum necessary for correlating the metabolites peak in the second dimension. Optimized hermite  $90^\circ$  and  $180^\circ$  RF pulses with 1 ms durations were used for localization. The bandwidth of  $90^\circ$  and  $180^\circ$  RF pulses were 5.4 KHz and 3.4 KHz, respectively. A total of 16 phase cycles for all three RF pulses were used for each localized  $\Delta t_1$  increment. To achieve a short echo time of 15 ms, the duration of the spoiler gradient necessary to dephase the unwanted magnetization from outside the voxel was kept to a minimum.

Both the 1D PRESS sequence and 2D L-COSY sequences were preceded by a VAPOR sequence (16) for global water suppression. The sequence consists of 7 variable power RF pulses with an optimized relaxation delay. The relaxation delays  $\tau_1$ - $\tau_7$  between the consecutive pulses were 150, 80, 160, 80, 100, 37.11 and 57.36 ms, respectively. Water suppression bandwidth was set at 350 Hz. Outer volume suppression (OVS) was

combined in an interleaved mode with the water suppression scheme, thus improving the localization performance and reducing the demands for spoiler gradients. The OVS scheme used a total of 18 hyperbolic secant RF pulses, each with  $90^\circ$  nominal flip angle and 1 ms pulse length. The OVS slice thickness was 4 mm with a 0 mm gap to the voxel.

Localized 2D MR spectra were recorded using a TE of 15 ms ( $TE_1=6\text{ms}$  and  $TE_2=9\text{ms}$ ), and a TR of 1500 ms (Fig. 4.1). In order to obtain a feasible scan time, 2D MR spectra were recorded using 2048 complex points along  $F_2$  and 192 points (incremental excitation steps) along  $F_1$ , with a spectral width of 11 ppm and 20 averages per excitation step. This resulted in a total of 3840 scans ( $192 \Delta t_1$  increments and  $20 \text{NEX}/\Delta t_1$ ), yielding a total scan time of approximately 1 hr 36 min. For the data in the  $F_2$  direction only the first 1024 data points were used. The data in the  $F_1$  direction were zero-filled to 1024 points, yielding a square matrix. Subsequently a squared sine windowing function was applied, with a sine bell shift of 8. Spectra were symmetrized to eliminate noise and obtain clearly defined cross-peaks. Processed data are presented in magnitude mode. The *in vivo* 2D spectra were referenced to the diagonal peak of Cr at 3.02 ppm.

## 4.4 Results and discussion

### 4.4.1 *In vitro* study

Figure 4.2 shows a highly resolved 2D MR spectrum obtained from the 64  $\mu\text{l}$  voxel placed at the centre of the brain phantom. Despite low physiological concentrations of metabolites in the brain phantom and the reasonably small voxel size of 64  $\mu\text{l}$ , excellent spectral dispersion was realized at 9.4T. In addition to the resonances of total creatine which were assigned based on their diagonal peaks, 9 other metabolites can be directly assigned based on their network of cross-peaks in the 2D MR spectrum (Fig. 4.2). A summary of the assignment of metabolites is given in table 4.1 (17). The cross peak ( $H^2$ ,  $H^3$ ) of N-acetyl aspartate is not visible in Fig. 4.2. However, this cross-peak was present in the spectrum before symmetrization (data not shown) and was highly asymmetric, possibly due to the unequal effect of water suppression as also observed in previous 2D studies (6,12). As is clear from Fig. 4.2 and table 4.1, excellent separation of the cross-peaks of the methylene protons of glutamate ( $H^3-H^4$ ;  $H^{3'}-H^4$ ) and glutamine ( $H^{3'}-H^4$ ) is achieved using the 2D L-COSY sequence at 9.4 T and small 64  $\mu\text{l}$  voxel. In addition, the cross-peaks of the Glu-moiety of glutathione were clearly separated from free Glu (Fig. 4.2). The cross-peaks of Choline ( $H^1-H^2$ ) and *myo*-inositol ( $H^1-H^2$ ) which were

overlapping at 3T in a previous phantom study (12) were clearly resolved in the present study (Fig. 4.2).

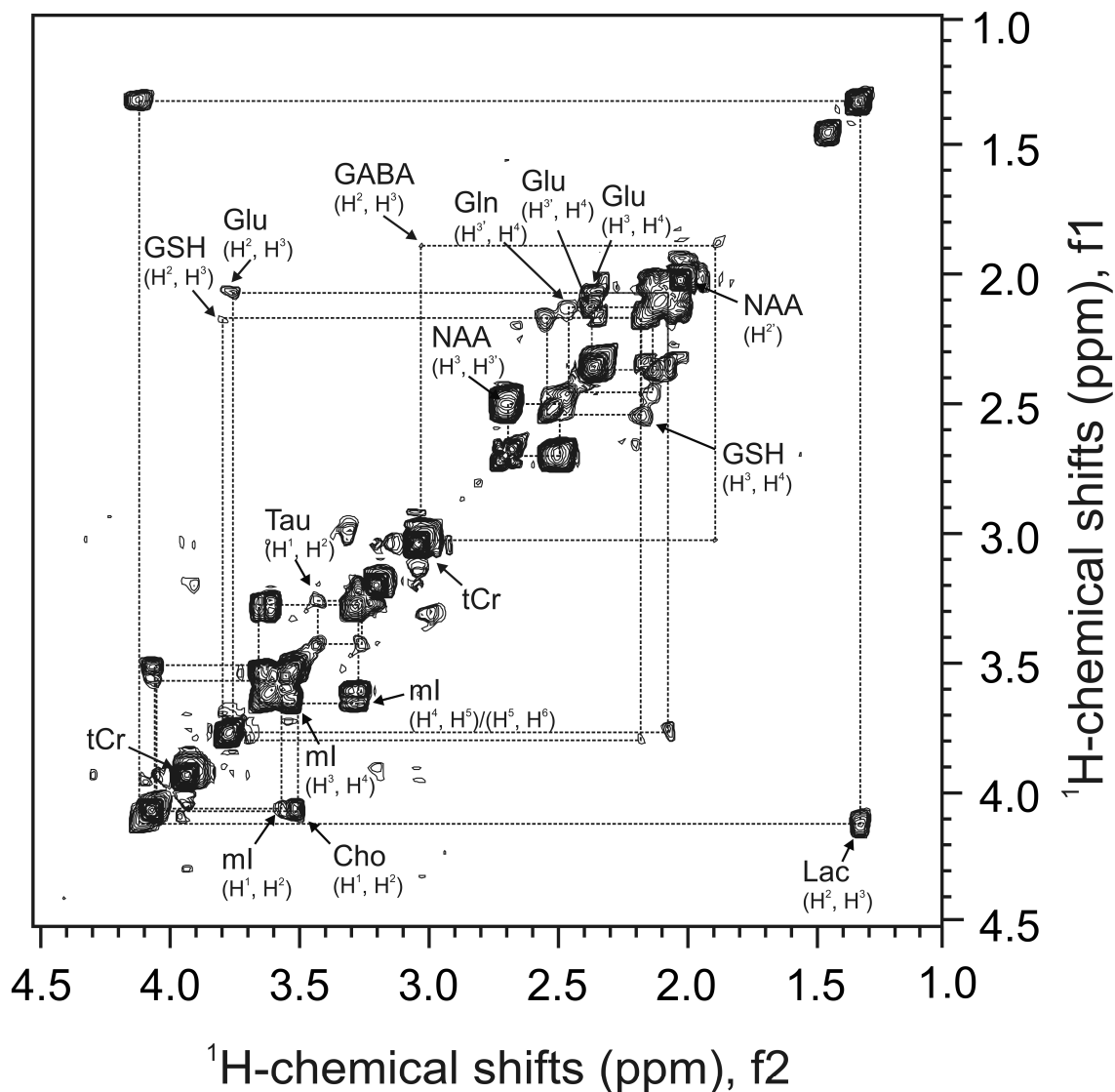


Figure 4.2. High resolution localized 2D MR spectrum obtained from  $64 \mu\text{l}$  ( $4 \times 4 \times 4 \text{ mm}^3$ ) voxel placed in a brain phantom composed of 11 brain metabolites, namely creatine, N-acetylaspartate, phosphocreatine, choline, glutamine, glutamate, glutathione,  $\gamma$ -aminobutyric acid, myo-inositol, taurine and lactate. Spectra were obtained at 9.4T using  $TR=1500 \text{ ms}$  and  $TE=15 \text{ ms}$ . The 2D data set was apodized with QSINE function and zero filled to 1024 in both dimensions. A summary of the chemical shifts assignments and cross-peaks is presented in table 4.1.

#### 4.4.2 *In vivo* study

*In vivo* high resolution localized 2D MRS was performed in the mouse brain after image guided positioning of a 64  $\mu\text{l}$  voxel ( $4 \times 4 \times 4 \text{ mm}^3$ ) in the centre of the brain, covering predominantly the thalamus region and some parts of the hippocampus, as depicted in Fig. 4.3a. A characteristic *in vivo* 1D MR spectrum of mouse brain from the same voxel is shown on top of the 2D MR spectrum in Fig. 4.3b. Generally short echo time localization methods minimize  $T_2$  relaxation effects, which increases the sensitivity and reliability of metabolite quantification (18). A short echo time of 15 ms was used for *in vivo* 2D MRS in the present study. Fig. 4.3b demonstrates how *in vivo* localized 2D MRS allowed separation of most overlapping peaks for the coupled spin systems that gave rise to off-diagonal peaks. The singlet resonance of the methyl group of NAA (2.0 ppm) appeared on the diagonal and protons from the aspartate moiety of NAA give rise to an off-diagonal peak, not contaminated by other resonances (Fig. 4.3b; table 4.1). In addition, 2D spectra showed clear separation of the cross-peaks of Glu, Gln, GSH and GABA, thus allowing the direct *in vivo* assignment of resonances of these coupled spin systems. A cross-peak at 2.35 ppm/1.95 ppm was assigned to the GABA moiety of homocarnosine, a dipeptide that consists of histidine and GABA (Fig. 4.3b). The resonances which overlap at 4.2 ppm in the 1D spectrum are resolved into cross-peaks of mI ( $\text{H}^5/\text{H}^4$ ), Tau ( $\text{H}^2/\text{H}^1$ ) and phosphorylethanolamine ( $\text{H}^2/\text{H}^1$ ) which could be clearly seen in the 2D spectrum (Fig. 4.3b). Comparison of the intensities of cross-peaks of Tau and mI reflects that the level of Tau was slightly higher than mI in the mouse brain. This is in contrast to human brain which contains 4-5 fold higher concentrations of mI than Tau (17,19). The higher level of Tau in comparison to mI in mice is consistent with levels reported by Tkac *et al.* (20) based on their 1D MRS data at 9.4T. The brain phantom used in this study contained 1 mM Tau, which is a physiologically relevant concentration for human brain. Other studies have shown that for mouse brain, a Tau concentration of up to 10 mM will be more relevant (20). The 2D spectrum in Fig. 4.3b also shows well-resolved cross-peaks of many other metabolites present in lower concentrations, such as alanine, aspartate and  $\alpha$ -glucose. As can be seen in Fig 4.4b and 4.5b, only the  $\alpha$ -anomer of glucose showed cross-peaks in the 2D spectra, despite the fact that the overall concentration of the  $\beta$ -anomer of glucose is believed to be higher in brain than that of the  $\alpha$ -anomer. Presently we are unable to explain why the  $\beta$ -glucose did not show any cross-peak. However, our results are similar to earlier *in vivo* 2D MRS studies in human (12) and rat (8) brain where cross-peaks of only  $\alpha$ -glucose were detected.

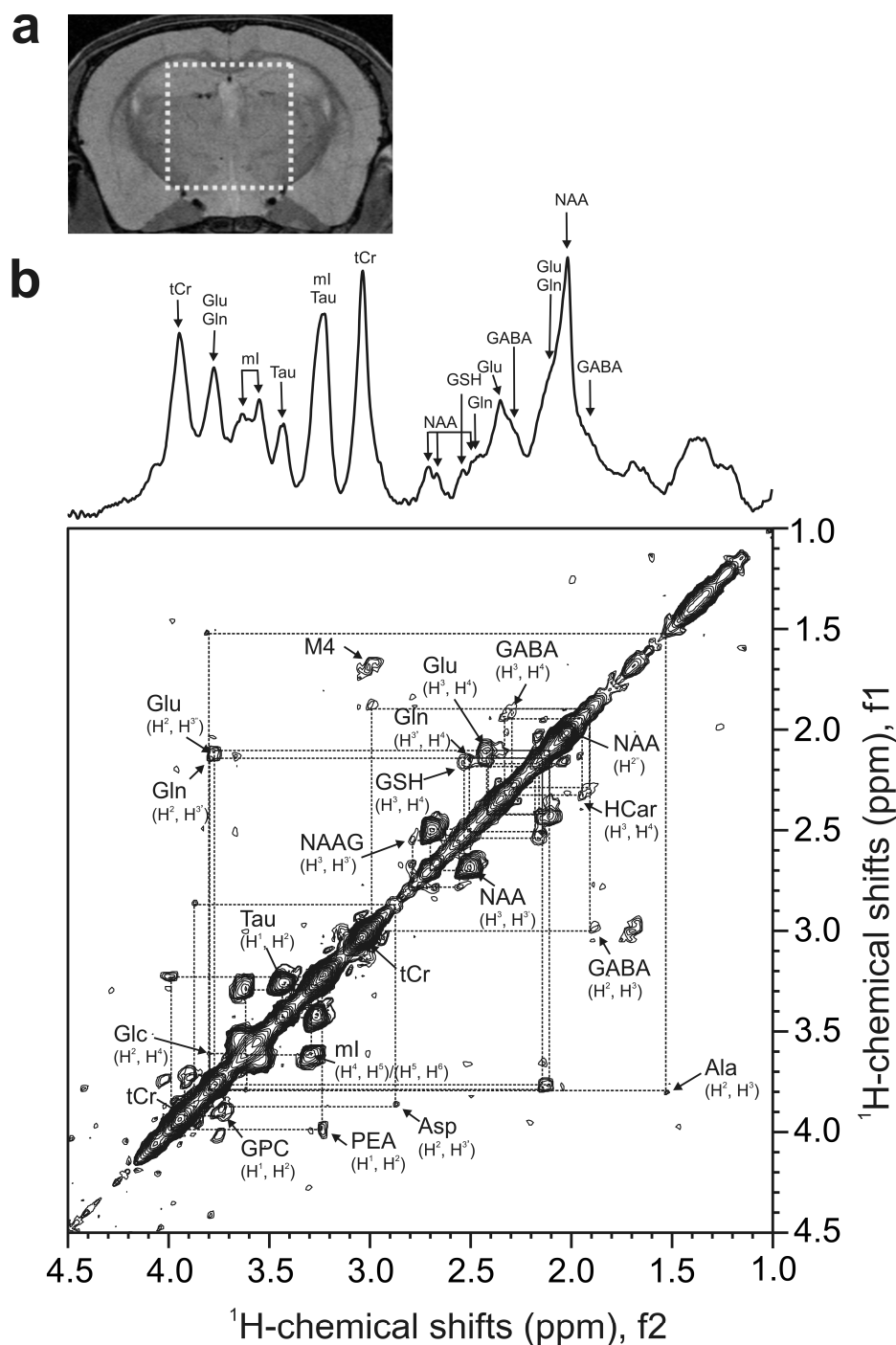


Figure 4.3. In vivo high resolution localized 2D MR spectrum from mouse brain obtained at 9.4T. (a) Coronal MR image of the mouse brain, obtained using a RARE sequence, showing the position of the selected voxel of  $64 \mu\text{l}$  ( $4 \times 4 \times 4 \text{ mm}^3$ ) covering predominantly the thalamus region and some parts of hippocampus. (b) 2D MR spectrum from the selected  $64 \mu\text{l}$  voxel in the mouse brain obtained by the PRESS based 2D L-COSY sequence as shown in Fig. 4.1. 1D spectrum from the same brain region ( $64 \mu\text{l}$  voxel) is shown on top of the 2D spectrum. Spectra were obtained using  $TR=1500 \text{ ms}$  and  $TE=15 \text{ ms}$ . The 2D data set was apodized with a QSINE function and zero filled to 1024 in both dimensions. A summary of the chemical shifts assignments and cross-peaks is presented in table 4.1. The peak M4 arises from macromolecules and is labeled in accordance with Behar and Ogino (21).

Table 4.1: Proton chemical shifts of metabolites obtained *in vivo*, in the mouse brain, or *in vitro*, in a brain phantom, from localized 2D MR spectra at 9.4T.

Metabolites	Group	<sup>1</sup> H-Chemical shift (ppm)*		Origin of cross-peaks		
		<i>In vitro</i>				
		In H <sub>2</sub> O <sup>ψ</sup>	In Phantom <sup>φ</sup>			
Ala	<sup>2</sup> CH <sub>2</sub> (H <sup>2</sup> )	3.77		3.8 <sup>a</sup>	H <sup>2</sup> -H <sup>3</sup>	
	<sup>3</sup> CH <sub>3</sub> (H <sup>3</sup> )	1.46		1.5 <sup>a</sup>		
Asp	<sup>2</sup> CH (H <sup>2</sup> )	3.89		3.9 <sup>b</sup>	H <sup>2</sup> -H <sup>3</sup>	
	<sup>3</sup> CH <sub>2</sub> (H <sup>3</sup> )	2.80		2.89 <sup>b</sup>		
Cho	<sup>1</sup> CH <sub>2</sub> (H <sup>1</sup> )	4.05	4.05		H <sup>1</sup> -H <sup>2</sup>	
	<sup>2</sup> CH <sub>2</sub> (H <sup>2</sup> )	3.50	3.50			
Glc	<sup>3</sup> CH (H <sup>3</sup> )	3.70		3.62 <sup>a</sup>	H <sup>3</sup> -H <sup>4</sup> H <sup>4</sup> -H <sup>5</sup>	
	<sup>4</sup> CH (H <sup>4</sup> )	3.40		3.4 <sup>b</sup>		
	<sup>5</sup> CH (H <sup>5</sup> )	3.82		3.80 <sup>a,b</sup>		
GABA	<sup>2</sup> CH <sub>2</sub> (H <sup>2</sup> )	3.01	3.02	3.0 <sup>a</sup>	H <sup>2</sup> -H <sup>3</sup> H <sup>3</sup> -H <sup>4</sup>	
	<sup>3</sup> CH <sub>2</sub> (H <sup>3</sup> )	1.89	1.9	1.9 <sup>a</sup> , 1.86 <sup>b</sup>		
	<sup>4</sup> CH <sub>2</sub> (H <sup>4</sup> )	2.28		2.29 <sup>a</sup> , 2.2 <sup>b</sup>		
Gln	<sup>2</sup> CH (H <sup>2</sup> )	3.75		3.8 <sup>a</sup>	H <sup>2</sup> -H <sup>3</sup> H <sup>3</sup> -H <sup>4</sup>	
	<sup>3</sup> CH <sub>2</sub> (H <sup>3</sup> )	2.13	2.13	2.17 <sup>a</sup> , 2.19 <sup>b</sup>		
	<sup>4</sup> CH <sub>2</sub> (H <sup>4</sup> )	2.45	2.46	2.49 <sup>a,b</sup>		
Glu	<sup>2</sup> CH (H <sup>2</sup> )	3.74	3.76	3.76 <sup>a</sup> , 3.78 <sup>b</sup>	H <sup>2</sup> -H <sup>3</sup> H <sup>3</sup> -H <sup>4</sup> H <sup>3</sup> -H <sup>4</sup>	
	<sup>3</sup> CH <sub>2</sub> (H <sup>3</sup> )	2.12	2.04	2.10 <sup>a</sup>		
	(H <sup>3</sup> )	2.04	2.12	2.12 <sup>a</sup> , 2.17 <sup>b</sup>		
	<sup>4</sup> CH <sub>2</sub> (H <sup>4</sup> )	2.34	2.38	2.47 <sup>a</sup> , 2.45 <sup>b</sup>		
GPC	<sup>1</sup> CH <sub>2</sub> (H <sup>1</sup> )	3.61		3.72 <sup>a,b</sup>	H <sup>1</sup> -H <sup>2</sup>	
	<sup>2</sup> CH (H <sup>2</sup> )	3.90		3.91 <sup>a,b</sup>		
Gro	<sup>1</sup> CH <sub>2</sub> (H <sup>1</sup> )	3.55		3.52 <sup>b</sup>	H <sup>1</sup> -H <sup>1</sup> H <sup>3</sup> -H <sup>3</sup>	
	(H <sup>1</sup> )	3.64		3.67 <sup>b</sup>		
	<sup>3</sup> CH <sub>2</sub> (H <sup>3</sup> )	3.55		3.52 <sup>b</sup>		
GSH	Glutamate moiety	(H <sup>3</sup> )	3.64	3.67 <sup>b</sup>		
		<sup>2</sup> CH (H <sup>2</sup> )	3.77	3.78		H <sup>2</sup> -H <sup>3</sup> H <sup>3</sup> -H <sup>4</sup>
		<sup>3</sup> CH <sub>2</sub> (H <sup>3</sup> )	2.16	2.18	2.17 <sup>a,b</sup>	
<sup>4</sup> CH <sub>2</sub> (H <sup>4</sup> )	2.56	2.55	2.55 <sup>a,b</sup>			
HCar	GABA moiety	<sup>3</sup> CH <sub>2</sub> (H <sup>3</sup> )	1.89		1.95 <sup>a</sup>	H <sup>3</sup> -H <sup>4</sup>
		<sup>4</sup> CH <sub>2</sub> (H <sup>4</sup> )	2.37		2.35 <sup>a</sup>	
Lac		<sup>2</sup> CH (H <sup>2</sup> )	4.10	4.11	4.14 <sup>b</sup>	H <sup>2</sup> -H <sup>3</sup>
		<sup>3</sup> CH <sub>3</sub> (H <sup>3</sup> )	1.31	1.31	1.33 <sup>b</sup>	
mI		<sup>1</sup> CH (H <sup>1</sup> )	3.52	3.56		H <sup>1</sup> -H <sup>2</sup> H <sup>2</sup> -H <sup>3</sup> H <sup>3</sup> -H <sup>4</sup> H <sup>4</sup> -H <sup>5</sup> H <sup>5</sup> -H <sup>6</sup>
		<sup>2</sup> CH (H <sup>2</sup> )	4.05	4.05		
		<sup>3</sup> CH (H <sup>3</sup> )	3.52	3.56		
		<sup>4</sup> CH (H <sup>4</sup> )	3.61	3.67	3.62 <sup>a,b</sup>	
		<sup>5</sup> CH (H <sup>5</sup> )	3.27	3.27	3.29 <sup>a</sup> , 3.25 <sup>b</sup>	
		<sup>6</sup> CH (H <sup>6</sup> )	3.61	3.67	3.62 <sup>a,b</sup>	
NAA	Acetyl moiety	<sup>2</sup> CH <sub>3</sub> (H <sup>2</sup> )	2.01	2.04	2.02 <sup>a,b</sup>	H <sup>3</sup> -H <sup>3</sup>
	Aspartate moiety	<sup>3</sup> CH <sub>2</sub> (H <sup>3</sup> )	2.67	2.67	2.70 <sup>a,b</sup>	
		(H <sup>3</sup> )	2.49	2.5	2.50 <sup>a,b</sup>	
NAAG	Aspartate moiety	<sup>3</sup> CH <sub>2</sub> (H <sup>3</sup> )	2.72		2.78 <sup>a</sup> , 2.74 <sup>b</sup>	H <sup>3</sup> -H <sup>3</sup>
		(H <sup>3</sup> )	2.52		2.55 <sup>a</sup> , 2.51 <sup>b</sup>	
PEA		<sup>1</sup> CH <sub>2</sub> <sup>2</sup> (H <sup>1</sup> )	3.98		3.98 <sup>a</sup>	H <sup>1</sup> -H <sup>2</sup>
		CH <sub>2</sub> (H <sup>2</sup> )	3.22		3.27 <sup>a</sup>	
Tau		<sup>1</sup> CH <sub>2</sub> (H <sup>1</sup> )	3.42	3.42	3.42 <sup>a,b</sup>	H <sup>1</sup> -H <sup>2</sup>
		<sup>2</sup> CH <sub>2</sub> (H <sup>2</sup> )	3.25	3.26	3.25 <sup>a,b</sup>	
Thr		<sup>2</sup> CH (H <sup>2</sup> )	3.58		3.52 <sup>b</sup>	H <sup>2</sup> -H <sup>3</sup>
		<sup>3</sup> CH (H <sup>3</sup> )	4.25		4.2 <sup>b</sup>	
Tyr		<sup>α</sup> CH (H <sup>α</sup> )	3.93		3.88 <sup>b</sup>	H <sup>α</sup> -H <sup>β</sup> H <sup>α</sup> -H <sup>β</sup>
		<sup>β</sup> CH <sub>2</sub> (H <sup>β</sup> )	3.19		3.1 <sup>b</sup>	
		<sup>β</sup> CH <sub>2</sub> (H <sup>β</sup> )	3.04		3.0 <sup>b</sup>	

<sup>ψ</sup>Govindaraju et al (17); <sup>φ</sup>This work; \*Estimated accuracy ±0.05ppm.

<sup>a</sup>Proton resonances seen *in vivo* in a 64 μl voxel covering predominantly the thalamus region

<sup>b</sup>Proton resonances seen *in vivo* in a 27 μl voxel placed in cortex/hippocampus region.

A complete map of the *in vivo* resonances of the observed cross-peaks is depicted in table 4.1. A strong cross-peak at 3.0 ppm/1.7 ppm is assigned to macromolecules (M4) according to Behar and Ogino (21). It has been shown earlier that the contribution of macromolecule resonances increases rapidly with decreasing echo time (16). Stronger signals from macromolecules in Fig. 4.3b might have been due to the use of a short echo time of 15 ms in the present studies.

While a large voxel as shown in Fig. 4.3b gave better signal-to-noise ratio in 2D spectra, a small voxel would be necessary to achieve regional specificity in the mouse brain. Especially localized information from regions such as the cortex and hippocampus which are more severely affected during neurodegenerative diseases would be invaluable. Figure 4.4b shows an *in vivo* 2D MR spectrum obtained from a smaller voxel ( $1.7 \times 4 \times 4$  mm<sup>3</sup>; 27  $\mu$ l) that was positioned in the cortex and hippocampus region as shown in Fig. 4.4a. Despite the small size of the voxel, the signal-to-noise ratio was sufficient to allow separation of most overlapping peaks, which resulted in clear identification and assignment of 15 brain metabolites. This was possible due to excellent localization performance, successful first and higher order shimming, efficient water suppression and careful optimization of acquisition parameters at high magnetic field (9.4T). Cross-peaks of Glu, Gln and GSH were clearly separated. In addition, the cross-peak of NAAG was separated from NAA (Fig. 4.4b). NAAG is the most abundant peptide neurotransmitter in the human brain (17), and consists of NAA with a peptide bond to Glu. It is difficult to differentiate NAAG from NAA and Glu by *in vivo* 1D MRS. Recently, Edden *et al.* (22) have used the MEGA-PRESS sequence to selectively separate the aspartyl spin system of NAA and NAAG. However, due to a low signal-to-noise ratio, a large voxel was necessary to observe the signal from NAAG. Moreover, only one spin system could be monitored at a time. As shown in Fig. 4.4b, using 2D MRS at high magnetic field, we could separate the cross-peaks between aspartyl  $\beta$ -protons of NAA (2.70, 2.50 ppm) and NAAG (2.74, 2.51 ppm) in the same spectrum from the living mouse brain and could simultaneously detect many other metabolites in a single data set. Well resolved cross-peaks from mI and Tau were also detected. Interestingly, the Tau/mI ratio is even higher in the cortex-hippocampus region (Fig. 4.4b) than in the centre of the brain covering predominantly the thalamus region (Fig. 4.3b). This is evident from the intensities of the cross-peaks of these two metabolites in the cortex-hippocampus, suggesting that the cortex and hippocampus of the mouse brain contain very high concentrations of Tau in comparison to mI. The 2D MR spectrum also shows cross-peaks of  $\alpha$ -glucose, tyrosine, threonine, and glycerol (Fig. 4.4b). Similar to previous studies (6,12), not all cross-peaks

of these metabolites could be easily detected. Three cross-peaks labeled as U1, U2 and U3 were also observed (Fig. 4.4b) which could not be assigned to any of the 35 known brain metabolites (17).

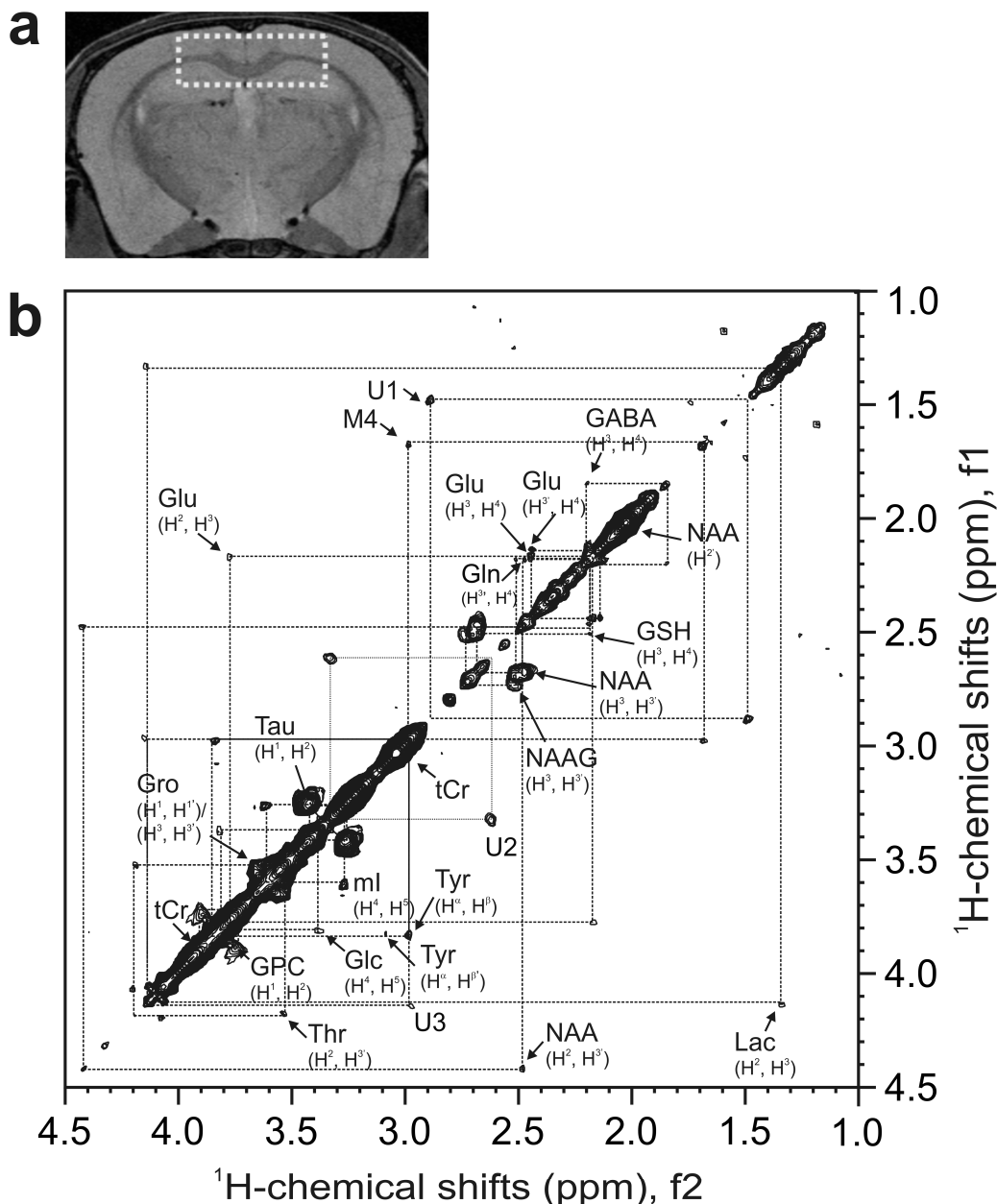


Figure 4.4. *In vivo* high resolution localized 2D MR spectrum from the cortex-hippocampus region of the mouse brain obtained at 9.4T. (a) Coronal MR image of the mouse brain, obtained using a RARE sequence, showing the position of the selected voxel of  $27 \mu\text{l}$  ( $1.7 \times 4 \times 4 \text{ mm}^3$ ) covering the cortex-hippocampus region. (b) 2D MR spectrum from the selected  $27 \mu\text{l}$  voxel in the cortex-hippocampus region of the mouse brain obtained by the PRESS based 2D L-COSY sequence as shown in Fig. 4.1. The spectrum was obtained using  $\text{TR}=1500 \text{ ms}$  and  $\text{TE}=15 \text{ ms}$ . The 2D data set was apodized with a QSINE function and zero filled to 1024 in both dimensions. A summary of the chemical shifts assignments and cross-peaks is presented in table 4.1. U1, U2 and U3 are unassigned cross-peaks. The peak M4 arises from macromolecules and is labeled in accordance with Behar and Ogino (21).



Further studies would be needed to assign these resonances to new metabolites or macromolecules present in the cortex-hippocampus region of the mouse brain. The *in vivo* resonance assignment of metabolites in the cortex-hippocampus region of mouse brain is summarized in table 1.

In general, in comparison to 2D MRS, 1D MRS is a more efficient method for absolute quantification of metabolites when it is combined with data analysis methods such as LCmodel. For example 16 brain metabolites were quantified in mouse brain using this method (20). Two dimensional MRS, however, allows unambiguous visualization of cross-peaks and thus has great potential to unearth unknown brain metabolites so far hidden under overlapping multiplets (7) which will have significant implication in detecting new biomarkers of various brain diseases in future.

In conclusion, the results presented in this paper clearly demonstrate the feasibility of 2D MRS in combination with high magnetic field (9.4T) to get localized access to the mouse brain for efficient identification of metabolites. A large number of metabolites were assigned simultaneously without contamination based on their network of cross-peaks in localized regions of the mouse brain *in vivo*. These results suggest that localized 2D  $^1\text{H}$  MRS at high field strength can offer a better scope for identifying potential biomarkers of neurological diseases using a variety of transgenic mouse models.

### **Acknowledgements**

The authors thank Kees Erkelens and Fons Lefeber for their assistance during various stages of MRS measurements. This research project was supported in part by funds from Internationale Stichting Alzheimer Onderzoek (ISAO), CYTTRON within the Bsik program (Besluit subsidies investeringen kennisinfrastructuur) and the Centre for Medical Systems Biology (CMSB).

### **References**

1. Kantarci K, Petersen RC, Boeve BF, Knopman DS, Tang-Wai DF, O'Brien PC, Weigand SD, Edland SD, Smith GE, Ivnik RJ, Ferman TJ, Tangalos EG, Jack CR.  $^1\text{H}$  MR spectroscopy in common dementias. *Neurology* 2004;63:1393-1398.
2. Mandal PK. Magnetic resonance spectroscopy (MRS) and its application in Alzheimer's disease. *Conc Magn Reson A* 2007;30A:40-64.

3. Marjanska M, Curran GL, Wengenack TM, Henry PG, Bliss RL, Poduslo JF, Jack CR Jr, Ugurbil K, Garwood M. Monitoring disease progression in transgenic mouse models of Alzheimer's disease with proton magnetic resonance spectroscopy. *Proc Natl Acad Sci USA* 2005;102:11906-11910.
4. Choi J-K, Dedeoglu A, Jenkins BG. Application of MRS to mouse models of neurodegenerative illness. *NMR Biomed* 2007;20:216-237.
5. Meric P, Autret G, Doan BT, Gillet B, Sebric C, Beloeil JC. *In vivo* 2D magnetic resonance spectroscopy of small animals. *Magn Reson Mat Phys Biol Med* 2004;17:317-338.
6. Delmas F, Beloeil JC, van der Sanden BPJ, Nicolay K, Gillet B. Two-voxel localization sequence for *in vivo* two-dimensional homonuclear correlation spectroscopy. *J Magn Reson* 2001;149:119-125.
7. Welch JWR, Bhakoo K, Dixon RM, Styles P, Sibson NR, Blamire AM. *In vivo* monitoring of rat brain metabolites during vigabatrin treatment using localized 2D-COSY. *NMR Biomed* 2003;16:47-54.
8. Peres M, Fedeli O, Barrere B, Gillet B, Berenger G, Seylaz J, Beloeil J-C. *In vivo* identification and monitoring of changes in rat brain glucose by two-dimensional shift correlated NMR spectroscopy. *Magn Reson Med* 1992;27:356-361.
9. Thomas MA, Ryner LN, Mehta MP, Turski PA, Sorenson JA. Localized 2D J-resolved  $^1\text{H}$  MR spectroscopy of human brain. *J Magn Reson Imaging* 1996;6: 453-459.
10. Thomas MA, Yue K, Binesh N, Davanzo P, Kumar A, Siegel B, Frye M, Curran J, Lufkin R, Martin P, Guze B. Localized two-dimensional shift correlated MR spectroscopy of human brain. *Magn Reson Med* 2001;46:58-67.
11. Ziegler A, Gillet B, Beloeil J, Macher J, Decorps M, Nedelec J. Localized 2D correlation spectroscopy in human brain at 3T. *MAGMA* 2001;14:45-49.
12. Thomas MA, Hattori N, Umeda M, Sawada T, Naruse S. Evaluation of two-dimensional L-COSY and PRESS using a 3 T MRI scanner: from phantoms to human brain *in vivo*. *NMR Biomed* 2003;16:245-251.
13. Von Kienlin M, Ziegler A, Le Fur Y, Rubin C, Decorps M, Remy C. 2D-spatial/2D-spectral spectroscopic imaging of intracerebral gliomas in rat brain. *Magn Reson Med* 2000;43:211-219.
14. Braakman N, Matysik J, van Duinen SG, Verbeek F, Schliebs R, de Groot HJM, Alia A. Longitudinal Assessment of Alzheimers  $\beta$ -amyloid plaque Development in Transgenic Mice Monitored by *In vivo* Magnetic Resonance Microimaging. *J Magn Reson Imaging* 2006;24:530-536.

15. Bottomley PA. Spatial localization in NMR spectroscopy *in vivo*. Ann N Y Acad Sci. 1987;508:333-348.
16. Tkac I, Starcuk Z, Choi IY, Gruetter R. *In vivo*  $^1\text{H}$  NMR spectroscopy of rat brain at 1 ms echo time. Magn Reson Med 1999;41:649-656.
17. Govindaraju V, Young K, Maudsley AA. Proton NMR chemical shifts and coupling constants for brain metabolites. NMR Biomed 2000;13:129-153.
18. Pfeuffer J, Tkac I, Provencher SW, Gruetter R. Toward an *in vivo* neurochemical profile: quantification of 18 metabolites in short echo-time  $^1\text{H}$  NMR spectra of the rat brain. J Magn Reson 1999;141:104–120.
19. van Zijl PCM, Barker PB. Magnetic resonance spectroscopy and spectroscopic imaging for the study of brain metabolism. Ann NY Acad Sci 1997;820:75-96.
20. Tkac I, Henry PG, Andersen P, Keene CD, Low WC, Gruetter R. Highly resolved *in vivo*  $^1\text{H}$  NMR spectroscopy of the mouse brain at 9.4 T. Magn Reson Med 2004;52:478-484.
21. Behar KL, Ogino T. Characterization of macromolecule resonances in the  $^1\text{H}$ -NMR spectrum of rat brain. Magn Reson Med 1993;30:38-44.  
Edden RAE, Pomper MG, Barker PB. *In vivo* differentiation of N-acetyl aspartyl glutamate from N-acetyl aspartate at 3 Tesla. Magn Reson Med 2007;57:977-982.

# 5 Correlation between the severity of amyloid- $\beta$ deposition and altered neurochemical profile in a transgenic mouse model of Alzheimer's disease, observed by $\mu$ MRI and high resolution two-dimensional MRS\*

---

## 5.1 Abstract

Localized two-dimensional magnetic resonance spectroscopy was applied in combination with high resolution  $\mu$ MRI to follow the exact sequential relationship between the severity of A $\beta$  deposition and altered neurochemical profile with age in the brain of a transgenic mouse model of Alzheimer's disease. Localized 2D MR spectra obtained from the cortex-hippocampus area of the 18 month old transgenic mice show a significant alteration in a number of neurometabolites. N-acetylaspartate, glutamate and glutathione show a clear decline, while the level of taurine shows an increase in AD mice as compared to controls. In addition, a significant increase (~75%) was detected in the level of glycerophosphocholine in AD mice. A correlation between age dependent changes in the level of GPC measured by 2D MRS and severity of A $\beta$  deposition visualized by  $\mu$ MRI has been followed in the same transgenic mice. Our results show that the increase in GPC with age in transgenic mice is directly correlated with the severity of plaque deposition up to 18 months of age. Interestingly the level of GPC drops drastically at the age of 20 months, which may signify gross membrane impairment at later stages of AD. This study provides the first direct *in vivo* evidence for the increase in GPC in plaque affected areas and suggests that altered GPC may be a valuable marker for early diagnosis and for testing therapeutics in the AD mouse model.

## 5.2 Introduction

Alzheimer's disease is the most common form of dementia, afflicting mainly the elderly. With the rapid aging of western societies, this disease is set to become a major problem in healthcare. Currently several methods are employed in attempts to diagnose AD; In

addition to psychological examination and examination of metabolite levels from collected blood samples, several neuroimaging techniques have been employed in an attempt to visualize AD pathological hallmarks (see Chapter 1). However, a definitive diagnosis of AD is only possible post-mortem, by detecting the two hallmarks of the disease- amyloid plaques and neurofibrillary tangles in the brain tissue (1). There is thus a great need for biomarkers to diagnose AD with high specificity and sensitivity in a clinical setting in humans, as well as in transgenic animal models for preclinical drug research.

Proton magnetic resonance spectroscopy provides a non-invasive way to investigate *in vivo* neurochemical abnormalities of many brain disorders. Several groups have applied MRS in the study of AD, both in transgenic mice (2-4) and in humans (5-10). In these studies the most commonly altered metabolites in AD were *myo*-inositol, taurine, glutamate, glutamine and N-acetylaspartate. Although a decrease in NAA, glutamate, glutamine and an increase in *myo*-inositol or taurine has been consistently observed in AD, these changes are not specific to only AD, since they have been shown to occur in other neurodegenerative diseases such as Huntington's disease (11,12), Parkinson's disease (13,14) as well as in other brain disorders (15-17). Therefore, specific *in vivo* MRS markers of AD are still missing. While transgenic mouse models of AD might be instrumental in discovering new *in vivo* biomarkers of AD, the use of localized *in vivo* 1D MRS in mice is often hampered by low sensitivity of local measurements due to both the small size of the brain resulting in limited signal-to-noise ratio and low concentrations of several brain metabolites. In addition a considerable overlap of peaks of metabolites with coupled spin systems restrict the number of molecules which can be uniquely assigned in 1D MRS (18).

To overcome the problem of spectral resolution and peak overlap, we have recently employed a 2D MRS at 9.4T and obtained the first highly resolved localized 2D MR spectra from the hippocampus-cortex regions of the living mouse brain (Chapter 4). Due to spreading of resonances in two dimensional surfaces, a large number of metabolites were unambiguously assigned based on their network of cross-peaks in localized region of the mouse brain *in vivo*. These results show that localized 2D MRS at high field strength can offer a better scope for identifying potential biomarkers of various brain diseases, including AD, using the various available transgenic mouse models.

In the present study we have mapped the neurochemical composition of transgenic AD mice and control mice, and followed the neurochemical changes with age in the same

animals, using high resolution localized 2D MRS. A noteworthy finding in this study was an increase in the level of GPC in Tg2576 mice compared to control mice. A correlation between age dependent changes in the level of GPC measured by 2D MRS and severity of A $\beta$  deposition visualized by  $\mu$ MRI has been followed in the same transgenic mice. Our results show that the age-dependent increase in GPC in transgenic mice correlates well with the severity of plaque deposition. Altered GPC levels may be a valuable marker to test therapeutics in the AD mouse model.

### **5.3 Materials & methods**

#### **5.3.1 Transgenic mice**

The transgenic mice used in this study contain as transgene the Swedish double mutation of the human amyloid precursor protein (APP<sub>695</sub>), as developed and described previously by Hsiao *et al.* (19). The transgene is expressed in C57B6 breeders. The N2 generation mice of both genders (n=30) were studied at ages between 8 and 24 months. Age-matched non-transgenic littermates served as controls. All animal experiments were approved by the Institutional Animal Care and Animal Use Committee in accordance with the NIH Guide for the care and Use of Laboratory Animals. For all *in vivo* MR measurements the mice were anesthetized using Isoflurane (Forene, Abott, UK) inhalation anesthesia, together with air and oxygen (1:1) at 0.3 l/minute. The anesthetic gas was administered via a special face mask, which also served as a fixation device for the mouse head by coupling it with a specially designed toothbar to hold the head in place (Bruker Biospin). While inside the probe, the respiration rate of the mouse was constantly monitored by means of a pressure transducer placed on the abdomen. The transducer was connected to an SA Instruments MR compatible small animal monitoring and gating system, which was interfaced to an SA Instruments command module and laptop running SAM PC monitoring software (SA Instruments, Inc. Stony Brook, NY, USA).

#### **5.3.2 MR Measurements**

All  $\mu$ MRI and 1D & 2D MRS measurements were conducted at 25° on a vertical wide-bore 9.4T Bruker Avance 400WB spectrometer, with a 1000 mTm<sup>-1</sup> actively shielded imaging gradient insert (Bruker BioSpin). The RF coil used was a 25 mm volume coil, specifically, a birdcage transmit/receive coil (Bruker BioSpin). The system was interfaced to a Linux pc running Topspin 1.5 and Paravision 4.0 imaging software (Bruker BioSpin).

***μMRI***

All μMRI measurements were done using a RARE sequence (20) which employs a single excitation step followed by the collection of multiple phase encoded echoes. Basic measurement parameters used for the RARE sequence were: TE = 10.567 ms (22.45 ms effective), TR = 6 s, flip angle = 90°, NA = 4, RARE factor (echo train length) = 4. The field of view was 2.00 × 2.00 cm<sup>2</sup>, with image matrix of 256 × 256. This yields an effective in-plane resolution of approximately 78 μm. Coronal (transverse) images were obtained with a slice thickness of 0.5 mm in a total scan time of approximately 25 minutes.

***MR spectroscopy***

To select a volume of interest, localized  $T_2$ -weighted images were acquired using the RARE sequence as described above. The MRS voxels were localized either in: (a) the middle of the mouse brain, covering predominantly the thalamus region and some parts of the hippocampus (4×4×4 mm<sup>3</sup>; 64 μl), or (b) in the cortex-hippocampus regions in the mouse brain (1.7×4×4 mm<sup>3</sup>; 27 μl). The local field homogeneity was optimized by adjustment of first- and second-order shim coil currents using the FASTMAP sequence. The field homogeneity in a 27-64 μl voxel typically resulted in water line-widths of ~16-20 Hz in live mouse brain.

The PRESS sequence (21) was used for localized 1D MR spectroscopy. This sequence uses 3 hermite RF pulses (90°, 180°, 180°). The sequence details are described by Mandal et al. (22). The repetition time and echo time were 1500 ms and 15 ms respectively. The PRESS sequence used 2048 complex points, with a spectral width of 11 ppm. The 1D spectra were collected in 512 scans with a scan time of approximately 13 minutes.

The localized 2D MRS was measured using the 2D L-COSY sequence (18) as described in Chapter 4. The sequence consists of three RF pulses (90°, 180°, 90°), slice-selective along 3 orthogonal axes. The last slice-selective 90° RF pulse also served as a coherence transfer pulse for the L-COSY spectrum necessary for correlating the metabolites peak in the second dimension. Optimized hermite 90° and 180° RF pulses with 1 ms durations were used for localization. The bandwidth of 90° and 180° RF pulses were 5.4 KHz and 3.4 KHz, respectively. A total of 16 phase cycles for the three RF pulses were used for each localized  $\Delta t_1$  increment. To achieve a short echo time of 15 ms, the duration of the spoiler gradient necessary to dephase the unwanted magnetization from outside the voxel was kept to a minimum. Both the 1D PRESS sequence and 2D L-COSY sequence were

preceded by a VAPOR sequence (23) for global water suppression. The sequence consists of 7 variable power RF pulses with an optimized relaxation delay. The relaxation delays  $\tau_1$ - $\tau_7$  between the consecutive pulses were 150, 80, 160, 80, 100, 37.11 and 57.36 ms, respectively. The water suppression bandwidth was set at 350 Hz. Outer volume suppression was combined in an interleaved mode with the water suppression scheme, thus improving the localization performance and reducing the demands for spoiler gradients. The OVS scheme used a total of 18 hyperbolic secant RF pulses, each with 90° nominal flip angle and 1 ms pulse length. The OVS slice thickness was 4 mm with a 0 mm gap to the voxel.

Localized 2D MR spectra were recorded using a TE of 15 ms ( $TE_1=6$ ms and  $TE_2=9$ ms), and a TR of 1500 ms (Fig. 5.1). In order to obtain a feasible scan time, 2D MR spectra were recorded using 2048 complex points along  $F_2$  and 192 incremental steps along  $F_1$ , with a spectral width of 11 ppm and 20 averages per excitation step. This resulted in a total of 3840 scans (192  $\Delta t_1$  increments and 20 NEX/ $\Delta t_1$ ), yielding a total scan time of approximately 1 hr 36 min. For the data in the  $F_2$  direction only the first 1024 data points were used. The data in the  $F_1$  direction was zero-filled to 1024 points, yielding a square matrix. Subsequently a squared sine windowing function was applied, with a sine bell shift of 8. For presentation spectra were symmetrized to eliminate noise and obtain clearly defined cross-peaks. Processed data is presented in magnitude mode. All 2D spectra were referenced to the diagonal peak of tCr at 3.02 ppm. Further assignments are based on the study by Govindaraju *et al.* (24)

### 5.3.3 Data Processing and Analysis

A $\beta$  plaque-load and numerical density in MR images were quantified by SCIL image software (25) as described in Chapter 3.

Localized 1D MR spectra were analyzed by using LCModel (26), which calculates the best fit of the experimental spectrum based on a linear combination of model spectra. The final analysis is performed in the frequency domain; however, raw data (FIDs) are used as standard data input. The following metabolites were included in the basis set for LCModel: alanine, aspartate, creatine,  $\gamma$ -aminobutyric acid, glucose, glutamate, glutamine, glycerophosphocholine, phosphocholine, *myo*-inositol, lactate, N-acetylaspartate, N-acetylaspartylglutamate, phosphocreatine, phosphoethanolamine, *scyllo*-inositol, and taurine. Quantification was obtained by using the tCr resonance as an internal standard. The LCModel fitting was performed over the spectral range from 1.0 to 4.4 ppm.



Metabolites in the localized 2D spectra were quantified by calculating the cross-peak volumes of properly scaled non-symmetrized 2D data sets using Sparky NMR assignment and integration software (T.D. Goddard & D.G. Kneller; Sparky 3, University of California, San Francisco). Volume calculation was achieved using the sum 'over ellipse' integration method, allowing linewidths to be adjusted and the baseline to be fit. Additionally, only data above the lowest contour was used for quantification. Manual selection and integration afforded better reproducibility than with the automatic peak selection and integration techniques in the Sparky analysis software.

#### 5.4 Results & Discussion

Figures 5.1b and 5.1c show characteristic 1D MR spectra obtained from a 27  $\mu$ l voxel placed in the cortex-hippocampus area of the brain of an 18 month old control and a transgenic mouse of the same age, as illustrated in Fig. 5.1a. The most significant changes were increased taurine and decreased NAA and Glutamate in the cortex and hippocampus of transgenic mice, compared to the WT. The quantification of MR spectra revealed an increase in the taurine/Cr ratio of  $\sim$ 20% and a decrease in the NAA/Cr and Glu/Cr ratios of  $\sim$ 18 and  $\sim$ 24%, respectively, in the transgenic mice compared to control mice. Similar neurochemical changes have been observed in the cingulate cortex in previous MRS studies using the same mouse model of AD at 4.7T (2) and at 9.4T (3). In another transgenic mouse model of AD, APP/PS1 mice, Marjanska *et al.* have observed an increase in *myo*-inositol instead of taurine compared to control mice (3). They proposed that the ratio of NAA and *myo*-inositol might be a sensitive spectroscopic marker for following AD in human disease as well as in mouse models such as the APP/PS1.

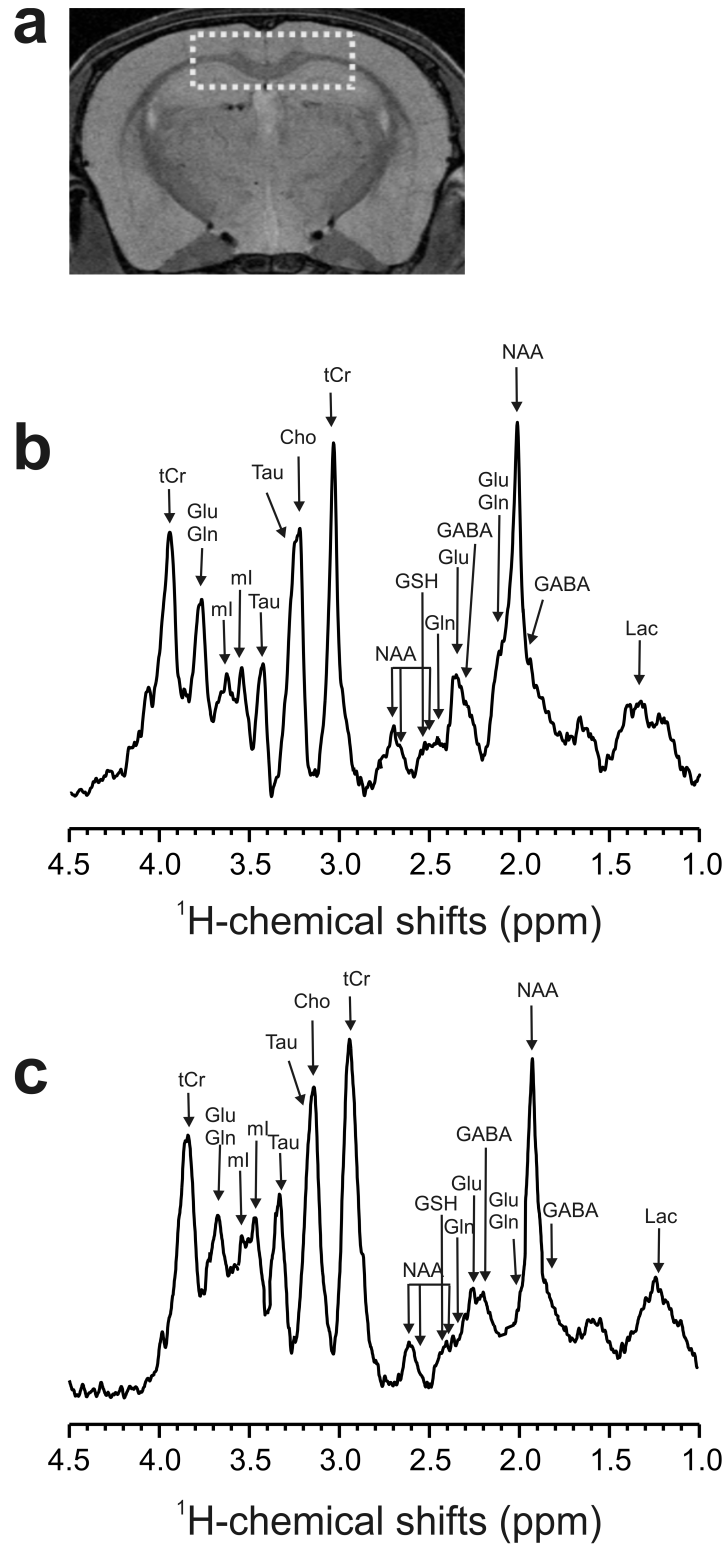


Figure 5.1: Representative MR image and spectra of the mouse brain. (a) A coronal MR image of the mouse brain, obtained using a RARE sequence, showing the position of the selected 27  $\mu$ l ( $1.7 \times 4 \times 4$  mm<sup>3</sup>) voxel covering the cortex-hippocampus region. One-dimensional localized <sup>1</sup>H-MR spectra obtained from the selected 27  $\mu$ l voxel placed in the brain of an 18 month old control (b) and AD (c) mouse. Spectra were obtained using a PRESS sequence with TR=1500 ms and TE=15 ms at 9.4T.

Although a decrease in NAA and glutamate and an increase in *myo*-inositol or taurine have been consistently observed in AD brain, these changes are not specific to only AD, since they have been shown to occur in other neurodegenerative diseases such as Huntington's disease (11,12), Parkinson's disease (13,14) as well as in other brain disorders (15-17). Since only a limited number of metabolites can be reliably detected with 1D MRS, several metabolites and neurotransmitters that are present in low concentrations cannot be unambiguously quantified with this approach. This limits the application of 1D MRS to identify potential biomarkers of AD. For unambiguous characterization of the neurochemical profile in transgenic AD mouse brains, we have applied *in vivo* localized 2D MRS. Figures 5.2a and 5.2b show characteristic 2D MR spectra obtained from a 27  $\mu$ l voxel placed in the cingulate cortex and covering some parts of the hippocampus (Fig. 5.1a) of an 18 month old control and a transgenic mouse, respectively. Both spectra are scaled and plotted with the same absolute contour levels. As has been shown in Chapter 4, 2D MRS in mouse brain at high magnetic field allows separation of most overlapping signals for the coupled spin systems that gave rise to off-diagonal peaks. As a result, a wider range of neurochemicals can be detected in a 2D MR spectrum compared to a 1D spectrum obtained from the same volume.

The 2D metabolite ratios and the raw volume integrals of the signals on the diagonal and of the cross peaks in data collected from the mouse brain were very well reproduced, and the variation of the 2D peak volumes between individuals was sufficiently small to allow for the reliable detection of differences between normal and AD mice. In line with the 1D spectra, an increase in the intensity of cross peaks of taurine, and reduced intensities of the cross peaks of glutamate and NAA were observed in the transgenic mice relative to controls. In addition, a decrease in the concentration of glutathione was observed. Interestingly, the cross-peaks labeled as U2 and U3 which could not be assigned to any of the 35 known brain metabolites in control mouse brain were absent in transgenic mouse brain (see also chapter 4). On the other hand, two unknown cross-peaks labeled as U4 and U5, were present only in transgenic mouse brain and not in controls. Although further studies would be needed to assign these resonances to new metabolites or macromolecules present in the cortex-hippocampus region of the control or transgenic mouse brain, their presence or absence in the transgenic brain may indicate a potential role as marker for AD.

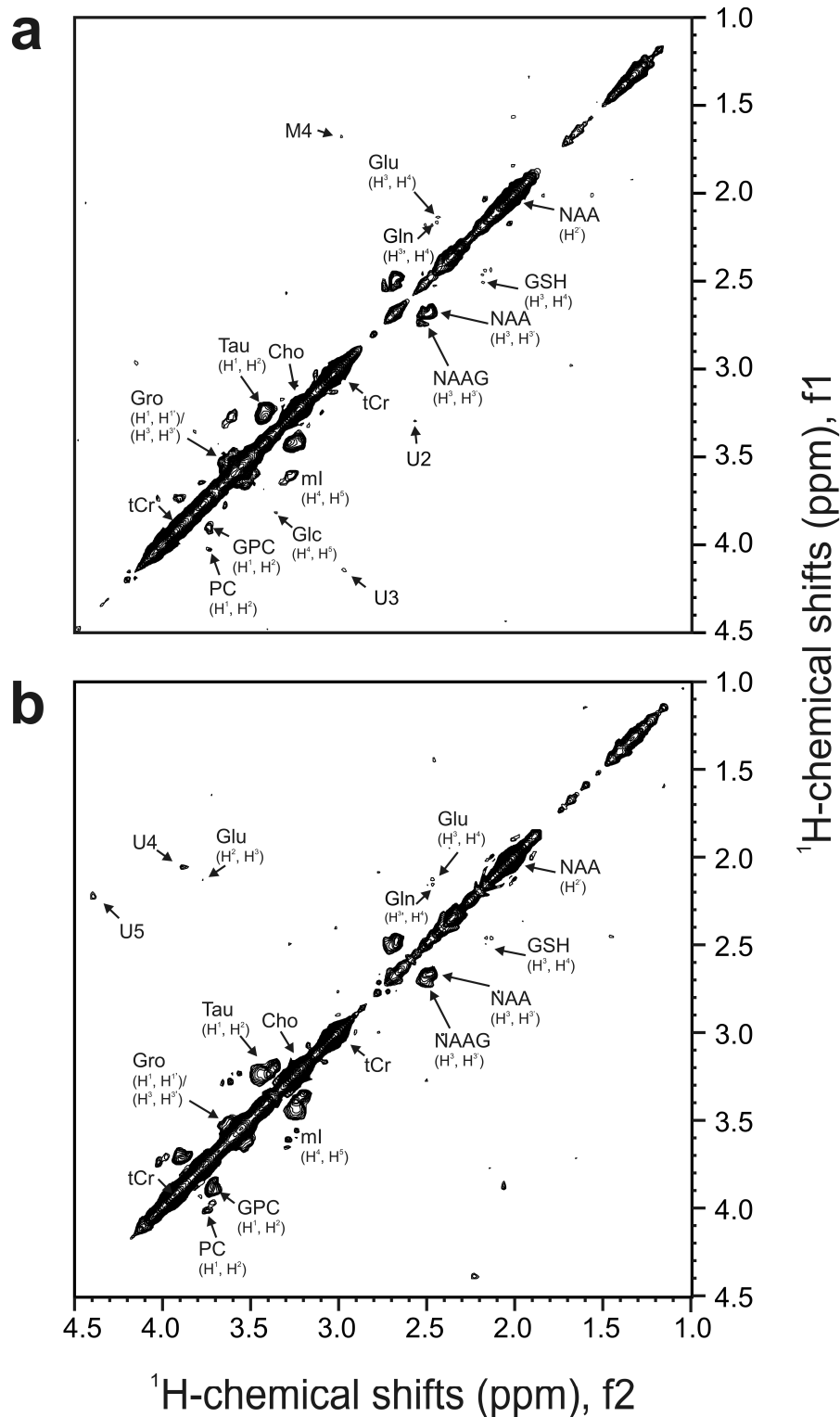


Figure 5.2: Two dimensional in vivo localized MR spectra obtained from a  $27 \mu\text{l}$  ( $1.7 \times 4 \times 4 \text{ mm}^3$ ) voxel covering the cortex-hippocampus region of the brain of an 18 month old control (a) and AD (b) mouse. Spectra were obtained using the PRESS based 2D L-COSY sequence at 9.4T with  $TR=1500 \text{ ms}$  and  $TE=15 \text{ ms}$ . The 2D data set was apodized with a QSINE function and zero filled to 1024 in both dimensions. U2, U3, U4 and U5 are unassigned cross-peaks (see also Chapter 4). The peak M4 arises from macromolecules and is labeled in accordance with Behar and Ogino (27).

A diagonal peak at 3.2 ppm arises from methyl protons of choline-containing compounds. This signal contains contribution from free choline, GPC and PC. Since the concentration of choline in brain is well below the NMR detection limit, the total choline response at 3.2 ppm arises mainly from GPC and PC. Due to the very small difference in chemical shifts, PC and GPC cannot be separated in 1D  $^1\text{H}$ -MRS. Separation could in principle be achieved through smaller resonances from the methylene proton in the region between 3.6 and 3.9 ppm. However, due to the strongly coupled spin system these resonances are difficult to separate from the resonances of other metabolites in the same region in 1D MRS. As shown in Fig. 5.2, the cross-peaks of GPC were clearly separated in the 2D MR spectrum. When the concentration of GPC in the transgenic mice was compared with control mice, GPC levels were strongly (~75%) and significantly ( $P < 0.01$ ) increased in AD mice. This observation is similar to what has been observed by HPLC in CSF samples of human AD patients and post-mortem  $^{31}\text{P}$  MRS studies of human AD brain extracts (10,28-30). It has been proposed that an increase in GPC during AD may be linked to the increased breakdown of membrane phospholipids, such as phosphatidylcholine, during progression of neurodegeneration due to the activation of calcium dependent phospholipase  $A_2$  (29). This inference is supported by a previous study, which revealed that phospholipase  $A_2$  is responsible for NMDA-induced formation of GPC in rat hippocampal slices (31). It is also supported by the detection of elevated cPLA $_2$  immunoreactivity in AD brain (32). In addition, amyloid peptide *in vitro* induces direct activation of cPLA $_2$  as well as direct release of cellular choline (33). Other studies have shown that GPC promotes amyloid aggregation (34,35). A putative chain of events to explain an increase in the level of GPC in AD brain and its relationship with soluble A $\beta$  and A $\beta$  plaques is shown in Fig. 5.3. In this cascade of events, soluble A $\beta$  protein produced during abnormal cleavage of APP is likely to be the initiating factor in the disease cascade. Increased levels of A $\beta$  can cause an influx of calcium in neuronal cells, leading to calcium overload. This subsequently activates calcium dependent phospholipase  $A_2$ , which breaks down PtdCho, which ultimately leads to an elevation in the level of GPC and other breakdown products (29). Under normal conditions GPC is unable to leave the cell. However, as the cell becomes leaky due to membrane breakdown, GPC can be released into the extracellular fluid and the CSF. This extracellular GPC can subsequently enhance A $\beta$  aggregation leading to plaque deposition (29,33-35). In addition, a defective membrane metabolism could expose APP to abnormal proteolytic cleavage (28) leading to an increase in toxic soluble A $\beta$  peptide which can disrupt normal membrane phospholipid turnover (Fig. 5.3).

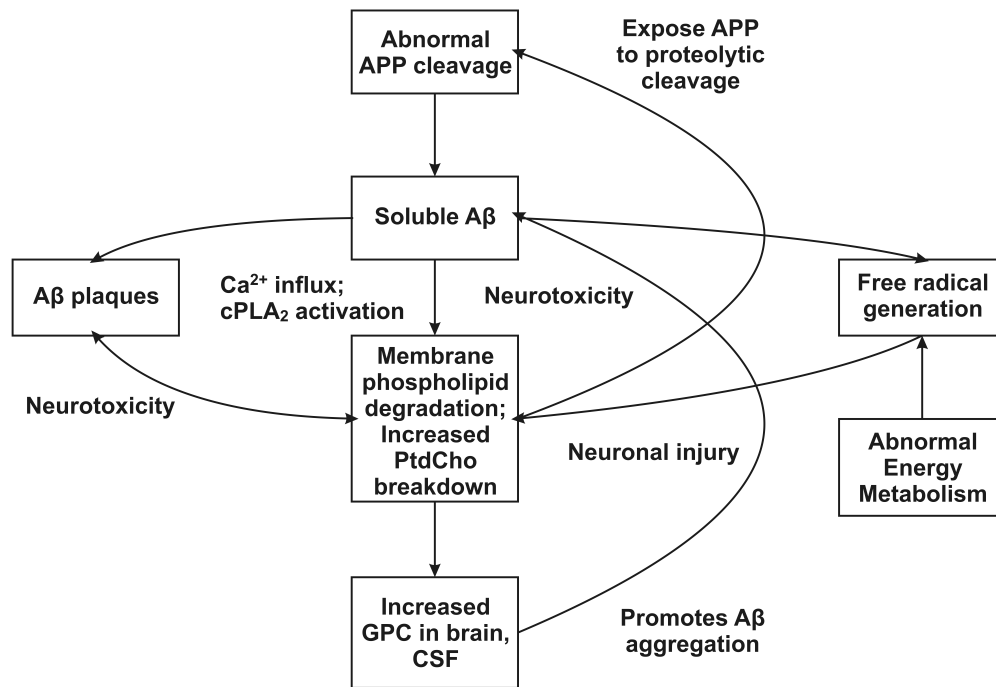


Figure 5.3: Simplified disease pathways of AD, illustrating the interactions of both soluble and aggregated A $\beta$  with membrane phospholipids. As a result of these interactions, GPC levels increase. Increasing GPC levels may account for the observed increase in plaque deposition, or vice versa.

The exact sequential relationship between amyloid aggregation and membrane breakdown during AD progression *in vivo* is not yet known. To investigate the temporal relation between plaque formation and changes in GPC during AD progression, we simultaneously tracked plaque deposition and the changes in GPC levels in the same transgenic AD mice with age using longitudinal *in vivo*  $\mu$ MRI and 2D MRS. Fig. 5.4 (upper panel), shows representative MR images of the same transgenic AD mouse which was imaged at 12, 16, 18, 20 and 22 months of age. A consistent increase in plaque-load was observed with age. This increase in plaque-load correlated well with an increase in GPC levels until 18 months of age (Fig. 5.4; lower panel). Interestingly, a very rapid decline in GPC was observed at the age of 20 months. Figure 5.5a shows the changes in GPC level in control and transgenic mice at ages between 8 and 22 months detected by 2D MRS. The level of GPC in the cortex/hippocampus region of control and AD mice was similar up to 12 months of age (Fig. 5.5a). Consequently an increase is observed in the transgenic mice up to 18 months of age, with levels in control mice being consistently lower (Fig. 5.5a). At the 20th month of age, GPC levels in transgenic mice apparently drop to resemble the levels found for control mice. Quantification of A $\beta$  plaque-load in AD mice with age is shown in Fig. 5.5b. A marked age-related increase in both plaque-load and numerical density of A $\beta$  plaques is evident in this figure.

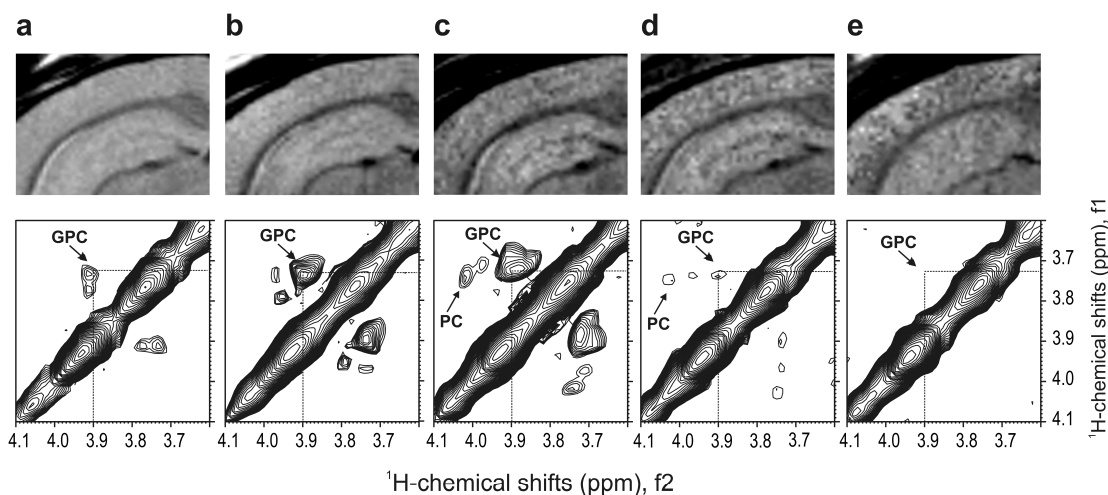


Figure 5.4: Correlation between the development of  $A\beta$  plaques visualized by  $\mu$ MRI (upper panel) and the changes in the levels of glycerophosphocholine monitored by 2D MRS (lower panel) in the cortex-hippocampus region of the same AD mouse brain with age.  $A\beta$  plaques were visualized in the same transgenic mouse (Tg2576) at the ages of 12 months (a), 16 months (b), 18 months (c), 20 months (d), and 22 months. The MR images were obtained using a RARE sequence, with an in-plane resolution of  $78 \mu\text{m} \times 78 \mu\text{m}$ ,  $TE = 10.567 \text{ ms}$ ,  $TR = 6 \text{ s}$ , echo train length = 4, averages = 4 and a total scan time of  $\sim 25 \text{ min}$ . Concurrently with the visualization of  $A\beta$  development, 2D spectra were obtained using the L-COSY sequence in the same mice at the ages of 12 months (a), 16 months (b), 18 months (c), 20 months (d), and 22 months.

A comparison of the GPC levels with plaque-load at different time points shows that GPC levels remain unchanged until 12 months of age, when plaques were also not detected. Subsequently a marked age-related increase in both plaque-load and GPC level was observed between 14 and 18 months (Fig. 5.5). These results advocate a direct correlation between the severity of  $A\beta$  deposition and the increase in GPC levels in AD brain. In contrast to the cortex-hippocampus region, the thalamus region does not show significant  $A\beta$  deposition, while the GPC levels remain the same (data not shown). This provides additional support for a direct correlation between GPC levels and  $A\beta$  deposition. The reason for the sudden decline in the GPC level beyond 20 months of age is not clear (Fig. 5.4 and 5.5). It is possible that significant neuronal membrane impairment up to this age results in GPC leaving the cells and being released into the extracellular fluid and CSF, which leads to a decline of GPC in the affected brain regions. This assumption is supported by the observation of an increase in GPC levels in CSF during AD in a previous study (29). Alternatively, down-regulation of the membrane phospholipid turnover may be responsible for the decline in GPC.

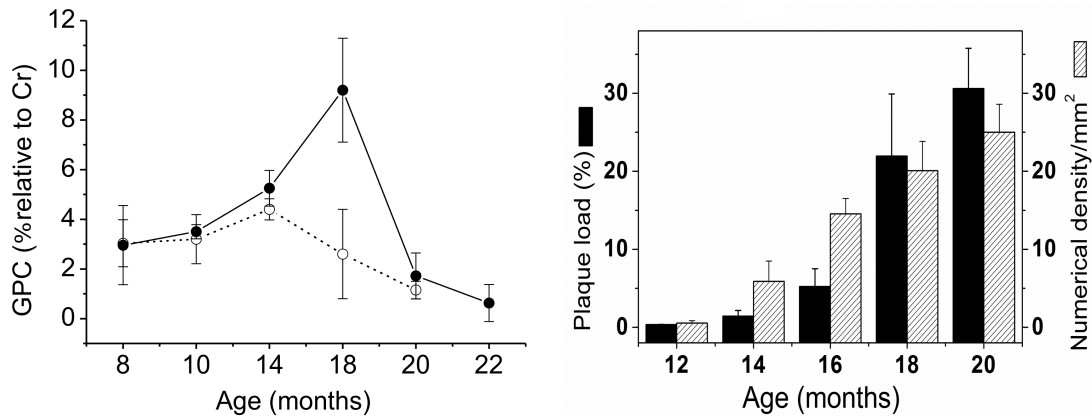


Figure 5.5: Age-dependent changes in A $\beta$  plaque-load and numerical density of A $\beta$  lesions in the cortex-hippocampus region of transgenic mice detected by  $\mu$ MRI are shown in the right panel, while GPC levels in the cortex-hippocampus region of AD mice (●) and control mice (○) detected by 2D MRS are shown in the left panel. Data represent the mean of  $n=5$  ( $\pm$ SD). The GPC levels were estimated from localized 2D datasets collected at the age of 8, 10, 14, 18, 20 and 22 months. Plaque-load and numerical density of plaques was calculated from the  $\mu$ MR images at the age of 12, 14, 16, 18 and 20 months.

In summary, the present study demonstrates that localized 2D MRS in combination with  $\mu$ MRI provides a powerful non-invasive method to follow the correlation between age-dependent neurochemical changes and plaque deposition in AD transgenic mice. Due to the non-invasive and repeatable nature, these methods can substantially accelerate drug discovery. Based on the results from this study, it can be concluded that elevated GPC levels correlate well with AD progression and GPC can be a useful *in vivo* biomarker of AD. Further experimental studies are needed to identify the large number of unassigned resonances detected on 2D MRS spectra, as these may be relevant to pathophysiological conditions during AD.

## Acknowledgements

The authors wish to thank dr. M.A. Thomas for useful discussion and suggestions, dr. S. Provencher for a useful discussion regarding the use of the LCmodel analysis software, and dr. M. Marjanska for providing an extended LCModel basis set for analysis of the 1D spectra, and E. Daviso, for his assistance with the Sparky analysis software. This research project was supported in part by funds from Internationale Stichting Alzheimer Onderzoek (ISAO), CYTTRON within the Bsik program (Besluit subsidies investeringen kennisinfrastructuur) and the Centre for Medical Systems Biology (CMSB).



## References

1. Braak H, Braak E. Diagnostic criteria for neuropathologic assessment of Alzheimer's disease. *Neurobiol Aging* 1997;18:S85-S88.
2. Dedeoglu A, Choi JK, Cormier K, Kowall NW, Jenkins BG. Magnetic resonance spectroscopic analysis of Alzheimer's disease mouse brain that express mutant human APP shows altered neurochemical profile. *Brain Res* 2004;1012:60-65.
3. Marjanska M, Curran GL, Wengenack TM, Henry PG, Bliss RL, Poduslo JF, Jack CR, Ugurbil K, Garwood M. Monitoring disease progression in transgenic mouse models of Alzheimer's disease with proton magnetic resonance spectroscopy. *Proc Natl Acad Sci U S A* 2005;102:11906-11910.
4. von Kienlin M, Kunnecke B, Metzger F, Steiner G, Richards JG, Ozmen L, Jacobsen H, Loetscher H. Altered metabolic profile in the frontal cortex of PS2APP transgenic mice, monitored throughout their life span. *Neurobiol Dis* 2005;18:32-39.
5. Kantarci K, Jack CR, Xu YC, Campeau NG, O'Brien PC, Smith GE, Ivnik RJ, Boeve BF, Kokmen E, Tangalos EG, Petersen RC. Regional metabolic patterns in mild cognitive impairment and Alzheimer's disease - A H-1 MRS study. *Neurology* 2000;55:210-217.
6. Jessen F, Block W, Traber F, Keller E, Flacke S, Papassotiropoulos A, Lamerichs R, Heun R, Schild HH. Proton MR spectroscopy detects a relative decrease of N-acetylaspartate in the medial temporal lobe of patients with AD. *Neurology* 2000;55:684-688.
7. Klunk WE, Xu C, Panchalingam K, McClure RJ, Pettegrew JW. Quantitative H-1 and P-31 MRS of PCA extracts of postmortem Alzheimer's disease brain. *Neurobiol Aging* 1996;17:349-357.
8. Mohanakrishnan P, Fowler AH, Vonsattel JP, Husain MM, Jolles PR, Liem P, Komoroski RA. An In-Vitro H-1 Nuclear-Magnetic-Resonance Study Of The Temporoparietal Cortex Of Alzheimer Brains. *Exp Brain Res* 1995;102:503-510.
9. Pettegrew JW, Klunk WE, Panchalingam K, McClure RJ, Stanley JA. Magnetic resonance spectroscopic changes in Alzheimer's disease. In: *Cerebrovascular Pathology In Alzheimer's Disease*. New York: New York Acad Sciences, 1997; 282-306.
10. Pettegrew JW, Panchalingam K, Moosy J, Martinez J, Rao G, Boller F. Correlation Of P-31 Magnetic-Resonance Spectroscopy And Morphologic Findings In Alzheimers-Disease. *Arch Neurol* 1988;45:1093-1096.

11. Tsang TA, Woodman B, McLoughlin GA, Griffin JL, Tabrizi SJ, Bates GP, Holmes E. Metabolic characterization of the R6/2 transgenic mouse model of Huntington's disease by high-resolution MAS H-1 NMR spectroscopy. *J Proteome Res* 2006;5:483-492.
12. van Dellen A, Welch J, Dixon RM, Cordery P, York D, Styles P, Blakemore C, Hannan AJ. N-acetylaspartate and DARPP-32 levels decrease in the corpus striatum of Huntington's disease mice. *Neuroreport* 2000;11:3751-3757.
13. Jenkins BG, Brouillet E, Chen YCI, Storey E, Schulz JB, Kirschner P, Beal MF, Rosen BR. Non-invasive neurochemical analysis of focus excitotoxic lesions in models of neurodegenerative illness using spectroscopic imaging. *J Cereb Blood Flow Metab* 1996;16:450-461.
14. Boska MD, Lewis TB, Destache CJ, Benner EJ, Nelson JA, Uberti M, Mosley RL, Gendelman HE. Quantitative H-1 magnetic resonance spectroscopic imaging determines therapeutic immunization efficacy in an animal model of Parkinson's disease. *J Neurosci* 2005;25:1691-1700.
15. Choi JK, Dedeoglu A, Jenkins BG. Application of MRS to mouse models of neurodegenerative illness. *NMR Biomed* 2007;20:216-237.
16. Pioro EP, Majors AW, Mitsumoto H, Ng TC. Proton magnetic resonance spectroscopic imaging reveals in vivo evidence of neurodegeneration and elevated glutamate in the medulla of patients with ALS. *Neurology* 1998;50:A315-A315.
17. Pioro EP, Wang Y, Moore JK, Ng TC, Trapp BD, Klinkosz B, Mitsumoto H. Neuronal pathology in the wobbler mouse brain revealed by in vivo proton magnetic resonance spectroscopy and immunocytochemistry. *Neuroreport* 1998;9:3041-3046.
18. Thomas MA, Yue K, Binesh N, Davanzo P, Kumar A, Siegel B, Frye M, Curran J, Lufkin R, Martin P, Guze B. Localized two-dimensional shift correlated MR spectroscopy of human brain. *Magn Reson Med* 2001;46:58-67.
19. Hsiao K, Chapman P, Nilsen S, Eckman C, Harigaya Y, Younkin S, Yang FS, Cole G. Correlative memory deficits, A beta elevation, and amyloid plaques in transgenic mice. *Science* 1996;274:99-102.
20. Hennig J, Nauerth A, Friedburg H. Rare Imaging - A Fast Imaging Method For Clinical Mr. *Magn Reson Med* 1986;3:823-833.
21. Bottomley PA. Spatial Localization In NMR Spectroscopy In vivo. *Ann N Y Acad Sci* 1987;508:333-348.
22. Mandal PK. Magnetic resonance spectroscopy (MRS) and its application in Alzheimer's disease. *Concepts In Magnetic Resonance Part A* 2007;30A:40-64.

23. Tkac I, Starcuk Z, Choi IY, Gruetter R. In vivo  $^1\text{H}$  NMR spectroscopy of rat brain at 1 ms echo time. *Magn Reson Med* 1999;41:649-656.
24. Govindaraju V, Young K, Maudsley AA. Proton NMR chemical shifts and coupling constants for brain metabolites. *NMR Biomed* 2000;13:129-153.
25. van Balen R, Koelma D, Ten Kate TK, Mosterd B, Smeulders AWM. SCIL Image: a multi-layered environment for use and development of image processing software. In: *Experimental environments for computer vision and image processing*. Singapore: World Scientific Computing Co. Pte. Ltd., 1994; 107-126.
26. Provencher SW. Estimation Of Metabolite Concentrations From Localized In-Vivo Proton Nmr-Spectra. *Magn Reson Med* 1993;30:672-679.
27. Behar KL, Ogino T. Characterization Of Macromolecule Resonances In The H-1-Nmr Spectrum Of Rat-Brain. *Magnetic Resonance In Medicine* 1993;30:38-44.
28. Nitsch RM, Blusztajn JK, Pittas AG, Slack BE, Growdon JH, Wurtman RJ. Evidence For A Membrane Defect In Alzheimer-Disease Brain. *Proc Natl Acad Sci U S A* 1992;89:1671-1675.
29. Walter A, Korth U, Hilgert M, Hartmann J, Weichel O, Hilgert M, Fassbender K, Schmitt A, Klein J. Glycerophosphocholine is elevated in cerebrospinal fluid of Alzheimer patients. *Neurobiol Aging* 2004;25:1299-1303.
30. Pettegrew JW, Moosy J, Withers G, McKeag D, Panchalingam K. P-31 Nuclear Magnetic-Resonance Study Of The Brain In Alzheimers-Disease. *J Neuropathol Exp Neurol* 1988;47:235-248.
31. Weichel O, Hilgert M, Chatterjee S, Lehr M, Klein J. Bilobalide, a constituent of Ginkgo biloba, inhibits NMDA-induced phospholipase A(2) activation and phospholipid breakdown in rat hippocampus. *Naunyn-Schmiedebergs Arch Pharmacol* 1999;360:609-615.
32. Stephenson DT, Lemere CA, Selkoe DJ, Clemens JA. Cytosolic phospholipase A(2) (cPLA(2)) immunoreactivity is elevated in Alzheimer's disease brain. *Neurobiol Dis* 1996;3:51-63.
33. Allen DD, Galdzicki Z, Brining SK, Fukuyama R, Rapoport SI, Smith QR. Beta-amyloid induced increase in choline flux across PC12 cell membranes. *Neurosci Lett* 1997;234:71-73.
34. Klunk WE, Xu CJ, McClure RJ, Panchalingam K, Stanley JA, Pettegrew JW. Aggregation of beta-amyloid peptide is promoted by membrane phospholipid metabolites elevated in Alzheimer's disease brain. *J Neurochem* 1997;69:266-272.

35. Mandal PK, McClure RJ, Pettegrew JW. Interactions of A beta(1-40) with glycerophosphocholine and intact erythrocyte membranes: Fluorescence and circular dichroism studies. *Neurochem Res* 2004;29:2273-2279.



# 6 General discussion and future outlook\*

---

In this thesis the potential applications of high resolution MR microimaging and spectroscopy to study Alzheimer's disease pathology in transgenic mouse models were explored. The focus was both on the  $\mu$ MRI and the 2D MRS method optimization, as well as their application to visualize and understand the mechanism of AD pathology *in vivo*.

## 6.1 Visualization of AD hallmarks: amyloid plaques and beyond

The visualization of A $\beta$  plaque deposition in brain, a key feature of Alzheimer's disease, is important for the evaluation of disease progression and the efficacy of therapeutic interventions. In Chapter 3, it was shown that application of the RARE sequence at 9.4T allowed plaques visualization without contrast agents in a scan time as short as 25 min with an in-plane resolution of 78  $\mu$ m. The straightforward implementation of a  $T_2$ -weighted RARE sequence combined with high magnetic field strength provided sufficient resolution for clearly visualizing plaques in living mouse brain.

The basis for intrinsic MRI contrast between individual plaques and normal background tissue is not fully understood. It is presumed that the hydrophobic nature of amyloid deposits, or age related accumulation of iron within the plaques, can have an effect on the  $T_2$  and  $T_2^*$  relaxation rates in and adjacent to plaques (1,2). Very recently, El Tannir El Tayara *et al.* (2) have shown that  $T_2$  relaxation can be affected by plaque deposition in the absence of histochemically detectable iron. House *et al.* (3) found no correlation between AD plaque density and iron concentration. The distribution of iron in the histological sections of the Tg2576 mouse brain was examined in Chapter 3. Iron was found to be associated with many dense-cored senile plaques, though not all contained iron. This suggests that the intrinsic MR contrast from A $\beta$  plaques may be partly caused by iron, although signal hypointensities arising from the reduced water content in A $\beta$  plaques compared to the surrounding tissue and from other unknown factors cannot be ruled out. Amyloid plaques in AD brains can be circumscript plaques with a dense core or more diffuse plaques. Dense-core plaques are fibrillar deposits of A $\beta$ , showing all the classical properties of amyloid including  $\beta$ -sheet secondary structure, while diffuse plaques are amorphous deposits of A $\beta$  that lack a core (4). It is still an open question if iron is

---

\*Parts of this chapter were submitted to Curr Med Imaging Rev

associated with dense cored plaques, diffuse core plaques, or both. In addition, it is not yet clear if MRI techniques for the visualization of amyloid plaques are more specifically detecting dense core plaques or diffuse plaques. This aspect warrants further research efforts. It will require the improvement of resolution and specificity of available MRI techniques to distinguish between dense-core and diffuse plaques.

In Chapter 3 it was shown that  $\mu$ MRI can be successfully used for longitudinal studies monitoring the development of A $\beta$  plaques with age in the same animals. The same Tg2576 mice were imaged at regular intervals, which showed a marked age-dependent increase in amyloid deposition in the hippocampus and cortex. This longitudinal study has shown that, using  $\mu$ MRI, a genuine map of plaque deposition can be made as the disease progresses in a living subject. Such a map may subsequently be used to assess the efficacy of putative AD treatment strategies. In addition, using this approach interesting biological issues could be non-invasively addressed; for example, does a particular therapeutic approach arrest plaque growth, shrink plaques, or prevent development of new plaques? Is the effect of a therapeutic a uniform response of all plaques, or are there significant plaque to plaque variations?

Further improvements will be required in the field of MR based amyloid imaging, such as higher specificity of plaque detection, improved resolution of MR images, and a reduction of the required measurement time. Specificity may be increased by the development of safe MR contrast agents that cross the blood-brain barrier and selectively bind A $\beta$  plaques. Improved resolution and reduced measurement times may be achieved by exploiting the improved SNR granted by high magnetic fields. For studies in mice, moving from 9.4T to 17.6T will be beneficial. Very recently Faber *et al.* published the first ultra-high field (17.6T) study of *in vivo* plaque visualization in transgenic AD mice (5). Due to the increased field strength, and the corresponding increase in SNR, it was possible to visualize plaques *in vivo* in the thalamus region with an isotropic resolution of 94 $\times$ 94 $\times$ 94  $\mu$ m in 34 minutes. The high magnetic field strength also permitted *in vivo* detection of plaques with a lower resolution of 94 $\times$ 234 $\times$ 234  $\mu$ m in a scan time of only 82 seconds using a gradient echo sequence. At high magnetic field strength, the dipole field of iron in the plaques causes strong signal dephasing in a region larger than the actual size of a plaque, which facilitates detection. Short scan times provide new opportunities for MR in Alzheimer research. For example, rapid scan protocols could be used for high throughput screening of a large number of AD transgenic mice treated with new drugs. However, *in vivo* visualization of plaques in the cortex and hippocampus, which are the most affected areas in human AD patients, has not yet been successful at high field.

For increased specificity in amyloid detection, ultimately molecular imaging will be the method of choice. This approach requires the administering of a suitable contrast agent. Thus far, contrast agent based MR approaches for *in vivo* plaque visualization in transgenic mice have been used in only two studies. The first reported study was by Wadghiri *et al.* in 2003 (6). Relying on the observation that the A $\beta$  peptide avidly binds to amyloid plaques, they developed an effective MRI sensitive plaque ligand by attaching either gadolinium or iron nanoparticles to A $\beta$ . Although the results of this study were convincing, the ligand does not spontaneously pass through the blood-brain barrier, and co-administration of mannitol was required for the ligand to gain access to the brain. Due to the neurotoxicity of A $\beta$  and the requirement for mannitol injection, these methods may have limited utility in longitudinal studies in mice. A subsequent study was reported by Higuchi *et al.* in 2005 (7). They used Congo Red-based amyloidophilic compounds that were labeled with  $^{19}\text{F}$ . The authors showed that when this ligand is injected intravenously into living transgenic mice, it successfully crosses the blood-brain barrier and binds amyloid plaques, which can subsequently be detected with  $^{19}\text{F}$ -MRI. They proposed that this approach can be used for longitudinal studies in mouse models of AD (7). It is interesting to note that  $^{19}\text{F}$ -containing ligands are not specific to only amyloid plaques, as they can bind neurofibrillary tangles and perhaps even Lewy bodies or other  $\beta$ -sheet inclusions as well (7). Sensitivity of ligands to both amyloid plaques and neurofibrillary tangles may be diagnostically relevant, since both are histological hallmarks of AD. Prospective contrast agents for visualizing and quantifying the pathologic burden of  $\beta$ -amyloid plaque should be highly stable *in vivo*, cross the blood-brain barrier non-destructively following intravenous injection, bind specifically to plaques with high affinity, produce local changes in tissue contrast detectable by MRI, and require lower dosages than current contrast agents (8,9).

## 6.2 2D MRS applications in AD

In Chapter 4, it was shown that the application of localized 2D MRS in mouse brain is possible, and that a large number of metabolites can be uniquely and reproducibly detected using 2D methods. Subsequently, in Chapter 5, the L-COSY method was applied to study the effects of AD on the neurochemical profile of aging Tg2576 mice. Specifically, it was found that the membrane phospholipid breakdown product GPC increases concurrently with the increasing plaque-load in aging Tg2576 mice. Unlike 1D MRS techniques, localized 2D MRS had not been reported in mouse brain until now, and resolving strongly overlapping signals from different metabolites required the use of



spectral editing techniques (10,11) or the application of spectral analysis software such as LCmodel (12). The drawback of spectral editing is that only a single metabolite of interest is targeted per measurement, and for current analysis software, only metabolites in the analysis database are measured. As seen in Chapters 4 and 5, 2D MRS provides a method whereby metabolites overlapping in 1D may be distinguished and uniquely assigned. As described in Chapter 5, glycerophosphocholine appears to be a potential biomarker for the onset and progression of AD. The *in vivo* changes in GPC levels in mice should be monitored in other AD mouse models as well. In addition, changes in GPC levels in human brain may be determined by implementation of 2D MRS on high field ( $\geq 7\text{T}$ ) clinical scanners.

As with MR imaging, several advantages are expected in MR spectroscopy when moving to high magnetic field (13,14). Spectroscopy at high field strengths is enhanced by the increase in SNR and by improved spatial resolution. Finally, increased spectral dispersion will provide more reliable quantification and additional sensitivity gains (13). I made some initial efforts to implement MRS on a Bruker 17.6T (750MHz) vertical bore system fitted with 1T/m gradients, and a 20mm birdcage volume transmit/receive coil. Measurements in a brain phantom yielded a linewidth of  $\sim 7$  Hz, or 0.0175 ppm, at 9.4T. At 17.6T, the linewidth obtained from the same sample, with the same scan settings, was  $\sim 10$  Hz, or 0.0133 ppm, which is an improvement of approximately 30%. With further optimization of the scan parameters a greater improvement may be obtained. These preliminary findings are hopeful for future 2D MRS experiments at 17.6T, although further optimization is still required. Thus far MRS at 17.6T has only been tested successfully in phantom solutions. It is expected that the NMR lines in brain or other inhomogeneous samples will be broader than in the phantom. In addition, tissue-inhomogeneity induced susceptibility effects due to the increasing field strength may cause an additional increase in linewidth (15). As reported by Fleysner *et al.* (15), first and second order shimming may not be sufficient to compensate for this effect. Reducing the voxel size can help to limit the linebroadening due to tissue-inhomogeneity (15). It is expected that these limitations may be less relevant for small animal scanners than for clinical scanners; shimming and gradient systems for small-animal scanners are considerably stronger than systems available on clinical scanners, and allow manual shimming of first, second, and higher order shims, in addition to automatic shimming of the first and second order shims. Efforts to further optimize one- and two-dimensional MRS at 17.6T may thus prove beneficial to the future study of AD.

### 6.3 Potential challenges for the translation to humans

As the field strengths of clinical scanners are approaching those of small-animal scanners, while A $\beta$  plaques in mice and humans are quite similar in size, from 20 up to 200  $\mu\text{m}$  (16), the exciting question is obvious: Can amyloid plaques be detected *in vivo* in man using MRI sequences that can be realistically applied in a clinical setting? In principle, the *ex vivo* MRI studies in post-mortem human tissue (1,17) and *in vivo* studies in mice (5-7,18-22) have set the stage for further technical innovation to extend amyloid imaging to living human subjects. However, several practical hurdles remain before this can be achieved. Despite the long imaging times and the use of very high field MR systems for plaque visualization in mice, MRI is a relatively insensitive technique. This suggests that MRI hardware and software need further improvement in terms of sensitivity to obtain sufficient contrast-to-noise ratios and resolution in humans in a much shorter imaging time. The optimization of MRI protocols for plaque detection will be difficult due to the uncertainty of the presence of amyloid plaques in suspected Alzheimer patients. Movement artifacts are likely to be a problem; in animal studies, the subjects are anaesthetized during measurement. This cannot be done in human studies. Consequently, patients remain conscious and are required to remain immobile. This may not be a problem for early detection of plaques in patients that do not yet have disease symptoms; however, it may be difficult for patients with advanced Alzheimer's disease to keep still even with a scan duration of only a few minutes. In addition, the specificity of the technique needs to be improved to differentiate A $\beta$  plaques from other structures with a similar appearance on MRI, such as blood vessels and small hemorrhages. Specificity may be increased by the development of safe MR contrast agents that cross the blood-brain barrier and selectively bind and enhance A $\beta$  plaques in MRI. The required doses of contrast agents must be decreased. Currently, PET-based ligands can be administered in the picomolar range or less, whereas MRI-based ligands need to be administered in the micromolar range (8).

With the advent of ultra-high field ( $\geq 7\text{T}$ ) MR in clinical settings, high resolution one- and two-dimensional MRS in humans is becoming feasible as well. As demonstrated previously by Thomas *et al.* (23), an increase in field strength from 1.5 to 3T is beneficial for the reliable detection of metabolites using 2D MRS. A further increase in field strength, from 3T to 7T, is expected to yield similar improvements in spectral dispersion. Keeping in mind the limitations set forth by Fleysher *et al.* (15), who noted that as  $B_0$  rises, the consequent increase in linewidths counteracts the chemical shift dispersion and leads to the overlap of the components of  $J$ -coupled multiplets (24), the voxel size may

need to be reduced to prevent an increased linewidth due to macroscopic inhomogeneity (15). While localized two-dimensional MRS has yet to be applied in high field clinical scanners, several groups have already successfully applied conventional 1D MRS using 7T clinical scanners, and reported a significant improvement in results compared to studies at lower fields (25,26).

## References

1. Benveniste H, Einstein G, Kim KR, Hulette C, Johnson A. Detection of neuritic plaques in Alzheimer's disease by magnetic resonance microscopy. *Proc Natl Acad Sci U S A* 1999;96:14079-14084.
2. El Tayara NET, Volk A, Dhenain M, Delatour B. Transverse relaxation time reflects brain amyloidosis in young APP/PS1 transgenic mice. *Magn Reson Med* 2007;58:179-184.
3. House MJ, Pierre TGS, Kowdley KV, Montine T, Connor J, Beard J, Berger J, Siddaiah N, Shankland E, Jin LW. Correlation of proton transverse relaxation rates (R2) with iron concentrations in postmortem brain tissue from Alzheimer's disease patients. *Magn Reson Med* 2007;57:172-180.
4. Rak M, Del Bigio MR, Mai S, Westaway D, Gough K. Dense-core and diffuse A beta plaques in TgCRND8 mice studied with synchrotron FTIR microspectroscopy. *Biopolymers* 2007;87:207-217.
5. Faber C, Zahneisen B, Tippmann F, Schroeder A, Fahrenholz F. Gradient-echo and CRAZED imaging for minute detection of Alzheimer plaques in an APP(V717I) x ADAM10-dn mouse model. *Magn Reson Med* 2007;57:696-703.
6. Wadghiri YZ, Sigurdsson EM, Sadowski M, Elliott JI, Li YS, Scholtzova H, Tang CY, Aguinaldo G, Pappolla M, Duff K, Wisniewski T, Turnbull DH. Detection of Alzheimer's amyloid in Transgenic mice using magnetic resonance microimaging. *Magn Reson Med* 2003;50:293-302.
7. Higuchi M, Iwata N, Matsuba Y, Sato K, Sasamoto K, Saido TC. <sup>19</sup>F and <sup>1</sup>H MRI detection of amyloid beta plaques in vivo. *Nat Neurosci* 2005;8:527-533.
8. Huddleston DE, Small SA. Technology Insight: imaging amyloid plaques in the living brain with positron emission tomography and MRI. *Nat Clin Pract Neurol* 2005;1:96-105.

9. Poduslo JF, Wengenack TM, Curran GL, Wisniewski T, Sigurdsson EM, Macura SI, Borowski BJ, Jack CR. Molecular targeting of Alzheimer's amyloid plaques for contrast-enhanced magnetic resonance imaging. *Neurobiol Dis* 2002;11:315-329.
10. Rothman DL, Petroff OAC, Behar KL, Mattson RH. Localized H-1-Nmr Measurements Of Gamma-Aminobutyric-Acid In Human Brain Invivo. *Proc Natl Acad Sci U S A* 1993;90:5662-5666.
11. de Graaf RA, Dijkhuizen RM, Biessels GJ, Braun KPJ, Nicolay K. In vivo glucose detection by homonuclear spectral editing. *Magn Reson Med* 2000;43:621-626.
12. Provencher SW. Estimation Of Metabolite Concentrations From Localized In-Vivo Proton Nmr-Spectra. *Magn Reson Med* 1993;30:672-679.
13. Helpert JA. The promise of high-field-strength MR imaging. *Am J Neuroradio* 2003;24:1738-1739.
14. Gonen O. Higher field strength for proton MR spectroscopy. *Am J Neuroradio* 2003;24:783-784.
15. Fleysher R, Fleysher L, Liu S, Gonen O. On the voxel size and magnetic field strength dependence of spectral resolution in magnetic resonance spectroscopy. *Magn Reson Imaging* 2008; In Press.
16. Lehericy S, Marjanska M, Mesrob L, Sarazin M, Kinkingnehun S. Magnetic resonance imaging of Alzheimer's disease. *European Radiology* 2007;17:347-362.
17. Dhenain M, Privat N, Duyckaerts C, Jacobs RE. Senile plaques do not induce susceptibility effects in T<sub>2</sub>\*-weighted MR microscopic images. *NMR Biomed* 2002;15:197-203.
18. Borthakur A, Gur T, Wheaton AJ, Corbo M, Trojanowski JQ, Lee VMY, Reddy R. In vivo measurement of plaque burden in a mouse model of Alzheimer's disease. *J Magn Reson Imaging* 2006;24:1011-1017.
19. Jack CR, Garwood M, Wengenack TM, Borowski B, Curran GL, Lin J, Adriany G, Grohn IHJ, Grimm R, Poduslo JF. In vivo visualization of Alzheimer's amyloid plaques by magnetic resonance imaging in transgenic mice without a contrast agent. *Magn Reson Med* 2004;52:1263-1271.
20. Jack CR, Wengenack TM, Reyes DA, Garwood M, Curran GL, Borowski BJ, Lin J, Preboske GM, Holasek SS, Adriany G, Poduslo JF. In vivo magnetic resonance microimaging of individual amyloid plaques in Alzheimer's transgenic mice. *J Neurosci* 2005;25:10041-10048.

21. Vanhoutte G, Dewachter I, Borghgraef P, Van Leuven F, Van der Linden A. Noninvasive in vivo MRI detection of neuritic plaques associated with iron in APP[V717I] transgenic mice, a model for Alzheimer's disease. *Magn Reson Med* 2005;53:607-613.
22. Zhang J, Yarowsky P, Gordon MN, Di Carlo G, Munireddy S, van Zijl PCM, Mori S. Detection of amyloid plaques in mouse models of Alzheimer's disease by magnetic resonance imaging. *Magn Reson Med* 2004;51:452-457.
23. Thomas MA, Hattori N, Umeda M, Sawada T, Naruse S. Evaluation of two-dimensional L-COSY and PRESS using a 3 T MRI scanner: from phantoms to human brain in vivo. *NMR Biomed* 2003;16:245-251.
24. Gruetter R, Weisdorf SA, Rajanayagan V, Terpstra M, Merkle H, Truwit CL, Garwood M, Nyberg SL, Ugurbil K. Resolution improvements in in vivo H-1 NMR spectra with increased magnetic field strength. *J Magn Reson* 1998;135:260-264.
25. Tkac I, Gruetter R. Methodology of H-1 NMR spectroscopy of the human brain at very high magnetic fields. *Applied Magnetic Resonance* 2005;29:139-157.
26. Tkac I. Lecture notes: The Ingredients of a Successful MRS Study at Ultra-High-Field. ISMRM 16th annual meeting 2008. Toronto, Canada.

# Appendix

## L-COSY pulse program

---

This is the L-COSY pulse program implemented on the Bruker BioSpin 9.4 and 17.6T MR spectrometers used for the research presented in this thesis.

```
; lcosy.ppg -
```

```
#include <Avance.incl>
```

```
#include <DBX.include>
```

```
#include <PrepModulesHead.mod>
```

```
define delay de4
```

```
"de4=0.00002-de+depa"
```

```
define delay decodur
```

```
"decodur=0.00002-de+depa"
```

```
#include <decoacq.mod>
```

```
define loopcounter lds={$NDummyScans}
```

```
preset off
```

```
#include <MEDSPEC.include>
```

```
;-----D/P-----GRAD-----RF/ACQ-----
```

```
start, 4u
```

```
av, d1 fq8b:f1
```

```
;-----Triggered data -----
```

```
#include <TriggerPerSlice.mod>
```

```
;-----noe module-----
```

```
#include "noe.mod"
```

```
;-----ws & ovs module-----
```

```
#include "WsOvs.mod"
```

```
;-----localisation module-----
```

```
1u ; reset:f1
```

```
d4 grad{ (t1) | (0.0) | (0.0) } fq1:f1
```

```
d6 gatepulse 1
```

```
(p1:sp1 ph1):f1
```

```
d6
```

```
d7 groff
```

```
goto 10
```

```
nav, 1u
```

```
if ( PVM_ppgFlag4 == Yes) { ; Retro frequency lock
```

```

    d4    grad{ (t1) | (0.0) | (0.0) }    fq1:f1
    d6                                gatepulse 1
    (p1:sp0 ph1):f1
    d6
    d7    groff
  }
10 d8    grad{ (t4) | (t6) | (t7) }
    d4    grad{ (0.0) | (t2) | (0.0) }    fq1:f1
    d6                                gatepulse 1
    (p2:sp2 ph2):f1
    d6
    d8    grad{ (t5) | (t6) | (t7) }
    d9    groff

d0 ; COSY time evolution

;pulse adjustments:
if ( PVM_ppgFlag3 == Yes ) {
d12    grad{ (t11) | (t12) | (t13) }
d4     groff
}
d10    grad{ (t8) | (t9) | (t10) }    fq1:f1
d4     grad{ (0.0) | (0.0) | (t3) }
d6                                gatepulse 1
(p3:sp3 ph3):f1
d6
d10    grad{ (t8) | (t9) | (t10) }
d11    groff

;-----data acquisition-----
;pulse adjustments:
if ( PVM_ppgFlag3 == Yes )
{
d4     grad{ (t14) | (t15) | (t16) }
de4                                REC_ENABLE
                                ADC_INIT_B(ph31, ph30)
                                ADC_START
aqq
}
else
{
subr decoup(decodur,ph31,ph30)
}
3m groff
if(OPT_RFLOnOff == On)
{
1m reload B0
}
else
{
1m
}
1m                                ADC_END

```

```

;-----navigator loop -----
    lo to nav times l1

;-----dummy scans -----
    "lds = lds - 1"
    if "lds>=0" goto start

;-----averaging & phase cycling-----
    if ( ACQ_scan_type == Scan_Experiment ) {
        1u                ipp1
        1u                ipp2
        1u                ipp3
        1u                ipp31
    }
    lo to start times NA
    1u                    rpp1
    1u                    rpp2
    1u                    rpp3
    1u                    rpp31

    if(ACQ_scan_type != Setup_Experiment)
    {
        1u id0
        1u id1
    }
    lo to start times ACQ_size[1]

    1u
    lo to av times NR
        SETUP_GOTO(av)
exit

ph0 = 0
ph1 = 0 0 0 0 0 0 0 0 0 0 0 0 0 0 0 0
ph2 = 0 0 1 1 0 0 1 1 2 2 3 3 2 2 3 3
ph3 = 0 2 0 2 1 3 1 3 0 2 0 2 1 3 1 3
ph30 = 0
ph31= 0 0 2 2 2 2 0 0 0 0 2 2 2 2 0 0

```





# Summary

---

Alzheimer's disease is the most frequently occurring neurodegenerative disorder, with currently no effective treatment or definitive ante-mortem diagnostic test. AD is characterized clinically by progressive memory loss that eventually leads to dementia. The incidence of AD increases exponentially with age and may emerge as a major health problem due to the current rapid aging of societies. The neuropathology of AD is characterized by neuronal and synaptic loss, and by the development of two lesions: the extracellular senile plaque, which is composed mostly of the  $\beta$ -amyloid peptide, and the intraneuronal neurofibrillary tangle, which is composed of hyperphosphorylated forms of tau protein. Current standards for assessing the progression of Alzheimer's disease are clinical and neuropsychological measures, however, the post-mortem observation of amyloid plaques and neurofibrillary tangles is still necessary for a definitive diagnosis.

Since no definitive *in vivo* biomarker of Alzheimer's disease is available, this impedes both clinical diagnosis in humans and drug development in transgenic animal models of AD. Structural magnetic resonance imaging is capable of visualizing anatomical changes in the brain, such as amyloid plaque deposition or changes in volume due to atrophy of affected regions. Alternatively, magnetic resonance spectroscopy provides a non-invasive way to investigate *in vivo* neurochemical abnormalities, and hence a link between the biochemical alterations and the pathophysiology of disease. Either of these techniques, individually or in combination, may have the potential to provide an *in vivo* biomarker of AD.

This thesis contains the results of studies employing several different MR approaches to study age-dependent changes in the brain of a transgenic mouse model of Alzheimer's disease. The context and relevance of this work is summarized in **Chapter 1**. Provided in **Chapter 2** is a brief theoretical background of the different MR techniques used in the studies presented in this thesis.

In **Chapter 3** it was demonstrated that amyloid plaques can be detected in AD mouse brain using  $\mu$ MRI in combination with a  $T_2$  weighted RARE sequence. The age-dependent development of plaque deposition was followed over time by imaging live Tg2576 mice at regular intervals between the age of 12 and 18 months. There was a remarkable degree of correspondence between the  $A\beta$  plaque distribution detected by  $\mu$ MRI and immunohistochemistry. In addition to the visualization of plaques, changes in  $T_2$  relaxation times were followed with age. Following the plaque development in the same animals with

age showed that the plaque-load and plaque size increased markedly, while  $T_2$  relaxation times showed a decreasing trend with age. These results demonstrate that  $\mu$ MRI may be used to follow the plaque developmental characteristics *in vivo* in the same animals and suggest that monitoring the effect of future therapeutic interventions over time in the same animals will be possible by  $\mu$ MRI.

In addition to structural changes, AD causes alterations in the neurochemical profile. MR spectroscopy is an ideal method for obtaining neurochemical information non-invasively from a localized region in the brain. In **Chapter 4**, a 2D MRS method (L-COSY) is implemented and optimized on a 9.4T scanner to study the neurochemical profile in mouse brain with the added resolution afforded by the second spectral dimension. Optimization of the sequence was done using a phantom solution containing several known metabolites in physiological concentrations. Subsequently the L-COSY method was used to study the neurochemical composition of mouse brain. Using this method, highly resolved 2D spectra were obtained, for the first time, from localized regions in the mouse brain *in vivo*. The combination of the optimized 2D sequence and high field strength allowed detection of cross-peaks of up to 16 brain metabolites from localized regions of mouse brain *in vivo*.

In **Chapter 5** the 2D L-COSY sequence was used, in addition to conventional localized one-dimensional MRS, to study the neurochemical profile in the brains of AD transgenic mice and non-transgenic controls between the ages of 8 and 22 months. Results from the one-dimensional study revealed an increase in taurine and decreases in N-acetylaspartate and glutamate. A remarkable observation in the 2D MRS study was that, until approximately 20 months of age, glycerophosphocholine was found to increase in transgenic animals compared to controls. At ages above ~20 months GPC levels dropped to values in the same range as observed in controls, which may reflect gross membrane impairment at later stages of AD or down-regulation of the membrane phospholipid turnover. The observed increase in GPC levels correlates well with the increasing plaque-load in the transgenic mice visualized by  $\mu$ MRI. This confirms that there may be a link between plaque deposition and membrane phospholipid breakdown, as suggested in *ex vivo* and *in vitro* studies by other groups. This study provides the first direct *in vivo* evidence for the increase in GPC in plaque affected areas and suggests that altered GPC may be a valuable marker for early diagnosis and for testing therapeutics in the AD mouse model.

Finally, **Chapter 6** provides a general discussion of this work and future outlook.

# Samenvatting

---

De ziekte van Alzheimer (AD) is de meest voorkomende neurodegeneratieve aandoening. Momenteel bestaat er geen effectieve behandeling of sluitende diagnose voor. AD wordt gekenmerkt door een geleidelijke achteruitgang van het cognitief functioneren, wat uiteindelijk resulteert in dementie. De incidentie van AD neemt exponentieel toe met het ouder worden en gezien de vergrijzing in de samenleving is dit potentieel een groot gezondheidsprobleem. De pathologie van AD wordt gekarakteriseerd door het verlies van neuronen en synapsen en het ontstaan van twee karakteristieke lesies: extracellulaire plaques die voornamelijk uit  $\beta$ -amyloïd ( $A\beta$ ) peptiden bestaan en intraneuronale neurofibrillaire tangles die bestaan uit hypergefosforyleerde vormen van het tau eiwit. Thans wordt het voortschrijden van de ziekte van Alzheimer gevolgd met behulp van klinische en psychologische methoden. Echter, voor een definitieve diagnose blijft het noodzakelijk de hersenen post-mortem te onderzoeken op de aanwezigheid van amyloïd plaques en neurofibrillaire tangles.

Door het ontbreken van een *in vivo* biomarker voor AD wordt tevens medicijnonderzoek in transgene diermodellen van de ziekte bemoeilijkt. Structurele magnetische resonantie imaging (MRI) is in staat de anatomische veranderingen in de hersenen, zoals plaque depositie, of volume veranderingen als gevolg van atrofie van aangetaste gebieden, zichtbaar te maken. Daarnaast maakt magnetische resonantie spectroscopie (MRS) het mogelijk op een niet-invasieve manier *in vivo* neurochemische veranderingen te bestuderen en dus ook een verband te leggen tussen de biochemische veranderingen en de pathofysiologie van de ziekte. Deze technieken, individueel of in combinatie, hebben het potentieel om een *in vivo* biomarker van AD te leveren.

Dit proefschrift bevat de resultaten van verschillende studies waarbij MR technieken zijn toegepast om de leeftijdsafhankelijke veranderingen te bestuderen in de hersenen van een transgeen muismodel van de ziekte van Alzheimer. De context en de relevantie van dit werk wordt samengevat in **Hoofdstuk 1**. In **Hoofdstuk 2** is een korte beschrijving opgenomen van de theoretische achtergronden van de verschillende MR-technieken die gebruikt werden in de studies beschreven in dit proefschrift.

In **Hoofdstuk 3** werd aangetoond dat amyloïde plaques kunnen worden gedetecteerd in AD muizenhersenen met behulp van MR micro-imaging ( $\mu$ MRI) in combinatie met een  $T_2$  gewogen RARE sequentie. De leeftijdsafhankelijke ontwikkeling van plaque afzetting werd

gevolgd in de tijd in levende Tg2576 muizen door ze met regelmatige tussenpozen te scannen tussen de leeftijd van 12 en 18 maanden. Hierbij werd een opmerkelijke overeenkomst gevonden tussen de A $\beta$  plaque distributie gedetecteerd door  $\mu$ MRI en door immunohistochemie. Naast de visualisatie van plaques, werden veranderingen in  $T_2$  relaxatietijden gevolgd bij het vorderen van de leeftijd. Het volgen van de ontwikkeling van plaques in dezelfde dieren toonde aan dat de hoeveelheid en omvang van de plaques toenamen, terwijl de  $T_2$  relaxatietijd een dalende trend vertoonde met toenemende leeftijd. Deze resultaten laten zien dat  $\mu$ MRI kan worden gebruikt om de plaque ontwikkelingskenmerken *in vivo* in dezelfde dieren te volgen en wijzen erop dat het bestuderen van het effect van toekomstige therapeutische interventies over de tijd in dezelfde dieren mogelijk zal zijn met behulp van  $\mu$ MRI.

Naast de structurele veranderingen veroorzaakt AD veranderingen in het neurochemische profiel in de hersenen. MR-spectroscopie is een ideale methode voor het verkrijgen van neurochemische informatie, op een niet-invasieve manier, uit een gelokaliseerde regio in de hersenen. In **Hoofdstuk 4** volgt de beschrijving van een 2D MRS methode: gelokaliseerde correlatie spectroscopie, ofwel L-COSY. Deze methode werd geïmplementeerd en geoptimaliseerd voor een 9.4T-scanner. Door de toegevoegde spectrale dimensie werd mogelijk om met verhoogde resolutie het neurochemische profiel in muizenhersen te bestuderen. Optimalisatie van de L-COSY methode werd gedaan met behulp van een fantoom oplossing met verschillende bekende metabolieten in fysiologische concentraties. Vervolgens werd de L-COSY methode gebruikt voor het bestuderen van het neurochemische metabole patroon in muizenhersen. Met behulp van deze methode zijn, voor het eerst, duidelijke *in vivo* 2D spectra verkregen uit gelokaliseerde regio's in de muizenhersen. De combinatie van de geoptimaliseerde 2D sequentie en de hoge veldsterkte maakte het mogelijk *in vivo* de "kruis-pieken" te detecteren van tot 16 metabolieten in gelokaliseerde gebieden in de muizenhersen.

In **Hoofdstuk 5** wordt de 2D L-COSY methode gebruikt, naast conventionele gelokaliseerde een-dimensionale MRS, om het neurochemische profiel in de hersenen van AD transgene muizen en niet-transgene controles in de leeftijd tussen 8 en 22 maanden te bestuderen. Resultaten van de een-dimensionale studie toonden een toename van taurine en dalingen van N-acetylaspartaat en glutamaat. Een opmerkelijke observatie in de 2D-MRS studie was dat, tot een leeftijd van ongeveer 20 maanden, glycerophosphocholine (GPC) bleek toe te nemen in transgene dieren in vergelijking met de controlegroep. Voor leeftijden boven de 20 maanden daalden GPC niveaus tot waarden in dezelfde orde van grootte als waargenomen in de controlegroep, wat een afspiegeling kan zijn van een grootschalige membraanbeschadiging in de latere stadia van Alzheimer of een regulatie van de omzetting van

membraanfosfolipide. De waargenomen stijging van de GPC niveaus correleert goed met de toenemende plaquevorming in de transgene muizen, zoals gevisualiseerd met  $\mu$ MRI. Dit bevestigt dat er mogelijk een verband bestaat tussen de plaque depositie en membraan fosfolipide afbraak, zoals gesuggereerd in *ex vivo* en *in vitro* studies van andere groepen. Deze studie vormt het eerste directe *in vivo* bewijs voor de stijging van GPC in de door plaque getroffen gebieden, wat aangeeft dat een verandering in GPC concentratie wellicht een belangrijke marker voor vroegtijdige diagnose en voor het testen van therapeutica in het AD muismodel kan zijn.

Tot slot wordt in **Hoofdstuk 6** een algemene bespreking van dit werk gegeven en wordt het toekomstperspectief van het werk geschetst.



# Curriculum Vitae

---

In 1994, after finishing my high school education, I started my studies in the department of mechanical engineering at the University of the Netherlands Antilles (UNA) in Curaçao. In 1996 I transferred to the Eindhoven Technical University in the Netherlands, to study medical engineering (werktuigkundige medische technologie, WMT), at the time a separate discipline within the mechanical engineering department. In 2002 I did two internships at the faculty of biomedical engineering: “*Experimental and numerical evaluation of a minimally invasive extra-corporeal circulation*” under guidance of prof. dr. ir. F.N. v.d. Vosse, dr. ir. M.C.M. Rutten, prof. dr. N.H.J. Pijls and P.A.M. Everts and “*Experimental determination of the three-dimensional collagen architecture of the articular cartilage of the knee joint*” under guidance of dr. C.C. v. Donkelaar and ir. W. Wilson. After obtaining my bachelor’s degree I proceeded with my master’s in mechanical engineering, but also did many elective courses and final master’s project at the faculty of biomedical engineering. In 2003 I started my master’s dissertation titled “*Determination of the passive transverse mechanical properties of skeletal muscle under in vivo compression*” under supervision of dr. ir. C.W.J. Oomens, ir. A. Stekelenburg and prof. dr. ir. F.P.T. Baaijens. I received my master’s degree in January 2004.

In September 2004 I started my PhD in the solid-state NMR group of prof. dr. H.J.M. de Groot, under the guidance of dr. Alia. During my PhD I had the opportunity to present my work in the form of posters at *Euromar/EENC* (2005) in Veldhoven, Netherlands, at the *Annual Meeting of the Study Group Neurochemistry of the German Society of Biochemistry and Molecular Biology* (2005) in Leipzig, Germany, at the *14<sup>th</sup> scientific meeting of the International Society for Magnetic Resonance in Medicine* (2006) in Seattle, USA where I was Nominated for a poster award in the category 'Neuroimaging' and was awarded 3rd place. Additionally I have presented posters at the *Genomics Research Event* (2007) in Amsterdam, Netherlands, and at the *First Benelux in vivo MR methods Symposium* (2007) in Nijmegen, Netherlands. I was invited to present my work in the form of an oral presentation at the *2<sup>nd</sup> Annual CMSB Members Symposium* (2005), in Amsterdam, Netherlands, at the *First Benelux in vivo MR methods Symposium* (2007), in Nijmegen, Netherlands, and was also given the opportunity to present my work orally at the *16<sup>th</sup> scientific meeting of the International Society for Magnetic Resonance in Medicine* (2008), in Toronto, Canada.

In December 2008 I will start my medical physicist traineeship at the Catharina hospital in Eindhoven, under guidance of ir. P.J.M. Brands.





# List of publications

---

## *Full publications*

### **Longitudinal assessment of Alzheimer's $\beta$ -amyloid plaque development in transgenic mice monitored by *in vivo* magnetic resonance microimaging**

**N. Braakman**, J. Matysik, S.G. van Duinen, F. Verbeek, R. Schliebs, H.J.M.de Groot, A. Alia  
Journal of Magnetic Resonance Imaging (2006); 24:530-536

### **High resolution localized two dimensional magnetic resonance spectroscopy in mouse brain *in vivo***

**N. Braakman**, T. Oerther, H.J.M.de Groot, A. Alia  
Magnetic Resonance in Medicine (2008); 60:449-456

### **Prospects for early detection of Alzheimer's disease from serial MR images in transgenic mouse models**

M. Muskulus\*, A.E.H. Scheenstra\*, **N. Braakman**, J. Dijkstra, S. Verduyn-Lunell, A. Alia, H.J.M. de Groot, J. H. C. Reiber

\*authors contributed equally

Revised manuscript submitted to Current Alzheimer Research (2008)

### **Recent advances in visualizing Alzheimer's plaques by magnetic resonance imaging**

**N. Braakman**, M.A. van Buchem, R. Schliebs, H.J.M. de Groot, A. Alia  
Revised manuscript submitted to Current Medical Imaging Review (2008)

### **Correlation between the severity of amyloid- $\beta$ deposition and altered neurochemical profile in a transgenic mouse model of Alzheimer's disease, observed by $\mu$ MRI and high resolution two-dimensional MRS**

**N. Braakman**, R. Schliebs, H.J.M.de Groot, A. Alia  
Manuscript in Preparation

***Conference proceedings***

**Visualization of Alzheimer's  $\beta$ -amyloid plaques *in vivo* by magnetic resonance imaging.**

**N. Braakman**, J. Matysik, H.J.M.de Groot, R. Schliebs, A. Alia

Presented at the Annual Meeting of the Study Group Neurochemistry of the German Society of Biochemistry and Molecular Biology

International Journal of Developmental Neuroscience 24 (2006); 226

**Longitudinal study of the development of beta-amyloid plaque burden in a transgenic mouse model of Alzheimer's disease, using *in vivo* magnetic resonance imaging**

**N. Braakman**, J. Matysik, S.G. van Duinen, F. Verbeek, R. Schliebs, H.J.M.de Groot, A. Alia

Proceedings ISMRM 14 (2006); 933

***In vivo* high resolution localized two dimensional magnetic resonance spectroscopy in mouse brain**

**N. Braakman**, T. Oerther, H.J.M.de Groot, A. Alia

Proceedings ISMRM 16 (2008); 121

**Correlation between neurochemical changes and development of Alzheimer's disease**

**N. Braakman**, J. Matysik, H. J. De Groot, R. Schliebs, A. Alia

Proceedings ISMRM 16 (2008); 257

# Nawoord

---

Na iets meer dan vier jaar komt, met het verschijnen van dit proefschrift, een einde aan mijn “tweede studententijd” en mijn verblijf in Leiden. Ondanks de nodige stress de laatste maanden is zeer zeker de uitdrukking “time flies when you’re having fun” van toepassing op mijn tijd binnen de SSNMR groep. Als afsluiting van mijn promotieonderzoek wil ik graag diegenen noemen die in meer of mindere mate, al dan niet wetenschappelijk, een bijdrage hebben geleverd aan het tot stand komen van dit proefschrift.

Leuke herinneringen heb ik aan de eerste paar maanden in LCP28, met Samira, Swapna en Geerten als kamergenoten, en later boven in de ‘denktank’ met eerst Ania en later Geertje als kamergenote. Het kweken van nieuwe levensvormen door Geerten was een avontuur op zich. Het begin met Samira als de twee imaging promovendi in een groep die verder overwegend georiënteerd is op NMR spectroscopie was niet altijd even makkelijk maar daardoor niet minder interessant. Uiteindelijk hebben we onze plek toch gevonden. Fons en Kees moet ik ook zeker noemen, voor het mij wegwijs maken in de basis MRI/MRS en de bijbehorende systemen, en het zorgen voor een plezierige werkomgeving op de NMR afdeling. Bianca Hogers heeft een aanzienlijke bijdrage geleverd aan mijn basis MRI kennis. My appreciation goes to Thomas Oerther of Bruker BioSpin in Karlsruhe, for the useful e-mail correspondence regarding the implementation of the MR spectroscopy methods described in this thesis. I am happy that Firat will continue what I started.

De atmosfeer in de SSNMR/BOF groep was erg plezierig, dankzij mijn collega’s: Anjali, Arjan Siebum, Arjan van Wijk, Francesco, Ido, Ineke, Jörg, José-Luis, Rob de Jong, Shipra and Smitha. Memorable are the numerous discussions I had with Piotr about life, the universe and everything, and the late night discussions and noodle sessions with Karthick while running overnight experiments. In retrospect I have fond memories of running the 10 km in the Leiden marathon with Swapna, Anna, Karthick and Johan, and also of the Friday night sports, the game nights, and the culinary discussions and experiences together with them, Esha and Prashant. Eugenio should be mentioned for the interesting discussions and for his ability to cook a great risotto. The multicultural and always tasty evenings with Thierry will not be forgotten.

De plezierige discussies tijdens de lunch, en de activiteiten buiten werk om met Rob van der Steen en Reinier zullen me zeker bijblijven. Liesbeth zorgde voor een gezellige sfeer op het secretariaat en was wel te porren voor een geintje. Wim van Oordt heeft me veel werk uit handen genomen met de muizen, en heeft me de nodige moed ingesproken tijdens de sollicitatie naar mijn volgende functie.

Van het LUMC wil ik nog noemen Rob van de Ven en Rob Nabuurs, voor hun aanstekelijke enthousiasme; Brigit en Mascha voor wat welkome afwisseling in de dagelijkse Alzheimer imaging routine; Louise voor de suggesties als het eens niet lekker liep. Verder Jouke, Faiza, Roald en Hans, voor hun bereidheid de verschillende beeldverwerking- en analyse methodes toe te passen op mijn data. Ook Alize en Michael mogen hier niet ontbreken; Onze verschillende achtergronden vormden een mooie aanvulling op elkaar, de samenwerking was altijd plezierig, en het resultaat mag er wezen.

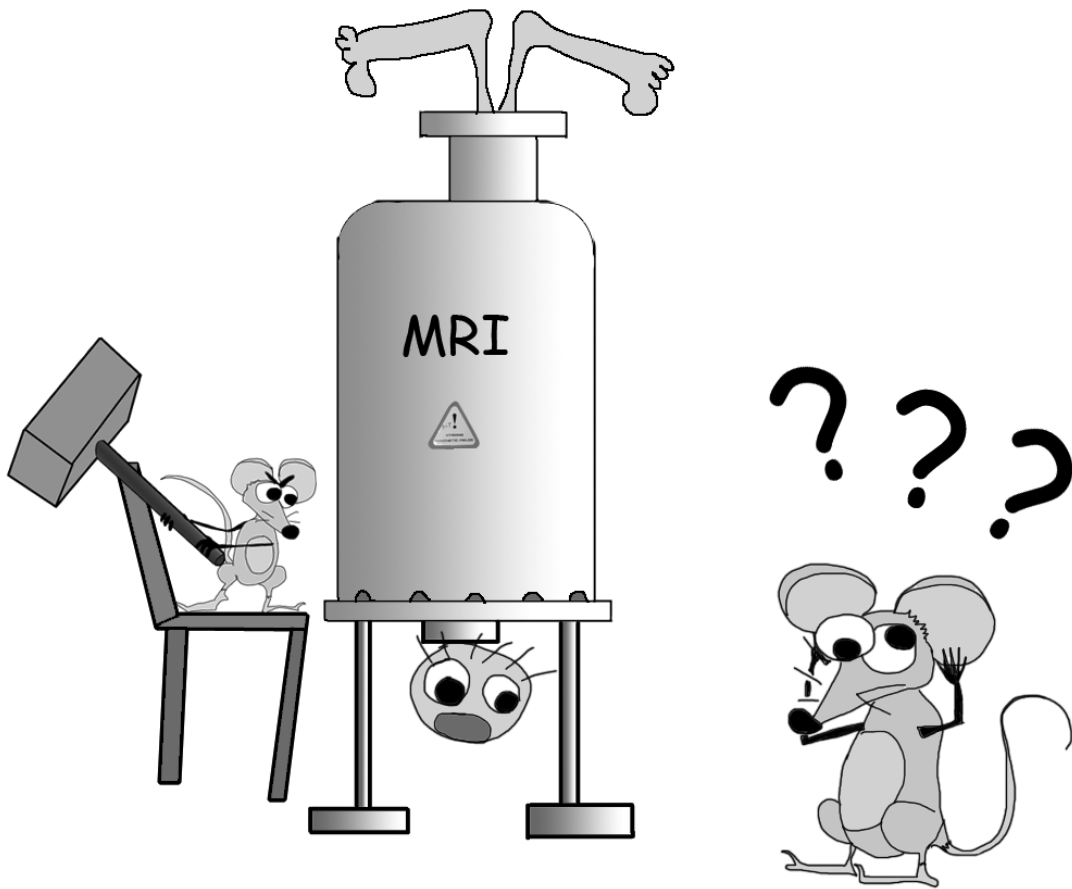
Van de Bedrijfshulpverlening (BHV) wil ik nog noemen Cees en Peter; zij hebben ervoor gezorgd dat ik naast wetenschappelijke kennis ook de nodige praktische kennis heb opgedaan.

Uiteindelijk wil ik nog noemen Rogier en Martijn, voor steun en de soms hoognodige afleiding, zowel op het lab als daarbuiten. Mijn ouders, die mij hebben gesteund tijdens mijn, wellicht iets te lange, “eerste studententijd”. Door hen was het mogelijk om aan deze promotie te beginnen, deels ook doordat mijn moeder per toeval de vacature voor mijn project ontdekte. En als laatste, *maar zeker niet als minste*, wil ik Charlotte noemen; ze stond altijd voor me klaar, ook in tijden dat ik wat minder gezellig was. Zonder haar warmte, steun en aanmoediging had ik deze promotie onmogelijk op tijd af kunnen hebben.

Leiden, oktober 2008

Niels Braakman

# Of (AD) Mice and Me(n)



© 2005, Niels Braakman







